Stony Brook University

Measurement of the Single Charged Pion Production Cross Section in Charged-Current Neutrino-Carbon Interactions

A Dissertation Presented

by

Lisa Angelika Whitehead

to

The Graduate School

in Partial Fulfillment of the

Requirements

for the Degree of

Doctor of Philosophy

in

Physics

Stony Brook University

May 2007

Stony Brook University

The Graduate School

Lisa Angelika Whitehead

We, the dissertation committee for the above candidate for the
Doctor of Philosophy degree, hereby recommend
acceptance of this dissertation.

Dr. Chang Kee Jung - Dissertation Advisor
Professor of Physics, Department of Physics and Astronomy

Dr. George Sterman - Chairperson of Defense
Distinguished Professor of Physics, Department of Physics and Astronomy

Dr. Thomas Hemmick
Professor of Physics, Department of Physics and Astronomy

Dr. Lucio Ludovici
Physicist
INFN Research Scientist, University of Rome "La Sapienza"

This dissertation is accepted by the Graduate School.

Lawrence Martin
Dean of the Graduate School

Abstract of the Dissertation

Measurement of the Single Charged Pion Production Cross Section in Charged-Current Neutrino-Carbon Interactions

by

Lisa Angelika Whitehead

Doctor of Philosophy

in

Physics

Stony Brook University

2007

The discovery of neutrino oscillations is one of the most exciting recent developments in particle physics. Current and future neutrino experiments are aiming to make precise measurements of the oscillation parameters. Improving our understanding of neutrino-nucleus cross sections is crucial to these precision studies of neutrino oscillations. Interactions in the neutrino energy region around 1 GeV are particularly important because this is the region of the expected oscillation signal in many experiments, but the cross sections in this region are not very well-known. This energy region is complicated due to overlapping contributions from quasi-elastic scattering, resonant single pion production, and deep inelastic scattering. This dissertation describes a measurement of the cross section for resonant single charged pion production in charged-current muon neutrino interactions with a carbon target. The measurement was made using data collected by the K2K long-baseline neutrino oscillation experiment, which used a muon neutrino beam with a mean energy of 1.3 GeV. The results of this measurement are consistent with previous experiments and predictions based on a widely-accepted model.

Contents

List of Tables

List of Figures

Acknowledgments

I would like to thank my advisor, Dr. Chang Kee Jung, for the opportunity to be part of this group. I am grateful for his encouragement, criticism, and honest advice (not to mention excellent barbecue and poker games). I thank Dr. Kenkou Kobayashi for helping me with every project that I have taken on. He has also occasionally been my translator and tour guide, for which I am very grateful. I also want to thank Dr. Clark McGrew, Dr. Chiaki Yanagisawa, and Dr. Peter Paul for their help and guidance. To all of my fellow NN group students - Fumi Kato, Ryan Terri, Glenn Lopez, Le Phuoc Trung, and Dima Beznosko - thank you for your friendship (and a few good parties), and I hope our paths cross again in the future. I also want to thank Joan Napolitano and Alice Dugan for all they do to keep the High Energy Group running smoothly.

I would like to thank the K2K Collaboration and especially everyone in the K2K-SciBar group. I want to thank Dr. Tsuyoshi Nakaya, Dr. Masashi Yokoyama, Dr. Lucio Ludovici, Dr. Federico Sanchez, and Dr. Michel Sorel for their excellent leadership of the SciBar group. I would especially like to thank Michel and Federico for guiding the final phase of this analysis. I thank Yokoyama-san and Nakaya-san for hosting me at Kyoto University during the times I stayed there. I am extremely grateful for the help of Dr. Masaya Hasegawa when I was getting started on this analysis. He answered my questions with endless patience. I appreciate the work of Gabriel Jover-Mañas in preparing the final versions of the SciBar data and MC sets that were used in this analysis. Last, and certainly not least, I would like to thank Ana Yaiza Rodriguez Marrero for her many contributions to this analysis! Working with Ana has really been a pleasure, and my work has been easier to do because of our collaboration.

Thanks to my parents for their love and support. I couldn't have achieved anything without the good start they gave me.

Finally, I thank Alan Dion for making life more fun. (Also for teaching me to use Linux without spilling piping hot gravy all over myself.)

Chapter 1

Introduction

The neutrino is one of the elementary particles which make up the universe. Neutrinos are produced in the fusion reactions inside the sun and other stars, by natural background radiation inside the earth, by supernovae, and by charged particles bombarding Earth's atmosphere. Despite their abundance, neutrinos remain mysterious because they are difficult to observe.

1.1 Neutrinos in the Standard Model

The existence of the neutrino was first proposed by Pauli in 1930 to explain the continuous electron energy spectrum observed in nuclear β-decay [1]. At the time, β-decay was understood to be the decay of a nucleus A into a lighter nucleus B with the emission of an electron, A $\rightarrow$ B e^-. In such a two-body decay, if A decays at rest, then according to the conservation of energy, the energy of the outgoing electron should be

$$E_e = \frac{m_A^2 - m_B^2 + m_e^2}{2m_A} \tag{1.1}$$

(where m is mass), yielding a monochromatic energy spectrum. Instead, β-decay experiments observed a continuous electron energy spectrum, with E_e as the maximum possible electron energy, $E_{max} \approx E_e$. Pauli proposed that another particle that he called the "neutron" (now known as the neutrino, ν) was being emitted in the decay, A $\rightarrow$ B e^- ν. Pauli said the particle should be electrically neutral (to conserve charge) and have spin 1/2 (to conserve angular momentum). He also proposed that the new particle should have a mass on the order of the electron mass. (The experimental observations that

indicated $E_{max} \approx E_e$ put an upper limit on the mass of the new particle.) In 1934, Fermi published a theory of β-decay [2] that incorporated this particle. By that time, the particle now known as the neutron had been discovered, so Fermi named Pauli's particle the neutrino.

In 1956, Reines and Cowan succeeded in detecting anti-neutrinos from inverse β-decay, $\overline{\nu}p \rightarrow e^+n$ [3] using a nuclear reactor, proving the existence of neutrinos for the first time. In 1962, another type of neutrino was detected in an experiment at Brookhaven National Laboratory [4]. This experiment established that there is one type of neutrino associated with the electron and a second type of neutrino associated with the muon. The Reines/Cowan neutrino was an electron neutrino (ν_e), and the new neutrino was a muon neutrino (ν_μ). Electrons and muons and their associated neutrinos are called leptons. In 1975, a third type of charged lepton, the tau (τ), was discovered. It was assumed then that a third type of neutrino, ν_τ, must exist. The tau neutrino was finally directly observed in 2001 [5] by the DONUT collaboration at Fermilab.

Neutrinos are electrically neutral and so they cannot interact electromagnetically. Color is the "charge" associated with the strong interaction; neutrinos are color-neutral and so do not interact strongly. Thus, neutrinos can only interact via the weak interaction. There are two types of weak interactions: charged-current (CC) and neutral-current (NC). CC interactions are mediated by charged W bosons and couple neutrinos to their charged lepton partners. NC interactions are mediated by the neutral Z boson and couple neutrinos to themselves. In the Standard Model of particle physics, neutrinos are massless. Experiments that can measure the mass of neutrinos directly (such as β-decay experiments) have so far only been able to set upper limits. The current upper limit obtained by tritium decay experiments is $m_\nu = 2$ eV/c^2 [6]. A limit on neutrino mass can also be obtained from cosmological data and assumptions. The cosmological limit, $\sum m_i$ <1 eV/c^2, is the most stringent limit on neutrino masses so far [6].

1.2 Neutrino Oscillations

According to experimental studies of Z decays, there are three types of light neutrinos [6]. The three "flavors" of neutrinos are electron, muon, and tau. Based on quantum mechanical principles, if neutrinos have a nonzero mass and the mass eigenstates do not correspond to the flavor eigenstates, then neutrinos can mix. This is analogous to the mixing in the quark sector.

The flavor states, $|\nu_\alpha\rangle$, are superpositions of the mass states, $|\nu_i\rangle$.

$$|\nu_\alpha\rangle = \sum_i U^*_{\alpha i} |\nu_i\rangle \tag{1.2}$$

where $\alpha = e, \mu, \tau$, $i = 1, 2, 3$, and U is a unitary mixing matrix.

Assume that a neutrino ν_α is produced by a weak interaction in a flavor eigenstate. To understand how the state evolves in time, we apply the time-dependent Schrödinger Equation to each ν_i component of ν_α in the rest frame of that component. This gives us

$$|\nu_i(\tau_i)\rangle = e^{-im_i\tau_i}|\nu_i(0)\rangle \tag{1.3}$$

where m_i is the mass of ν_i and τ_i is the time in the ν_i rest frame. In this section, natural units ($\hbar = c = 1$) are used. The phase factor is Lorentz-invariant and thus may be written in terms of laboratory frame time t and position L,

$$|\nu_i(t)\rangle = e^{-i(E_it - p_iL)}|\nu_i\rangle \tag{1.4}$$

where E_i and p_i are the energy and momentum of ν_i in the laboratory frame. The neutrino is highly relativistic, and thus we can make the approximation, $t \approx L$, giving

$$|\nu_i(L)\rangle = e^{-i(E_i - p_i)L}|\nu_i\rangle \tag{1.5}$$

Assume ν_α is produced with definite momentum p, so that all of the mass eigenstate components of ν_α have a common momentum, $p_i = p$. Also, we can assume that the neutrino masses m_i are sufficiently small compared with the momentum so that we can make the approximation $E_i = \sqrt{p^2 + m_i^2} \approx p + \frac{m_i^2}{2p}$. Then the equation for $|\nu_i(L)\rangle$ becomes

$$\begin{aligned} |\nu_i(L)\rangle &= e^{-i(p + m_i^2/2p - p)L}|\nu_i\rangle \\ |\nu_i(L)\rangle &= e^{-im_i^2L/2p}|\nu_i\rangle \end{aligned} \tag{1.6}$$

Finally, let $E \simeq p$ be the average energy of all the mass eigenstate components of the neutrino.

$$|\nu_i(L)\rangle = e^{-im_i^2L/2E}|\nu_i\rangle \tag{1.7}$$

Thus for a neutrino born as a ν_α that has propagated a distance of L, the state vector is:

$$\begin{aligned} |\nu_\alpha(L)\rangle &= \sum_i U_{\alpha i}^*|\nu_i(L)\rangle \\ |\nu_\alpha(L)\rangle &= \sum_i U_{\alpha i}^* e^{-im_i^2L/2E}|\nu_i\rangle \end{aligned} \tag{1.8}$$

The neutrino is produced in a pure flavor eigenstate α, which is a

particular superposition of the mass eigenstates. After travelling a distance L, the neutrino state evolves into a different superposition of the mass eigenstates. If we observe this neutrino at its new position via a weak interaction, what flavor eigenstate will we observe?

The probability of observing a neutrino that was in flavor state α at time $t = 0$ in flavor eigenstate β at time $t = L$ is

$$\begin{aligned} P(\nu_\alpha \to \nu_\beta) &= |\langle \nu_\beta | \nu_\alpha(L) \rangle|^2 \\ &= |\sum_i U^*_{\alpha i} e^{-i m_i^2 L/2E} U_{\beta i}|^2 \end{aligned} \tag{1.9}$$

In the two-flavor approximation, where we assume there are only two flavor states and two mass states, the mixing matrix U can be written

$$U = \begin{pmatrix} \cos\theta & \sin\theta \\ -\sin\theta & \cos\theta \end{pmatrix} \tag{1.10}$$

where the mixing angle θ is the only parameter needed to describe the mixing. In this case, the probability of flavor change becomes

$$\begin{aligned} P(\nu_\alpha \to \nu_\beta) &= \sin^2 2\theta \sin^2 \frac{\Delta m^2 L}{4E} \\ &= \sin^2 2\theta \sin^2 \frac{1.27 \Delta m^2 L}{E} \end{aligned} \tag{1.11}$$

where $\Delta m^2 = m_2^2 - m_1^2$ is measured in $(\mathrm{eV}/c^2)^2$, L is measured in km, and E is measured in GeV. The factor of 1.27 comes from including the relevant factors of $\hbar$ and c.

For the case of three neutrinos, a common way to write the mixing matrix is

$$U = \begin{pmatrix} c_{12}c_{13} & s_{12}c_{13} & s_{13}e^{-i\delta} \\ -s_{12}c_{23} - c_{12}s_{23}s_{13}e^{i\delta} & c_{12}c_{23} - s_{12}s_{23}s_{13}e^{i\delta} & s_{23}c_{13} \\ s_{12}s_{23} - c_{12}c_{23}s_{13}e^{i\delta} & -c_{12}s_{23} - s_{12}c_{23}s_{13}e^{i\delta} & c_{23}c_{13} \end{pmatrix} \tag{1.12}$$

where $c_{ij} = \cos\theta_{ij}$ and $s_{ij} = \sin\theta_{ij}$. In this case, there are four parameters to describe the mixing: three mixing angles θ_{12}, θ_{13}, and θ_{23} and a CP-violating phase δ.

The Super-Kamiokande collaboration announced in 1998 the first compelling evidence for oscillations of neutrinos produced in the upper atmosphere [7]. The observation of neutrino oscillations has proven indirectly that neutrinos have non-zero mass by showing that Δm^2 is non-zero. The most recent result from Super-Kamiokande for the $\nu_\mu \to \nu_\tau$ oscillation parameters is $\sin^2 2\theta_{23} > 0.92$ and $1.5 \times 10^{-3} < \Delta m^2_{23} < 3.4 \times 10^{-3}$ $(\mathrm{eV}/c^2)^2$ at the 90%

confidence level [8].

1.3 K2K, A Long-Baseline Neutrino Oscillation Experiment

The purpose of the KEK to Kamioka (K2K) Long-Baseline Neutrino Oscillation Experiment is to confirm the observation of atmospheric neutrino oscillations using accelerator-produced neutrinos. K2K is the first successful experiment of this type. Muon neutrinos are produced by an accelerator at KEK in Tsukuba, Japan and detected by a suite of near detectors; the neutrino beam is then detected 250 km away in Kamioka, Japan at the Super-Kamiokande (SK) 50 kiloton water Cherenkov detector (see Figure 1.1).

Figure 1.1: Map of Japan's main island showing the location of KEK and SK.

What is the signature of neutrino oscillations in such an experiment? For given values of the oscillation parameters and the neutrino masses, the oscillation probability is a sinusoidal function of L/E. For K2K, the distance between the neutrino source (KEK) and the point of observation (SK), denoted L, is fixed. Thus the probability is only energy-dependent; this means that neutrino oscillations change the number of muon neutrino events at SK as a function of energy. To observe this, the muon neutrino flux and energy spectrum need to be measured simultaneously at KEK and SK. The near detector is close enough to the neutrino source that the neutrinos have not oscillated yet; in other words, $L_{near} \approx 0$, which means that the probability of neutrinos changing flavor before reaching the near detector is negligible. The observed flux and energy spectrum at the near detector is extrapolated to SK. A deficit of muon neutrino events and a distortion of the energy spectrum at SK compared to the extrapolation from the near detector measurement indicates the oscillation of

muon neutrinos. To illustrate this effect, Figure 1.2 shows the predicted neutrino energy spectrum distortion at SK. The energy spectrum with and without oscillations (hatched and blank histograms, respectively) is shown as well as the ratio of the spectrum with oscillations to the spectrum without oscillations. Oscillation parameters of $(\sin^2 2\theta_{23}, \Delta m^2_{23}) = (1.0, 3 \times 10^{-3}(\mathrm{eV}/c^2)^2)$ are assumed (these values are consistent with the SK atmospheric neutrino results).

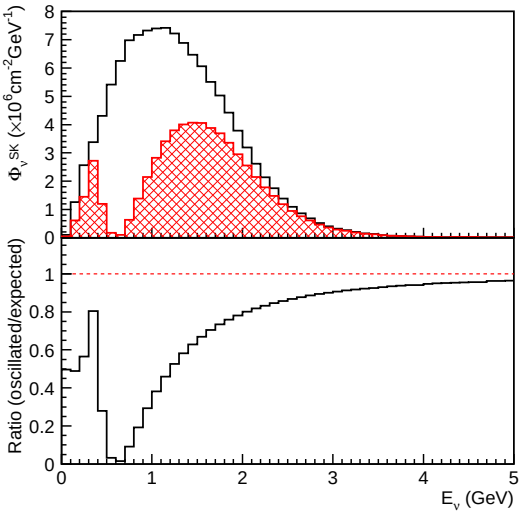

Figure 1.2: Expected neutrino energy spectrum distortion at Super-Kamiokande due to neutrino oscillations.

1.4 Motivation for Neutrino Cross Section Studies

The discovery of neutrino oscillations has renewed interest in studying neutrino interactions because uncertainties in cross sections affect the oscillation measurement. For example, in K2K, the muon neutrino energy spectrum at SK is measured using events in which a single muon is detected. The neutrino energy (E_ν) for single muon events is reconstructed from the muon angle (θ_μ) and momentum (p_μ), assuming each event is a charged-current quasi-elastic (CCQE) interaction, $\nu_\mu n \to \mu^- p$. (CCQE interactions in SK are usually single muon events because the proton is typically below the Cherenkov threshold.) The reconstructed neutrino energy is

$$E_\nu = \frac{E_\mu m_n - \frac{1}{2} m_\mu^2}{m_n - E_\mu + p_\mu \cos\theta_\mu} \tag{1.13}$$

where m_n, m_μ, and $E_\mu = \sqrt{p_\mu^2 + m_\mu^2}$ are the neutron mass, muon mass, and muon energy, respectively. However, not all these single muon events are CCQE events. Figure 1.3 shows the relationship between reconstructed neutrino energy and the true neutrino energy for CCQE and other (non-QE) CC events in SK. The neutrino energy is reconstructed well for true CCQE events. For CC non-QE events, the reconstructed neutrino energy is less than the true energy due to the additional particles that are produced but not detected. To predict the energy spectrum of muon neutrinos at SK, we must be able to predict the number of CC non-QE events in the single muon sample. This illustrates the reason why measurements of neutrino cross sections are important for neutrino oscillation experiments.

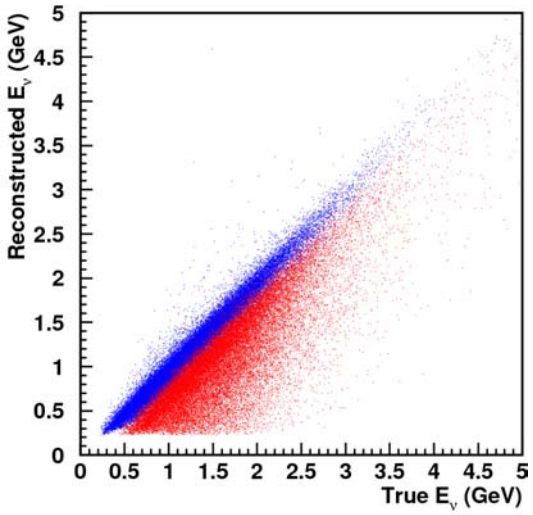

Figure 1.3: Reconstructed neutrino energy vs. true neutrino energy for CCQE (blue) events and CC non-QE (red) events in SK.

Current and future neutrino experiments are planning to make high-statistics precision measurements of the oscillation parameters. This means systematic uncertainties due to neutrino cross sections will be significant. Better knowledge of neutrino-nucleus interactions is crucial to these future precision measurements. Neutrino interactions in the region of neutrino energy around 1 GeV are particularly important because this is the region of the expected oscillation signal in many experiments.

This is the major motivation for the work described in this dissertation, the measurement of the cross section for single charged pion production in charged-current neutrino-carbon interactions, $\nu_\mu N \to \mu^- N \pi^+$. The measurement is made using the SciBar detector, one of the near detectors in the K2K experiment, in which the mean neutrino energy is 1.3 GeV. In Chapter 2, I

will briefly describe the K2K experiment, and in Chapter 3, I will describe the SciBar detector in detail.

Chapter 2

K2K Long-Baseline Neutrino Oscillation Experiment

As mentioned in the introduction, the purpose of the K2K experiment is to confirm the observation of atmospheric neutrino oscillation using accelerator-produced neutrinos. Muon neutrinos are produced by an accelerator at KEK and detected by a suite of near detectors; the neutrino beam is then detected 250 km away at the Super-Kamiokande (SK) detector. K2K's mean energy of 1.3 GeV and baseline distance of 250 km make the experiment sensitive to Δm^2 in the region of what was measured with atmospheric neutrinos.

The period of K2K data acquisition from June 1999 through July 2001 is called K2K-I. The period from January 2003 until the end of the experiment in November 2004 is called K2K-II.

2.1 The Neutrino Beam

To produce a beam of muon neutrinos, a proton beam hits a stationary target, producing mostly pions. The positively charged pions are focused by so-called neutrino horns in the forward direction and decay into muons and muon neutrinos. The charged particles are stopped by a beam dump, leaving the muon neutrinos to propagate in the direction of SK. According to simulation, the neutrino beam at the near detector complex is 97.3% pure ν_μ.

2.1.1 Primary Proton Beam

Figure 2.1 is a diagram of the neutrino beam line at KEK. Protons are accelerated by the KEK Proton Synchrotron (KEK-PS) to an energy of 12

GeV. The protons are extracted to the neutrino beam line in a single turn every 2.2 s. Each extraction, or "spill", lasts for 1.1 μs and consists of 9 bunches of protons with 125 ns spacing between the bunches. The proton beam is initially extracted torward the north, and then it is bent 90 degrees towards the direction of SK. Just before the target, a steering magnet bends the beam approximately 1 degree downward from horizontal.

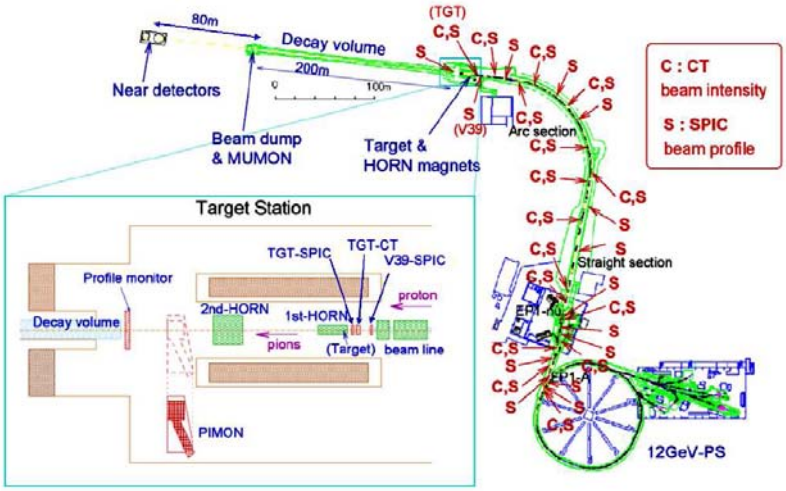

Figure 2.1: KEK-PS and neutrino beam line.

The beam intensity and transportation efficiency are monitored by 13 current transformers placed along the beam line. The current transformers measure the induced current produced by the proton beam passing through a coil. A current transformer placed just before the target is used to estimate the total number of protons delivered to the target. The beam intensity just before the target is typically 5×10^{12} protons per spill. Figure 2.2 shows number of protons on target (POT) as a function of time for the duration of the experiment. In total, 1.049×10^{20} POT are delivered from March 1999 through November 2004.

The profile and position of the proton beam are measured by 28 segmented plate ionization chambers. The chambers consist of three copper sheets that are each 28 μm thick. The gaps between the sheets are 1 cm wide and filled with helium gas. The central sheet is the anode and is supplied with a high voltage of about -1000 V. The outer two sheets consist of vertical or horizontal cathode strips. Data from most of the chambers is used to steer

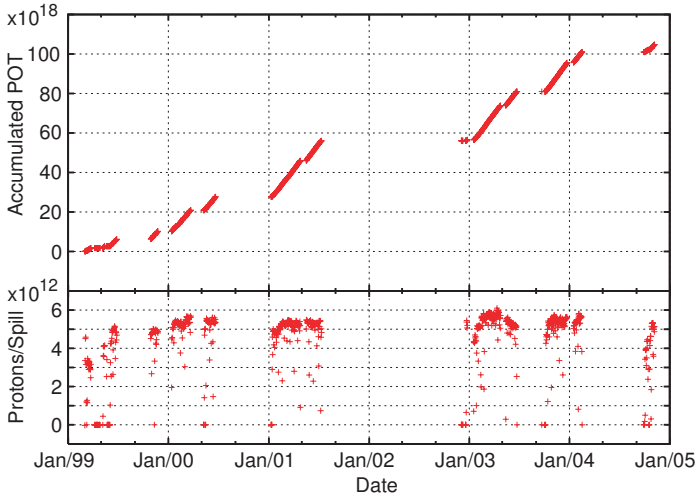

Figure 2.2: Protons on Target (POT). The horizontal axis is date. The upper plot shows integrated POT since March 1999, and the bottom plot shows the average POT per spill for one day.

and monitor the beam. The measurements from the two chambers located just before the target are used to estimate the beam size and divergence; this information is an input to the Monte Carlo (MC) beam simulation.

2.1.2 Target and Horn Magnets

The proton beam target is a cylindrical piece of aluminum, 66 cm in length and 3 cm diameter (2 cm before November 1999). Protons hit the target, producing secondary particles which are mostly pions. Two magnetic horns are used to focus the positively charged particles in the forward direction. A pulsed current of 2 ms duration and 250 kA amplitude (200 kA before November 1999) is supplied to the horns every 2.2 s (synchronized with the proton beam spills). The current creates a toroidal magnetic field that focuses positively charged particles and defocuses negatively charged ones. The first horn is 0.70 m in diameter and 2.37 m long. The target is located inside the first horn and serves as the inner conductor. The second horn is 1.65 m in diameter and 2.76 m in length, located 10.5 m downstream of the first; its purpose is to refocus over-bent low energy pions and under-bent high energy pions. Both horns are cylindrically symmetric. Figure 2.3 shows a diagram of the horns, with the current direction and induced magnetic field labeled. The transverse momentum focusing of the horns is about 100 MeV/m, and the typical energy of the focused pions is 2-3 GeV. In the configuration with 3 cm target diameter and 250 kA current, the maximum magnetic field in the horn

is 33 kG at the surface of the target. The horn current is monitored so that good beam spills can be selected for data analysis. According to simulation, the flux of neutrinos with energy above 0.5 GeV is 22 times greater with the horns at 250 kA than without the horns.

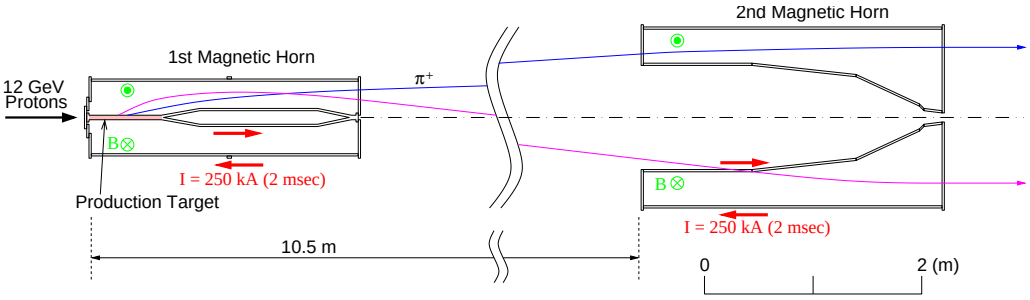

Figure 2.3: Diagram of the horn magnets.

2.1.3 Decay Pipe and Beam Dump

The focused pions enter a 200 m long decay volume where they decay, producing muon neutrinos via the process $\pi^+ \rightarrow \mu^+\nu_\mu$. The decay volume is filled with helium gas at 1 atm rather than air to avoid the loss of pions by absorption and the uncontrollable production of pions. The decay volume has a diameter of 1.5 m for the first 10 m, a diameter of 2 m for the next 90 m, and a diameter of 3 m for the remaining 100 m. There is a beam dump located at the end of the decay pipe to stop all the particles except the neutrinos. The beam dump consists of 3.5 m of iron, 2 m of concrete, and 60 m of soil.

2.1.4 Secondary Beam Monitors

MUMON

Just downstream of the iron and concrete beam dump, a muon monitor (MUMON) measures the profile and intensity of the muons every spill. Because of the energy loss in the iron and concrete, only muons with momentum of 5.5 GeV/c or greater reach the MUMON. Since muons and neutrinos are produced by the two-body decay of pions, the center of the muon profile corresponds to the neutrino beam center. Thus, the MUMON monitors the direction of the neutrino beam. The goal is to control the beam direction within 3 mrad, as a change in the beam direction of 3 mrad corresponds to a change in the neutrino flux at SK of approximately 1%. As seen in the figure, the beam direction for the entire K2K run is very stable (<1 mrad variation) and much better than the design requirements (3 mrad).

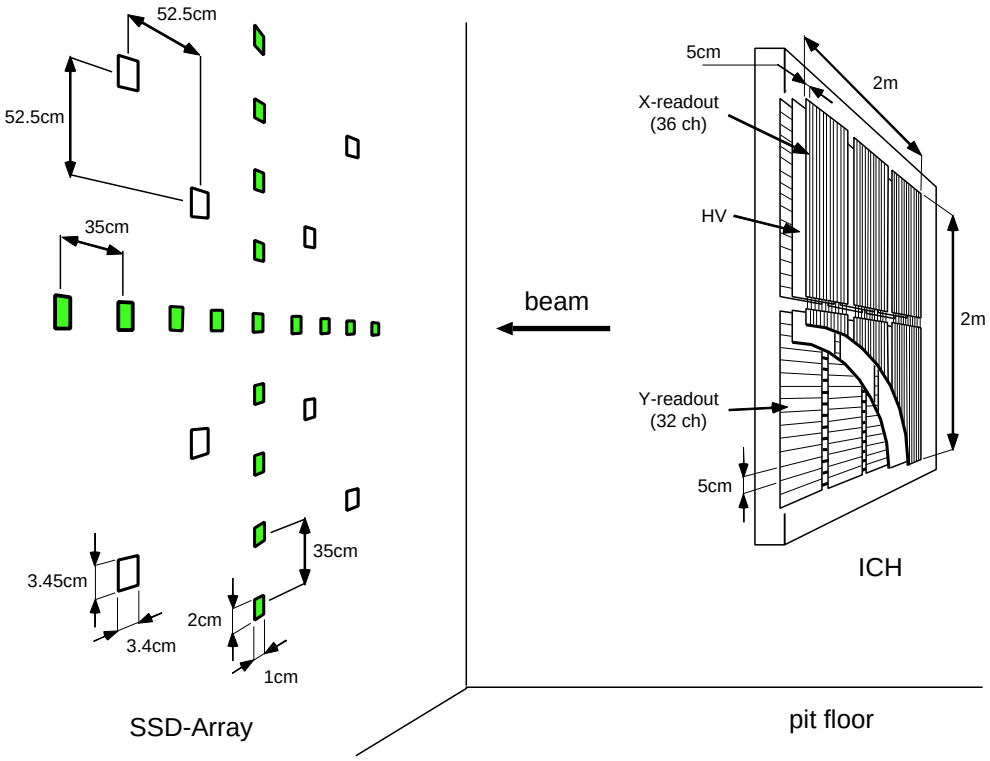

Figure 2.4: Diagram of MUMON. The ionization chamber is shown on the right; the silicon pad array is shown on the left.

The MUMON consists of ionization chamber and an array of silicon pad detectors, as shown in Figure 2.4. The ionization chamber consists of one anode plane and two cathode planes; one cathode plane has 32 vertical strips and the other has 36 horizontal strips. The spacing between the cathode strips is 5 cm. The gap between each cathode plane and the anode is 1 cm. Each plane is divided into six modules (three horizontally, two vertically) that are each 60 cm in the horizontal direction and 90 cm in the vertical direction. There is space between the modules (25 cm horizontally and 15 cm vertically), but the corresponding cathode strips on adjacent modules are electrically connected, making each strip effectively 180 cm long. A voltage of -500 V is applied to the anode. The gaps between anode and cathode are filled with Argon gas. Figure 2.5 shows the center of the muon profile measured by the ionization chamber for the duration of the experiment. The upper (lower) plot shows the profile center in the horizontal (vertical) direction. The black center line represents the direction to SK measured by GPS. The surrounding red lines show ± 1 mrad from the black center line.

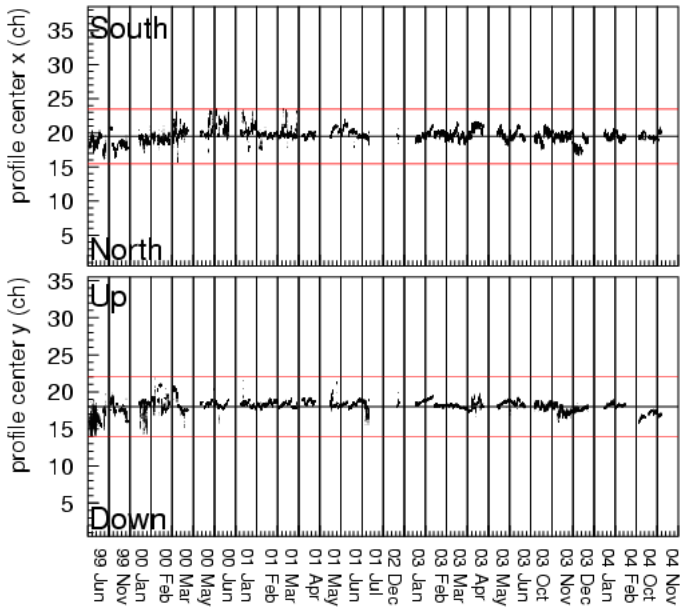

Figure 2.5: Center of the muon profile as measured by the ionization chamber of the MUMON. Upper: Horizontal direction. Lower: Vertical direction.

The silicon pad array is located downstream of the ionization chamber. There are 17 silicon pad detectors each with a sensitive area of 1 cm $\times$ 2 cm and a depletion layer with thickness 300 μm arranged along a horizontal line and a vertical line, with a spacing of 35 cm. There are nine larger silicon pad detectors each with a 3.4 cm $\times$ 3.05 cm sensitive area and a depletion

layer thickness of 375 μm that are arranged along the diagonals with 74.2 cm spacing. The bias voltage for the pads is 100 V and 70-80 V for the small and large pads, respectively.

PIMON

A pion monitor (PIMON) is installed just downstream of the horns to measure the momentum (p_π) and angular (θ_π) distribution of the focused pions before they enter the decay volume. For pion decay into a muon and muon neutrino, the energy of the neutrino can be calculated given the momentum of the pion and the angle (θ) of the outgoing neutrino with respect to the pion's initial direction in the lab frame.

$$E_\nu = \frac{m_\pi^2 - m_\mu^2}{2(E_\pi - p_\pi cos\theta)} \tag{2.1}$$

where m_μ is the muon mass, m_π is the pion mass, and $E_\pi = \sqrt{p_\pi^2 + m_\pi^2}$ is the pion energy in the lab frame. Given Equation 2.1 and the fact that pion decay is isotropic in the rest frame of the pion, the neutrino energy spectrum at any distance can be extrapolated from the (p_π, θ_π) distributions. The PIMON data is one method used in K2K to calculate the expected ratio of neutrino flux at the far detector to that at the near detector, which is crucial to the neutrino oscillation analysis. The PIMON detector is only put into the beam line when it is needed for the pion measurement; it is never present during normal neutrino data-taking.

The PIMON is a gas imaging Cherenkov detector which consists of a gas vessel, a spherical mirror, and 20 photomultiplier tubes (PMTs). Cherenkov photons emitted by pions travelling through the gas are reflected by a section of a spherical mirror and focused on the array of PMTs. The gas vessel is filled with freon gas (C_4F_8). The refractive index n of the gas can be adjusted by changing the gas pressure. Changing the refractive index changes the momentum threshold for pions to emit Cherenkov radiation. At refractive indices above $n = 1.00242$, the 12 GeV primary protons emit Cherenkov photons and are a significant background to the pion measurement. The spherical mirror is wedged-shaped and covers 1/30 of the beam; azimuthal symmetry of the beam is assumed. The reflection angle of the Cherenkov photons is 30 degrees with respect to the beam direction. The array of PMTs is set 3 m away from the beam to minimize radiation damage. The sensitive area of the photocathode of each PMT is 8 mm in diameter, and the PMTs are arranged vertically with 35 mm spacing.

A diagram of the PIMON is shown in Figure 2.6. The lower part of the figure shows the wedge-shaped spherical mirror in the beam view. The concentric circles represent the Cherenkov light produced by pions. The upper

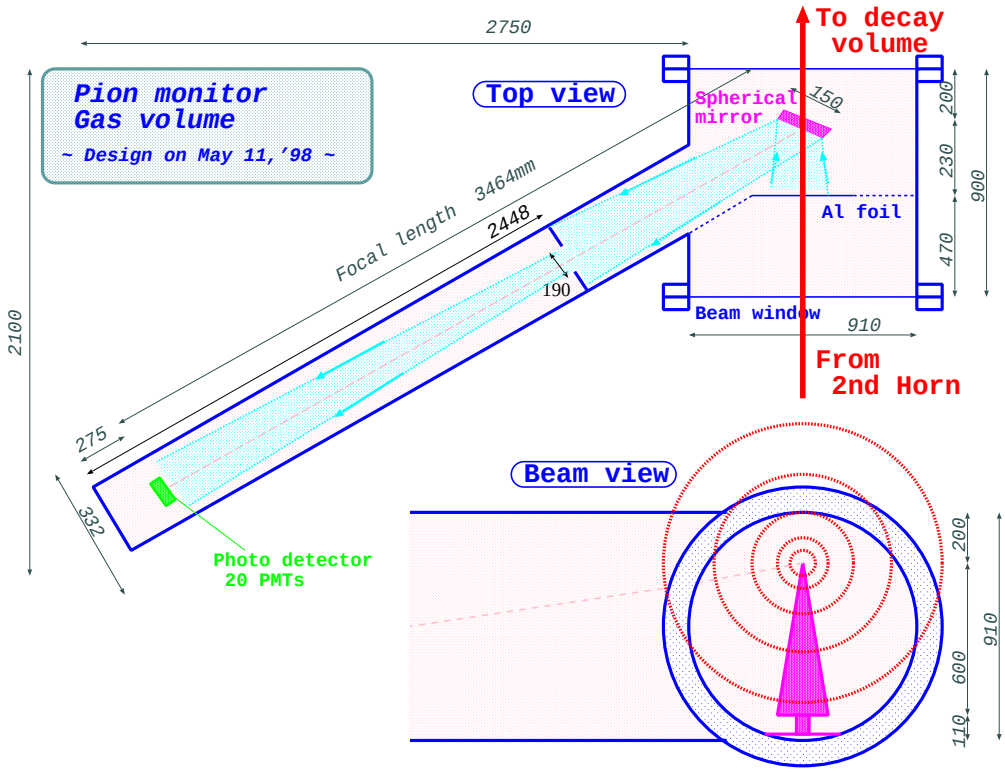

Figure 2.6: Diagram of PIMON. The upper part of the figure shows the PIMON from above, where the arrow indicates the beam direction. The lower part of the figure shows the PIMON in the beam view, where the beam is travelling into the page.

part of the figure shows the PIMON as viewed from the top, with the beam travelling upward on the page. The Cherenkov photons strike the mirror and are reflected toward the PMT array.

Due to the characteristics of the spherical mirror, photons propagating in the same direction are focused at the same point on the focal plane. Thus, the direction of the pion is determined by the location of the Cherenkov image. The momentum of the pion is determined by the size of the Cherenkov ring.

2.2 Neutrino Detectors

A set of near detectors is located at KEK 300 m downstream of the production target. The near detector consists of a 1 kiloton water Cherenkov detector (1 KT), a scintillating fiber detector (SciFi), a scintillating bar detector (SciBar) or a lead glass calorimeter (LG), and a muon range detector (MRD). For the K2K-I period, the LG was placed between SciFi and the MRD, but it was replaced by SciBar for the K2K-II period. Figure 2.7 shows a diagram of the near detector. SK [9] is a 50 kiloton water Cherenkov detector located 250 km away from KEK that is used as the far detector for K2K.

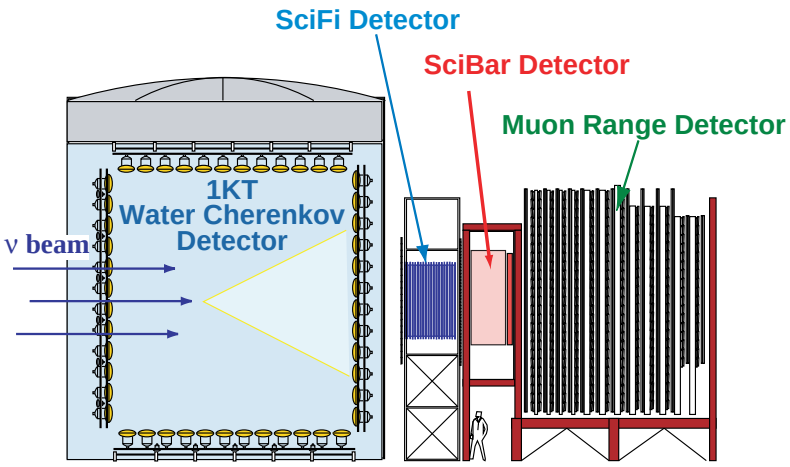

Figure 2.7: K2K near detectors for the K2K-II period.

2.2.1 1 KT Detector

The 1 KT is a cylindrical tank, 10.8 m tall and 10.8 m in diameter, that is filled with 1000 tons of pure water. It is a miniature version of the SK detector [9] and uses the same target material and instrumentation. The tank is optically separated into an inner detector (ID) and outer detector (OD) using

opaque black sheets and reflective Tyvek® sheets. The ID is cylindrical with an 8.6 m height and an 8.6 m diameter and has 680 50-inch diameter PMTs facing the inside of the tank, giving 40% photocathode coverage. The ID PMTs view the Cherenkov light produced by neutrino events in the fiducial volume of the detector. The OD has 68 20-inch diameter PMTs facing outward to veto incoming particles. The 1 KT is used to measure the ν_μ interaction rate in water and the ν_μ energy spectrum, which are extrapolated and compared with the measurements made at SK. Details of the 1 KT detector can be found in [10].

2.2.2 SciFi Detector

The SciFi detector is a tracking detector consisting of alternating layers of tracking modules and water targets. There are 20 tracking modules in total and 19 water targets. The tracking modules are 2.6 m by 2.6 m and consist of two sheets of scintillating fibers. In one sheet, the fibers are arranged vertically, and in the other sheet, the fibers are arranged horizontally. Each sheet is two fibers thick; the fibers are each 0.692 mm in diameter. The fiber sheets are coupled to an image intensifier tube and have a CCD readout system. The water target is contained in extruded aluminum tubes. The SciFi detector is used to measure the ν_μ energy spectrum and reconstruct charged particle tracks with high resolution. See [11],[12] for more information on the SciFi detector.

2.2.3 Lead Glass Calorimeter

For the K2K-I period, the LG is located between SciFi and the MRD. It is replaced by SciBar for K2K-II. The LG is made of 600 cells. Each cell is 12 cm $\times$ 12 cm $\times$ 34 cm and is attached to a 3-inch diameter PMT. Light is guided to the PMT by a light guide cylinder that is also made of lead glass. The LG is used to distinguish electrons from muons by the energy deposition.

2.2.4 SciBar Detector

The SciBar detector will be described in detail in Chapter 3.

2.2.5 Muon Range Detector

The MRD consists of 12 layers of iron absorber located in between 13 layers of horizontal and vertical drift tubes. Each layer is 7.6 m by 7.6 m; the four upstream iron plates are 10 cm thick and the remaining iron plates are 20 cm thick. There are a total of 6632 drift tubes; each tube is aluminum with a

cross sectional area of 5 cm by 7 cm. Each tube is filled with P10 gas (Ar:CH_4 = 90%:10%). The mass of the MRD is 915 tons, 864 of which is iron.

The purpose of the MRD is to monitor the stability of the neutrino beam direction, profile, and spectrum by detecting muons produced by charged-current (CC) neutrino interactions in the iron target. The MRD is also used to identify muons produced by CC neutrino interactions in the upstream detectors and to measure the energy of these muons in combination with the other detectors. An accurate measurement of the muon energy is necessary to reconstruct the incident neutrino's energy.

The MRD tracking efficiency is 66%, 95%, and 97.5% for tracks that traverse one, two and three iron layers, respectively; for longer tracks, the efficiency approaches 99%. The muon energy is reconstructed using a range to energy lookup table based on GEANT3 MC [13, 14]. The uncertainty in the muon energy due to differences among various calculations of the relationship between muon energy and range is 1.7%. The uncertainty in the weight of the iron is 1%. Thus, the systematic uncertainty in the MRD energy scale is conservatively quoted to be the sum of these uncertainties, 2.7%. The energy acceptance of the detector is 0.3 to 2.8 GeV with a resolution fo 0.12 GeV for forward-going muons; the maximum muon energy is about 3 GeV, so the MRD covers almost the entire spectrum. The angular resolution is about 5 degrees, and the vertex resolution is approximately 2 cm.

More detailed information on the MRD.can be found in reference [15].

2.3 Results from K2K

The K2K collaboration's final neutrino oscillation results for muon neutrino disappearance ($\nu_\mu \rightarrow \nu_\tau$) are published [16]. The best fit values of the oscillation parameters in the physical region are $(\sin^2 2\theta_{23}, \Delta m^2_{23}) = (1.0, 2.8 \times 10^{-3}(\mathrm{eV}/c^2)^2)$. Figure 2.8 shows the allowed region of oscillation parameters from K2K's result compared with the Super-Kamiokande atmospheric neutrino result. K2K's final result for electron neutrino appearance (a search for $\nu_\mu \rightarrow \nu_e$) is also published [17].

The high neutrino interaction rate in the near detectors enables the K2K experiment to make measurements of neutrino-nucleus interaction cross sections. In addition to the study described in this thesis, K2K has final results for the neutral-current π^0 production cross section [10], the charged-current coherent pion production cross section [18], and a study of the charged-current quasi-elastic interaction [19]. A few other cross section measurements are currently in the process of being finalized.

For further reference, [16] and [20] include detailed descriptions of the K2K experiment.

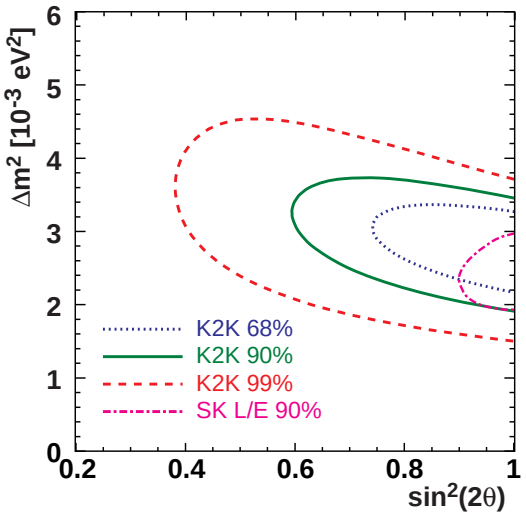

Figure 2.8: K2K's result for allowed regions for oscillation parameters compared with the Super-Kamiokande result.

Chapter 3

The SciBar Detector

The SciBar detector was installed to upgrade the near detector. The main purpose of the detector was to increase the sensitivity in measuring low momentum particles which is important for the oscillation analysis. A prototype for SciBar replaced the lead-glass calorimeter in January 2003 at the beginning of the K2K-II period. The full detector was installed in summer 2003. SciBar took data from October 2003 until November 2004; 2.1×10^{19} P.O.T. were accumulated during this time period. This data is used for the analysis presented in this dissertation. Detailed descriptions of the SciBar detector can be found in [21], [22], and [23].

3.1 Overview

The purpose of the SciBar detector is to measure the neutrino energy spectrum and to study neutrino interactions with a high detection efficiency especially for low momentum particles. SciBar consists of 14,848 scintillating bars. Groups of 116 bars are arranged side by side horizontally or vertically to make one plane. One layer consists of one horizontal plane and one vertical plane; there are 64 layers total. SciBar is a fully active detector. The total volume is 1.7 m $\times$ 3 m $\times$ 3 m, for a total mass of $\sim$15 tons. The scintillation light produced by charged particles passing through the detector material is guided by wavelength shifting (WLS) fibers to 64-channel multi-anode photomultiplier tubes (MAPMTs). Figure 3.1 shows a diagram of the SciBar detector.

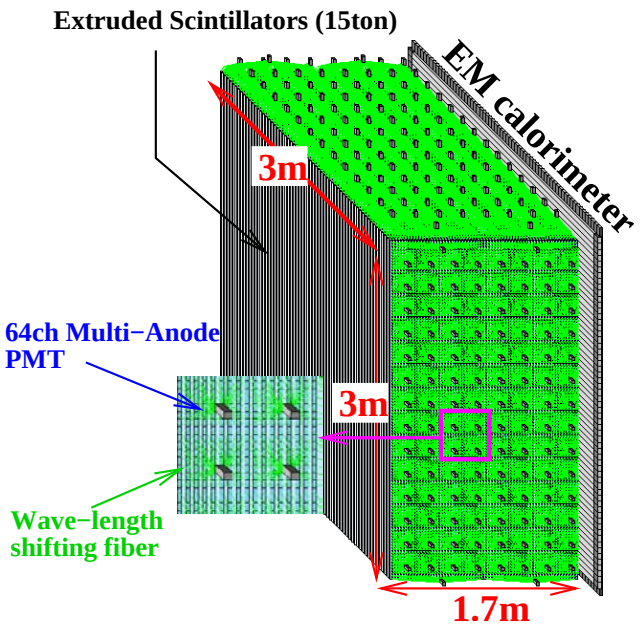

Figure 3.1: Diagram of SciBar.

3.2 Scintillating Bars and WLS Fibers

The extruded scintillator bars are produced by FNAL. The bars are made of polystyrene (C_8H_8), PPO (1%), and POPOP (0.03%). Each bar is 1.3 cm $\times$ 2.5 cm $\times$ 300 cm and has a 0.25 mm thick reflective coating made of TiO_2. The peak of the emission spectrum for the scintillator is at 420 nm as shown in Figure 3.2.

A 1.5 mm diameter wavelength shifting (WLS) fiber (Kuraray Y11(200)MS) is inserted in a 1.8 mm diameter hole in each bar to guide the scintillation light to MAPMTs. The attenuation length of the fibers is approximately 350 cm, which is much longer than the attenuation length of the scintillator (about 10 cm). Each fiber has a polystyrene core (refractive index n=1.56) which contains the wavelength shifting material with a concentration of 200 ppm. The fibers have an inner cladding of acrylic (n=1.49) and an outer cladding of polyfluor (n=1.42). The absorption and emission spectra for the WLS fibers is shown in Figure 3.3. The absorption peak for the fibers is at 430 nm (matching the emission peak for the scintillator), and the emission peak for the fibers is at 476 nm.

A diagram of a bar with the fiber inserted is shown in Figure 3.4.

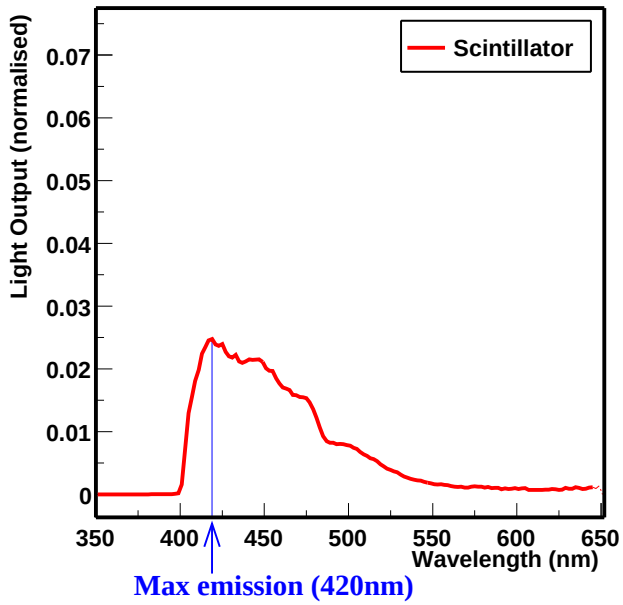

Figure 3.2: Emission spectrum for scintillating bars

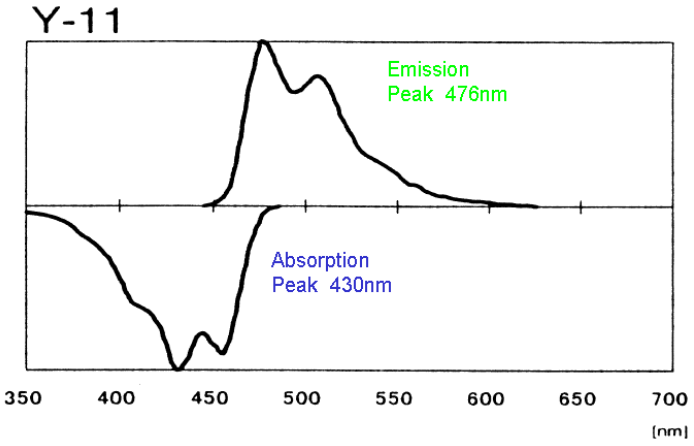

Figure 3.3: Absorption and emission spectra for WLS fibers

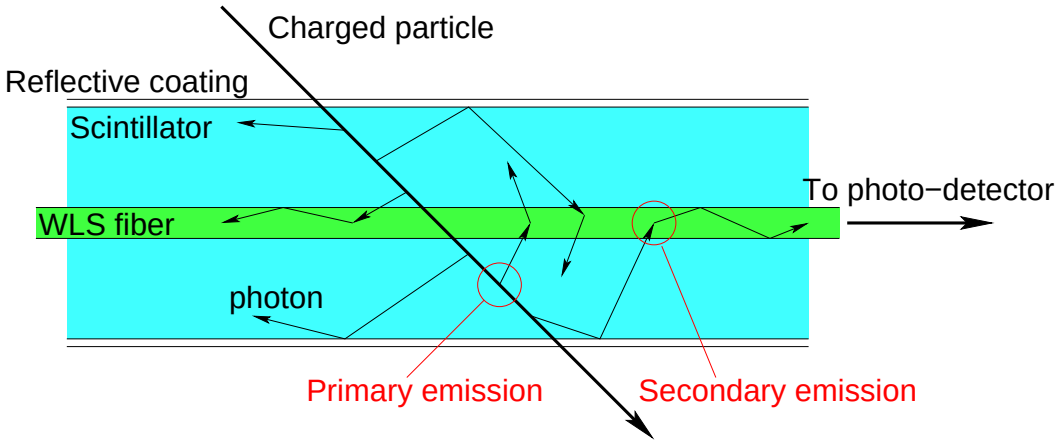

Figure 3.4: Cross section of a scintillating bar with fiber.

3.3 MAPMTs

The scintillation light is detected by Hamamatsu H8804 MAPMTs. Each MAPMT has 64 channels arranged in an 8×8 array. Each pixel is 2 mm × 2 mm. The cathode material is bialkali, with a quantum efficiency of 21% at a wavelength of 390 nm. The cathode is sensitive to wavelengths between 300 and 650 nm. A typical channel gain is 3×10^5 at a supply voltage of 800 V. The basic properties such as gain and linearity are measured for each channel before installation. The non-linearity of the output signal vs. input charge is 5% at 200 photoelectrons (p.e.) at a gain of 5×10^5. Crosstalk in the MAPMT is approximately 3% in neighboring channels, according to a measurement [24].

Groups of 64 fibers are bundled together in an 8×8 array with the fixture shown in Figure 3.5. The fibers are spaced so that they can be precisely aligned with the pixels of the MAPMT.

The energy resolution of the MAPMT is 40% ± 10%. This value is determined using beam data to tune the dE/dx per plane for muons in the MC to match the data.

3.4 Readout

SciBar's readout system [25] consists of a front-end electronics board (FEB) attached to each MAPMT and a back-end VME module. The front-end electronics uses VA/TA ASICs. The VA is a 32-channel pre-amplifier chip with a shaper and multiplexer. The TA provides timing information by taking the "OR" of 32 channels. Each FEB uses two VA/TA packages to read 64 analog signals and two timing signals for each MAPMT. Each back-end VME

Figure 3.5: Fibers in 8×8 configuration, ready to be aligned with face of MAPMT.

board controls the readout of eight FEBs. Flash ADCs are used to digitize the charge information, and TDCs are used to process the timing information. The pedestal width is approximately 0.3 p.e. The TA timing resolution is measured using timing signals from cosmic-ray muons and is found to be 1.3 ns.

3.5 Gain Monitoring System

In order to measure and correct for gain drift, a gain calibration system is used. Light is produced by four blue LEDs monitored by PIN photodiodes. Each LED is used to deliver light to 56 MAPMTs through clear fibers. Each clear fiber is connected to a light injection module that delivers the LED light to a bundle of WLS fibers, illuminating all 64 WLS fibers equally. The spectrum emitted by the WLS fibers in response to the LED is very similar to the spectrum emitted in response to scintillation light, meaning that the LED signal mimics the scintillation signal well. The gain is monitored by comparing the signal in the MAPMT due to the LED with the signal from the PIN photodiode. A diagram of the system is shown in Figure 3.6.

The system shows that the gains are stable within 5% for the entire period of operation. Figure 3.7 shows the relative gain as a function of time for a typical channel. The gain monitoring system can also be used to identify dead channels.

3.6 Energy Calibration

Cosmic-ray muons are used to calibrate the light yield of each channel. The average light yield per bar is measured to be about 20 p.e. for a minimum

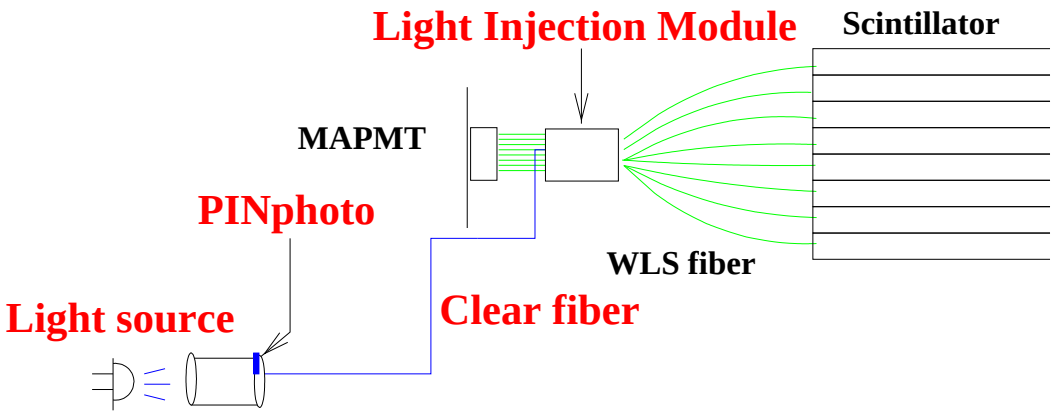

Figure 3.6: Gain Monitoring System.

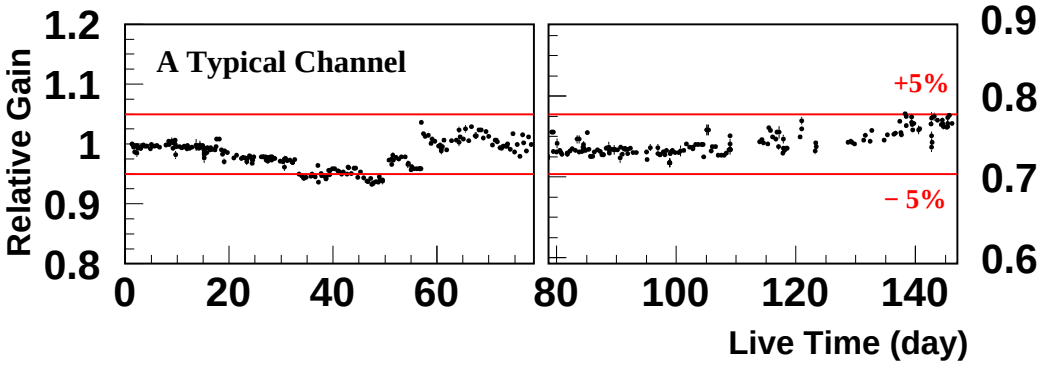

Figure 3.7: Relative gain of a typical channel over time

ionizing particle. The stability of the energy calibration over time is also monitored. Figure 3.8 shows the light yield of one strip over time. The upper figure shows the light yield before correction for gain variation, and the lower figure shows the light yield after the correction. The light yield is found to be stable within 1% for the whole period of operation after the correction.

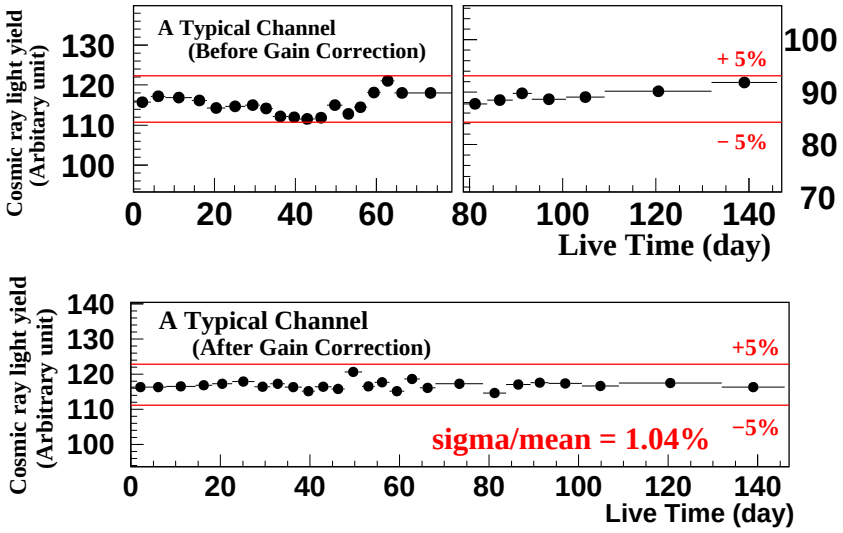

Figure 3.8: Light yield in a single strip over time. Upper: before correction for gain variation, Lower: after correction

3.7 Measurement of Birks' Constant

For heavy particles (such as protons), the light yield from scintillation increases non-linearly with the energy loss of the particle.

$$\frac{\Delta E_{vis}}{\Delta E} \propto \frac{1}{1 + c\frac{dE}{dx}(exp)} \tag{3.1}$$

where ΔE_{vis} is the visible energy from scintillation, ΔE is the actual energy loss and $\frac{dE}{dx}(exp)$ is the expected energy loss per distance travelled [26]. c is called Birks' constant, and it must be measured.

Birks' constant was measured for SciBar using a small prototype detector at KEK and a proton beam. Figure 3.9 shows the result of the measurement. The measured value for Birks' constant is $0.0208 \pm 0.0003(\text{stat}) \pm 0.0023(\text{syst})$ cm/MeV.

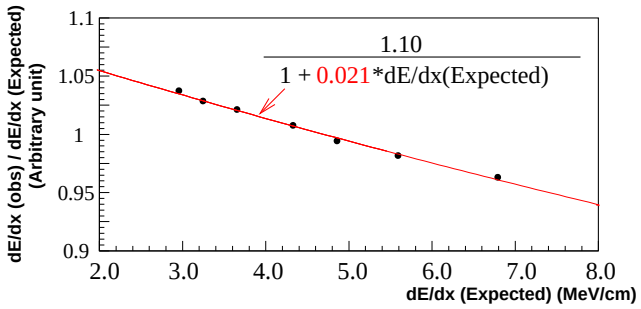

Figure 3.9: Ratio of visible energy loss to expected energy loss as a function of expected $\frac{dE}{dx}$ as measured with a prototype of SciBar in a proton beam. The red line shows the best fit to the data points.

3.8 Data Acquisition

Pedestal, LED (for gain monitoring), and cosmic-ray data are taken at the same time as neutrino beam data. Figure 3.10 shows the timing structure for data acquisition. LED and pedestal triggers are initiated after the beam trigger. Then cosmic-ray triggering is enabled.

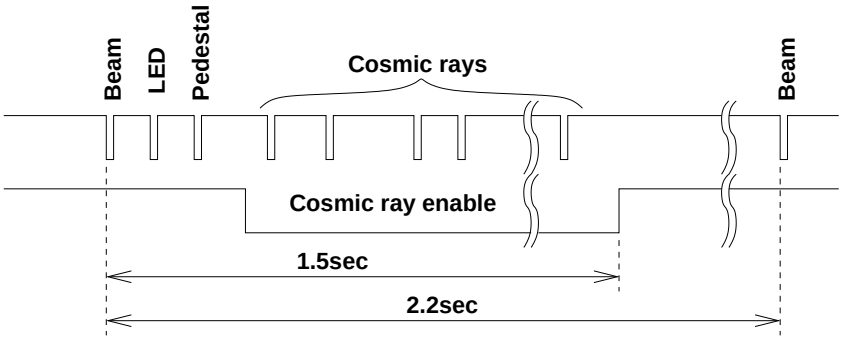

Figure 3.10: Timing structure for data acquisition

3.9 Electron Catcher

Just downstream of SciBar is an electromagnetic calorimeter called the Electron Catcher (EC). The purpose of the EC is to measure the electron neutrino contamination in the beam and π^0 production in neutrino interactions. The EC consists of one plane of horizontal bars and one plane of vertical bars. Each bar is made of lead and scintillating fibers. The bars were originally

made for the CHORUS neutrino experiment at CERN [27]. Each plane is 4 cm thick in the beam direction with cross sectional areas of 2.7 m $\times$ 2.6 m and 2.6 m $\times$ 2.5 m, respectively. The EC adds an additional 11 radiation lengths in the beam direction (the main part of SciBar is about four radiation lengths in the beam direction). The energy resolution for electrons is $14\%/\sqrt{E(\mathrm{GeV})}$ as measured by a test beam [27].

Chapter 4

Simulation

4.1 Beam simulation

The neutrino beam simulation consists of three parts: 1) the proton beam simulation, 2) simulation of the production of secondary particles via interaction of protons with the target, and 3) simulation of the decays of secondary particles into neutrinos and other particles. The geometry of the beam line is implemented in GEANT3 [13, 14]; particles are tracked by GEANT until they decay or are absorbed. Neutrino tracks are extrapolated along a straight line to the near detector and to Super-Kamiokande (SK) so the neutrino flux and energy spectrum at both sites can be predicted.

4.1.1 Proton Beam Characteristics

Protons with a kinetic energy of 12 GeV are injected into the aluminum target material. As mentioned in Section 2.1.1, measurements of the proton beam profile and divergence made by two segmented plate ionization chambers located just before the target are used as inputs for the beam simulation. The bunch structure of the neutrino beam is simulated based on real beam data.

4.1.2 Production of Hadrons

The Sanford-Wang parametrization [28],[29] is an empirical parametrization for the cross section of hadron production given by

$$\frac{d^2\sigma}{d\Omega dp} = C_1 p^{C_2} \left(1 - \frac{p}{p_B}\right) \times \exp\left(-\frac{C_3 p^{C_4}}{p_B^{C_5}} - C_6\theta(p - C_7 p_B \cos^{C_8}\theta)\right) \quad (4.1)$$

where $\frac{d^2\sigma}{d\Omega dp}$ is the double differential cross section of particle production per interacting proton, p_B is the momentum of the beam particle, p is the momentum of the outgoing hadron, θ is the angle between the outgoing hadron and the beam axis, and the C_i's are parameters to be fitted.

K2K's simulation of positive pion production uses the 'Cho-CERN compilation' result for the C_i's. The data used in this compilation mostly come from the results of Cho *et al.* [30] for proton-beryllium interactions. For use in our beam simulation, this cross section is scaled to account for the difference between beryllium and aluminum as target nuclei. For the production of negative pions, the C_i's from Cho *et al.* [30] are used; for kaon production, the parameters from [31] are used.

The secondary particles are tracked by GEANT through the horn magnets and the decay volume until they decay or are absorbed.

4.1.3 Decays

GEANT treats different types of neutrinos identically; therefore K2K uses a custom-made simulation for the decay of particles into neutrinos.

In our simulation, charged pions decay into muon and muon neutrino ($\pi^+ \to \mu^+\nu_\mu$, $\pi^- \to \mu^-\overline{\nu}_\mu$) with a branching ratio of 100%.

The following kaon decays are considered:

- $K^+ \to \mu^+\nu_\mu$, $K^- \to \mu^-\overline{\nu}_\mu$
- $K^+ \to \pi^0 e^+\nu_e$, $K^- \to \pi^0 e^-\overline{\nu}_e$
- $K^+ \to \pi^0\mu^+\nu_\mu$, $K^- \to \pi^0\mu^-\overline{\nu}_\mu$
- $K^0_L \to \pi^- e^+\nu_e$, $K^0_L \to \pi^+ e^-\overline{\nu}_e$
- $K^0_L \to \pi^-\mu^+\nu_\mu$, $K^0_L \to \pi^+\mu^-\overline{\nu}_\mu$

Other kaon decay modes are ignored because of low branching ratios. The branching ratios for the kaon decays listed above are taken from the Particle Data Group [32]. For the three-body decay modes (K_{l3}), the Dalitz plot density [32],[33] of $V - A$ theory is used to obtain the neutrino energy in the kaon rest frame.

Muons decay into an electron and two neutrinos ($\mu^+ \to e^+\nu_e\overline{\nu}_\mu$, $\mu^- \to e^-\overline{\nu}_e\nu_\mu$) with a branching ratio of 100%. The energy and angular distributions

of the neutrinos from muon decay are calculated using Michel spectra of $V-A$ theory [33]; the polarization of the muon is considered.

4.1.4 Results of Beam Simulation

Figure 4.1 shows the prediction for the neutrino energy spectrum at the near detector and at SK. The beam is 97.3% pure muon neutrino at the near detector and 97.9% pure muon neutrino at SK. The prediction of the beam simulation for the muon neutrino energy spectrum is consistent with measurements made by the PIMON (described in Chapter 2.1.4) and by the HARP experiment [34]. The HARP experiment at CERN studied the cross section for pion production in the interactions of 12.9 GeV/c protons with an aluminum target. Figure 4.2 compares the muon neutrino energy spectrum at the near detector and at SK predicted by the beam MC to the predictions from the PIMON measurements and the HARP experiment.

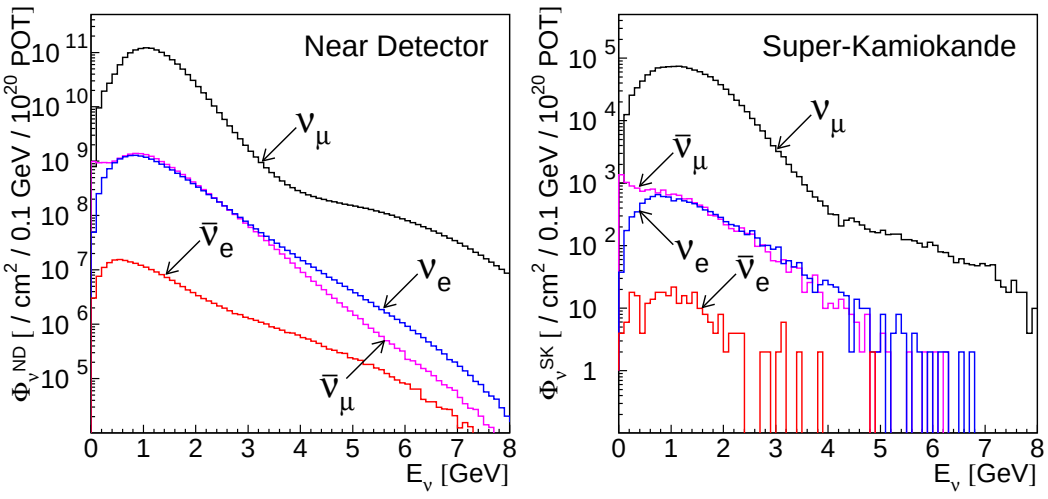

Figure 4.1: Beam MC prediction for the neutrino energy spectrum at the near detector (left) and at SK (right).

4.1.5 Correction to Energy Spectrum Based on Measurement

Data from all the near detectors are used to fine-tune the simulated neutrino energy spectrum [16]. The data are fitted to the MC expectation, with seven energy spectrum reweighting factors as free parameters in the fit. The best fit values of these parameters are then used to reweight the MC predicted energy spectrum. The weighting factors are given in Table 4.1, and

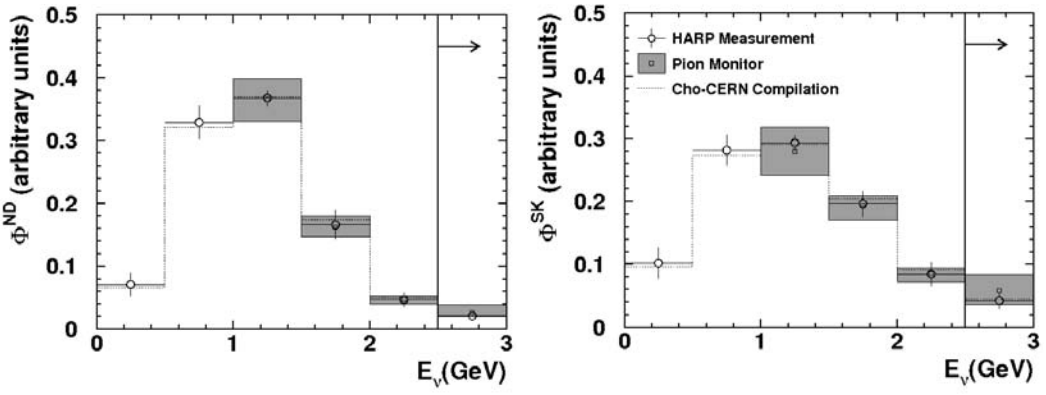

Figure 4.2: Muon neutrino energy spectrum predicted by beam MC (which uses the Cho-CERN compilation), PIMON, and HARP at the near detector (left) and at SK (right).

the error matrix for the weighting factors is shown in Table 4.2. Figure 4.3 shows the energy spectrum for all neutrino events in the fiducial volume of SciBar with and without the reweighting.

Table 4.1: Neutrino Energy Spectrum Weighting

E_ν (GeV)	Weighting factor
0.00-0.50	1.657
0.50-0.75	1.107
0.75-1.00	1.154
1.00-1.50	$\equiv 1$
1.50-2.00	0.911
2.00-2.50	1.069
2.50-3.00	1.152
>3.00	1.260

4.2 Simulation of Neutrino Interactions

The K2K experiment uses a neutrino interaction simulation package called NEUT [35]. NEUT was originally developed for the Kamiokande experiment and has been updated for use in the Super-Kamiokande experiment and K2K. The following interactions of neutrinos with matter are considered:

- (quasi)elastic scattering, $\nu N \to \ell N'$
- single meson production via baryon resonance, $\nu N \to \ell N' m$

Table 4.2: Each element in this matrix is $\mathrm{sign}[M_{ij}] \cdot \sqrt{|M_{ij}|}$, where M is the error matrix for the energy spectrum weighting factors.

0.4386	-0.0316	0.0728	-0.0221	-0.0076	-0.0348	0.0081
-0.0316	0.0751	0.0197	0.0190	0.0062	0.0129	0.0243
0.0728	0.0197	0.0600	0.0338	0.0163	0.0344	0.0171
-0.0221	0.0190	0.0338	0.0404	-0.0186	0.0453	0.0220
-0.0076	0.0062	0.0163	-0.0186	0.0528	-0.0585	0.0511
-0.0348	0.0129	0.0344	0.0453	-0.0585	0.1367	-0.1014
0.0081	0.0243	0.0171	0.0220	0.0511	-0.1014	0.1835

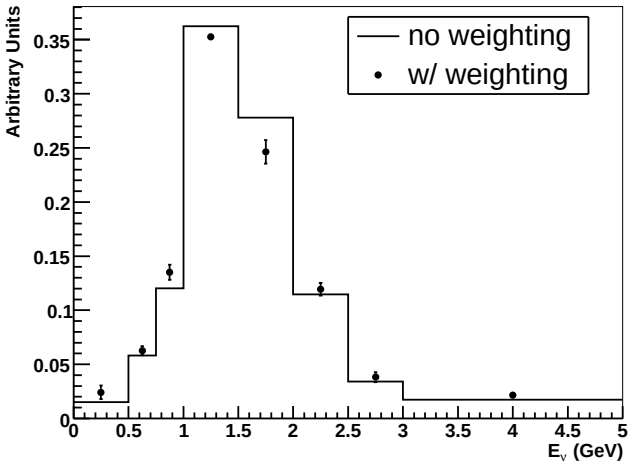

Figure 4.3: The energy spectrum for all neutrino events in the fiducial volume of SciBar with and without the reweighting. (Both distributions are normalized to have unit area.)

- deep inelastic scattering, $\nu N \rightarrow \ell X$
- coherent π production, $\nu A \rightarrow \ell \pi A$

where ν is a neutrino, N is a nucleon, ℓ is a lepton, m is a meson, X is a system of hadrons, π is a pion, and A is a nucleus. The interaction of neutrinos with electrons is not considered since the cross section is negligible compared to the above interactions in the $\sim$1 GeV energy region.

4.2.1 (Quasi)elastic Scattering

For charged-current (CC) quasi-elastic scattering of a neutrino off a free nucleon, $\nu_\ell n \rightarrow \ell^- p$, NEUT uses the hadronic current, J_λ, as given by Llewellyn Smith [36]:

$$< p|J_\lambda|n > \;\; = \tag{4.2}$$
$$\cos\theta_c \overline{u}(p) \left[\gamma_\lambda F_V^1(q^2) + \frac{i\sigma_{\lambda\nu} q^\nu \xi F_V^2(q^2)}{2M} + \gamma_\lambda \gamma_5 F_A(q^2) + \frac{q_\lambda \gamma_5 F_P(q^2)}{M} \right] u(n)$$

where θ_c is the Cabibbo angle, M is the nucleon mass, q^2 is the lepton momentum transfer, F_V^i are vector form factors, F_A is the axial-vector form factor, and $\xi \equiv \mu_p - \mu_n$ is the difference in proton and neutron magnetic moments. F_P is the pseudoscalar form factor. When the cross section is calculated using the current given above, the terms proportional to F_P are multiplied by m_ℓ^2/M^2 where m_ℓ is the lepton mass; thus the contribution of F_P is negligible for muon and electron neutrino interactions. So the current reduces to

$$< p|J_\lambda|n > = \cos\theta_c \overline{u}(p) \left[\gamma_\lambda F_V^1(q^2) + \frac{i\sigma_{\lambda\nu} q^\nu \xi F_V^2(q^2)}{2M} + \gamma_\lambda \gamma_5 F_A(q^2) \right] u(n) \tag{4.3}$$

The conserved vector current (CVC) hypothesis [37] implies that the vector form factors F_V^1, F_V^2 for the weak interaction can be written in terms of the electric and magnetic Sachs form factors (G_E,G_M) that have been measured to high precision in electron scattering experiments. The axial-vector form factor F_A can only be determined by neutrino scattering. F_A is typically parametrized in the dipole form as

$$F_A = -1.23 \times (1 - \frac{q^2}{M_A^2})^{-2} \tag{4.4}$$

where M_A is called the axial vector mass. In our simulation, M_A is set at 1.1 GeV/c^2 based on near detector data [38]. Given these parametrizations of F_V^1,

F_V^2, and F_A, the cross section for CCQE is calculated using the current given in Equation 4.3.

Figure 4.4 shows the calculated cross sections for the ν_μ and $\overline{\nu}_\mu$ CCQE interactions compared with experimental measurements.

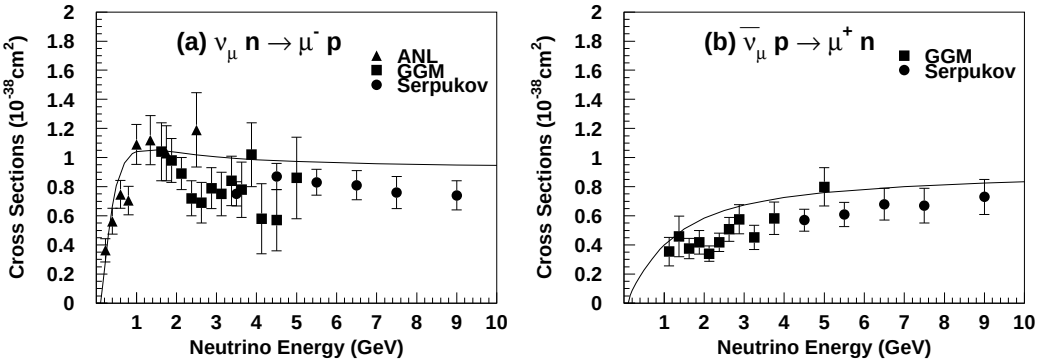

Figure 4.4: NEUT calculated CCQE cross sections compared to experimental measurements. In Figure a), data points are taken from ANL[39], GGM[40], and Serpukov[41]. In Figure b) data points are taken from GGM[42] and Serpukov[41].

The cross sections for neutral current (NC) elastic scattering are estimated using the CCQE cross section and these relations from [43],[44]:

- $\sigma(\nu_\ell p \to \nu_\ell p) = 0.153 \times \sigma(\nu_\ell n \to \ell^- p)$
- $\sigma(\overline{\nu}_\ell p \to \overline{\nu}_\ell p) = 0.218 \times \sigma(\overline{\nu}_\ell p \to \ell^+ n)$
- $\sigma(\nu n \to \nu n) = 1.5 \times \sigma(\nu p \to \nu p)$
- $\sigma(\overline{\nu} n \to \overline{\nu} n) = \sigma(\overline{\nu} p \to \overline{\nu} p)$

4.2.2 Single Meson Production

Rein and Sehgal's model [45],[46] is used to simulate single pion production by baryon resonance excitation, $\nu_\ell N \to \ell N^*$, $N^* \to N'\pi$. In this model, the cross section for each $\ell N \pi$ final state is calculated as a coherent superposition of all the possible contributing resonances.

The differential cross section for the production of a single resonance with mass M and negligible width is given by

$$\frac{d\sigma}{dq^2 dW} = \frac{1}{32\pi m_N E_\nu^2} \frac{1}{2} \sum_{spins} |T(\nu N \to \ell N^*)|^2 \delta(W^2 - M^2), \qquad (4.5)$$

where q^2 is the square of the lepton momentum transfer, W is the invariant mass of the produced baryon, m_N is the nucleon mass, and E_ν is the incident neutrino energy. The finite width of the resonance, Γ, is taken into account by replacing the δ-function by the Breit-Wigner factor

$$\delta(W^2 - M^2) \rightarrow \frac{1}{2\pi} \frac{\Gamma}{(W - M)^2 + \Gamma^2/4}. \tag{4.6}$$

Rein and Sehgal use the relativistic harmonic oscillator quark model of Feynman, Kislinger, and Ravndal [47] to calculate the transition matrix elements $T(\nu N \rightarrow lN^*)$ from a ground state nucleon to a baryon resonance. For the same reasons explained in relation to quasi-elastic cross section, there is only one parameter in this model to be determined by experiment, the axial vector mass, M_A. It is set to 1.1 GeV/c^2 in our simulation based on near detector data [38]. The model for the decay of each resonance to a $N\pi$ final state uses experimental input for resonance mass, resonance width, and $N\pi$ branching ratios.

The cross section for the production of each $N\pi$ final state can be found from from summing the contributions from each resonance, using appropriate factors determined by isospin Clebsch-Gordon rules. The interference of overlapping resonances is taken into account. Our simulation considers 18 baryon resonances in the $W < 2$ GeV/c^2 region.

We use Rein and Sehgal's method for the pion angular distribution for the dominant resonance, $P_{33}(1232)$. For the other resonances, the angular distribution of the pion is isotropic in the resonance rest frame. The MC prediction for the π^+ angular distribution for the $\nu p \rightarrow \mu^- p \pi^+$ mode agrees well with measurement [48].

Figure 4.5 shows the calculated cross sections for the three modes of CC single pion production by muon neutrinos on nucleons compared with experimental measurements.

Our simulation also considers the production of single K and η using the same model.

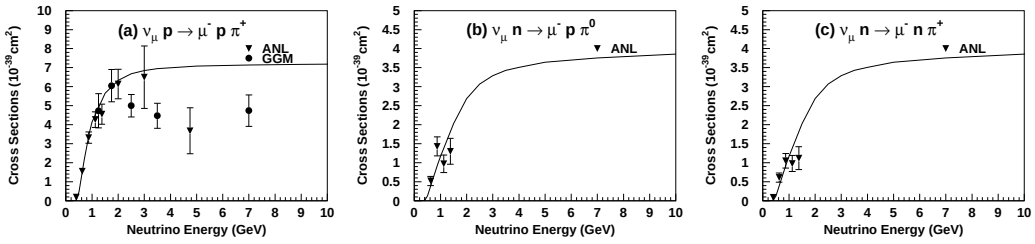

Figure 4.5: NEUT calculated CC single pion cross sections compared to experimental measurements. Data points are taken from ANL[49] and GGM[50]

4.2.3 Deep Inelastic Scattering

The cross section for CC deep inelastic scattering, $\nu N \rightarrow \ell X$, is given by:

$$\frac{d^2\sigma}{dxdy} = \frac{G_F^2 M_N E_\nu}{\pi} \times \left[\left(1 - y + \frac{1}{2}y^2 + C_1 \right) F_2(x, q^2) \pm y \left(1 - \frac{1}{2}y + C_2 \right) xF_3(x, q^2) \right] \tag{4.7}$$

where

$$\begin{aligned} C_1 &= \frac{yM_\ell^2}{4M_N E_\nu x} - \frac{xyM_N}{2E_\nu} - \frac{M_\ell^2}{4E_\nu^2} - \frac{M_\ell^2}{2M_N E_\nu x} \\ C_2 &= -\frac{M_\ell^2}{4M_N E_\nu x} \\ x &= -\frac{q^2}{2M\left(E_\nu - E_\ell\right)} \\ y &= \frac{E_\nu - E_\ell}{E_\nu} \end{aligned} \tag{4.8}$$

G_F is the Fermi coupling constant, M_N is the nucleon mass, E_ν is the incident neutrino energy, q^2 is the square of the lepton momentum transfer, M_ℓ is the outgoing lepton mass, and E_ℓ is the outgoing lepton energy.

For the structure functions F_2 and xF_3, we use the GRV94 formulation [51]. We include the corrections to the GRV94 structure functions in the small q^2 region proposed by Bodek and Yang [52]. This correction is implemented by reweighting DIS events by the factor

$$weight = \frac{Q^2}{Q^2 + 0.188} \tag{4.9}$$

where $Q^2 = -q^2$.

The invariant mass of the hadronic system, W, is required to be greater than 1.3 GeV/c^2 in the calculation. The PYTHIA/JETSET package [53] is used for $W > 2$ GeV/c^2. This package was developed for simulation of high energy interactions, and it does not fit the data well at lower energies. Therefore, a custom made package is used to simulate DIS for $1.3 < W < 2$ GeV/c^2 [54]. In the region of $W < 2$ GeV/c^2, the number of pions in the final state is required to be larger than one since single pion production in that region has already been accounted for.

NC DIS cross sections are calculated using the following relations

determined by experiment [55],[56]:

$$\begin{aligned}\frac{\sigma(\nu_\mu N \to \nu_\mu X)}{\sigma(\nu_\mu N \to \mu^- X)} &= 0.26 \ (E_\nu \leq 3 \text{ GeV}) \\ &= 0.26 + 0.04 \times \frac{E_\nu - 3}{3} \ (3 \text{ GeV} < E_\nu < 6 \text{ GeV}) \\ &= 0.30 \ (E_\nu \geq 6 \text{ GeV})\end{aligned}$$

$$\begin{aligned}\frac{\sigma(\overline{\nu}_\mu N \to \overline{\nu}_\mu X)}{\sigma(\overline{\nu}_\mu N \to \mu^+ X)} &= 0.39 \ (E_\nu \leq 3 \text{ GeV}) \\ &= 0.39 \text{ - } 0.02 \times \frac{E_\nu - 3}{3} \ (3 \text{ GeV} < E_\nu < 6 \text{ GeV}) \\ &= 0.37 \ (E_\nu \geq 6 \text{ GeV})\end{aligned}$$

4.2.4 Coherent Pion Production

Coherent pion production, $\nu A \to \ell A \pi$, is the process in which a neutrino scatters coherently off the entire nucleus with a small energy transfer and produces a pion. This process is simulated based on the model of Rein and Sehgal [57], with the correction described by Marteau *et al.* [58]. However, only the NC coherent process is simulated. The cross section of CC coherent pion production is negligible in K2K's energy range, according to a K2K measurement [18].

4.2.5 Nuclear Effects

The relativistic Fermi gas model of Smith and Moniz [59] is used for the interaction of neutrinos and nucleons inside a nucleus. The Fermi motion of nucleons and the Pauli exclusion principle is taken into account. The momentum distribution of nucleons is assumed to be flat up to p_F, the Fermi surface momentum. For carbon and oxygen, p_F is set to 225 MeV/c; for iron, p_F is set to 250 MeV/c. The effect of Pauli blocking is taken into account by requiring that the outgoing nucleon momentum be larger than p_F. The nuclear potential is set at 27 MeV for carbon and oxygen and 32 MeV for iron.

NEUT simulates the interactions of mesons and nucleons within the nucleus. For pions, absorption, inelastic scattering, and charge exchange are considered. The Woods-Saxon nucleon density distribution [60] is used to set the position of the pion in the nucleus. The interaction mode of the pion is determined by calculating the mean free path of each interaction using the model by Salcedo *et al.* [61]. If charge exchange or inelastic scattering occurs, the momentum and direction of the pion are determined based on results from

πN scattering experiments [62]. The Pauli blocking effect is taken into account when calculating the pion scattering amplitude; the nucleon momentum after the scattering must be larger than the Fermi surface momentum evaluated at the interaction point. The interaction of K and η in the nucleus are also considered using basically the same method used for pions. For kaons, the differential cross sections and interaction kinematics are simulated based on the results of experimental measurements [63, 64, 65]. The absorption of η is also considered [66].

The simulation of pion nuclear effects is evaluated by comparison with data. Figure 4.6 shows the interaction cross sections for π^+ on oxygen as a function of pion momentum. The lines show the result of the MC simulation; the points are taken from experimental measurements [67].

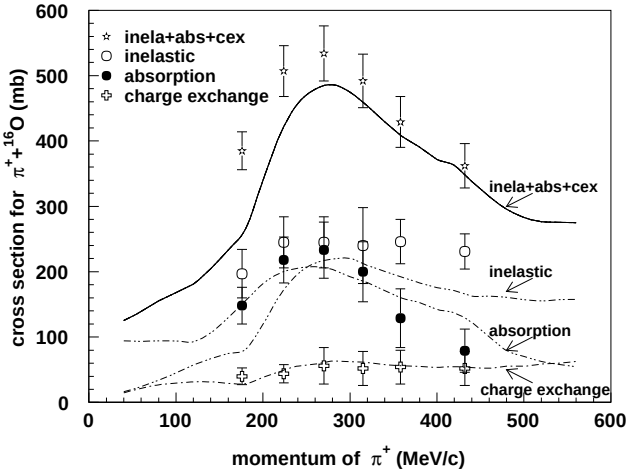

Figure 4.6: Calculated cross sections for π^+-^{16}O interactions compared to experimental measurements [67]. The data comes from measurements of π^+-^{12}C interactions; thus, the data points are scaled by a factor of 16/12 to be compared with the π^+-^{16}O calculation.

It is also possible for deltas to be absorbed by the nucleus. If a neutrino interaction excites a delta resonance, but the delta is absorbed, there is no pion in the final state. In our simulation, this occurs for 20% of the deltas produced.

Nucleon-nucleon interactions in the nucleus are also simulated; the differential cross sections are obtained from nucleon-nucleon scattering experiments [68]. Both elastic scattering and delta production [69] are considered.

4.3 Detector Simulation

GEANT3 is used to simulate the interactions of particles with the detector material.

4.3.1 Energy deposition

The energy loss of a particle in each single strip is simulated by GEANT. This energy loss must be adjusted to correctly simulate the scintillation light that is observed in the detector. For protons, the effect of scintillator quenching (described in Section 3.7) is simulated, using the measured value for Birk's constant in SciBar, 0.0208 $\pm$ 0.0023 cm/MeV. The attenuation of light in the WLS fiber is taken into account using the measured attenuation length for each channel, which is approximately 350 cm on average. For each hit, crosstalk among nearby channels is simulated. Chapter 5 will describe the crosstalk simulation in detail. After correcting for all these effects, the energy deposition in MeV is converted to number of photoelectrons (p.e.) using the light yield calibration constant which is measured for each channel with cosmic muons. The number of photoelectrons is then smeared by Poisson statistics. Finally, the PMT charge resolution of 40% is taken into account. To simulate the digitization of the signal, the energy deposition in p.e. is converted to ADC counts. Electronics noise and the reponse of the VA shaping are taken into account.

4.3.2 Timing

To simulate the timing response of our detector, the true time of energy deposition given by GEANT is corrected by adding the travel time of the light in the WLS fiber; the velocity of light in the fiber is approximately 16 cm/ns. In addition, the time is smeared by the timing resolution of the detector.

4.3.3 Interactions of pions in the detector

The CALOR program library [70] is used to simulate the interactions of pions with the detector material for pions with momentum greater than 0.5 GeV/c. For lower energy pions, the CALOR simulation does not reproduce the data well, so a custom library [54] is used.

Chapter 5

Study of SciBar Crosstalk Simulation

Crosstalk is the appearance of an apparent signal in channels other than the channel in which the original signal actually occurred. In the SciBar detector, crosstalk can occur in three ways: between the scintillating bars, in the electronics, and in the multi-anode photomultiplier tubes (MAPMTs). The light leakage between bars is expected to be negligible based on a laboratory test using cosmic muons [24]. The crosstalk in the electronics is also small. As for crosstalk within the MAPMTs, there are two main sources. Optical crosstalk is caused mainly by primary photoelectrons that are multiplied in the wrong channel. This gives some probability that a 1 photoelectron (p.e.) signal will be observed in a channel other than the channel that is exposed to the signal. Electrical crosstalk is caused by electrons leaking from one dynode chain to another near the bottom of the chain. This means that some small fraction of charge is always expected to leak into other channels. For both kinds of crosstalk, the average charge observed in the crosstalk channel is proportional to the average charge observed in the signal channel.[71]

The amount of crosstalk is typically expressed as the ratio of the charge observed in the crosstalk channel to the charge observed in the signal channel. For example, 4% crosstalk means that the charge observed in that particular channel is 4% of the charge observed in the channel where the signal is delivered.

Crosstalk can affect the event reconstruction in several ways. Crosstalk can add hits at the end of track, extending the track length, or crosstalk hits can create fake tracks. Crosstalk can affect the angular resolution. Crosstalk can also affect the measured dE/dx. Because crosstalk can have a significant

impact in the reconstruction, it is important for crosstalk to be well-simulated in the MC. A study of crosstalk simulation is performed to minimize the systematic uncertainty due to the crosstalk model.

5.1 Crosstalk Simulation

The crosstalk simulation in SciBar doesn't consider optical and electrical crosstalk separately, but considers only the mean effect, which is that the average charge observed in a crosstalk channel is proportional to the average charge observed in the signal channel. The constant of proportionality is a parameter in the model. The simulation takes the total charge of a simulated hit and spreads that charge out among the hit channel and the surrounding channels using the crosstalk parameter(s).

5.1.1 A Simple Model

One method to simulate crosstalk in an MAPMT is to consider only the charge spread to the nearest channels - the four neighboring channels (top, bottom, left and right) and the four diagonal channels. This is one method tested for the SciBar simulation. Figure 5.1 shows a signal channel and the eight surrounding channels before and after crosstalk. Let the total charge of the simulated hit be Q_0. Let the amount of charge remaining in the hit channel after crosstalk be Q. The parameters of this model are n and d, the proportion of the observed charge in the hit channel (Q) that is observed in the neighboring and diagonal channels, respectively. In other words, the amount of charge in a neighboring channel after crosstalk is $Q_{neighbor} = nQ$, and the amount of charge in a diagonal channel after crosstalk is $Q_{diagonal} = dQ$. Given that $4Q_{neighbor} + 4Q_{diagonal} + Q = Q_0$, the exact amount of charge in the hit channel and the eight surrounding channels after crosstalk can be found in terms of n, d, and Q_0 as follows:

$$\begin{aligned} Q &= \frac{Q_0}{(4n + 4d + 1)} \\ Q_{neighbor} = nQ &= \frac{nQ_0}{(4n + 4d + 1)} \\ Q_{diagonal} = dQ &= \frac{dQ_0}{(4n + 4d + 1)} \end{aligned} \tag{5.1}$$

When this model is used for crosstalk simulation, there is an excess of total number of hits in data as compared with the MC, as shown in Figure 5.2. In this figure, the crosstalk parameters are $n = 3.26\%$ and $d = 0.81\%$,

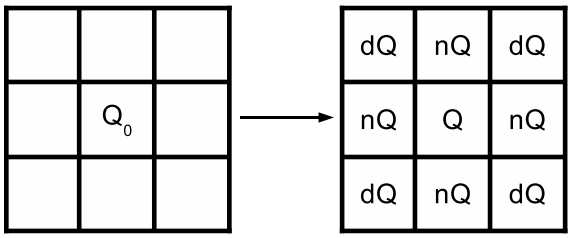

Figure 5.1: In a simple crosstalk model, if the center channel is hit with total charge Q_0, charge will spread to the eight immediately surrounding channels as shown in this figure. $Q = \frac{Q_0}{(4n+4d+1)}$

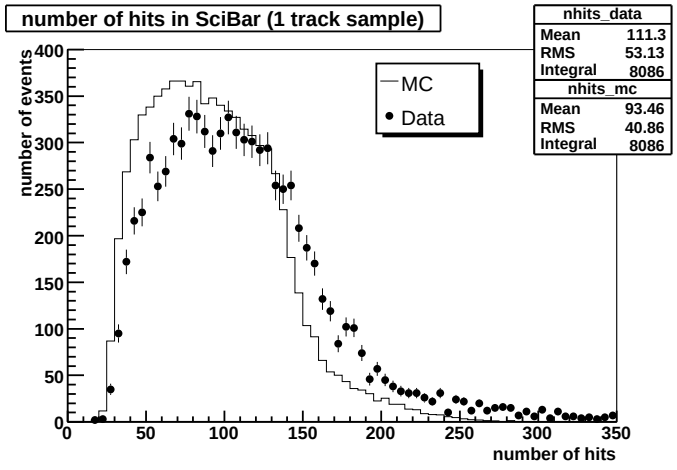

Figure 5.2: The distribution of total number of hits per event in the 1 track sample for MC compared with data.

which are close to the measured values of crosstalk in the MAPMTs [24].

One possible explanation for the excess of hits is that there is random noise in the data but not in the MC. This is unlikely to be a problem because a 2 p.e. threshold cut is applied to reduce noise hits. Another possible reason for the excess hits is a beam-induced background that we call skyshine, which is not simulated in the MC. Skyshine is a background we see in our data with timing that is slightly offset from the neutrino beam timing. The hits from skyshine are clustered in the upper part of the detector. We believe that neutrons and gamma-rays are produced by interactions in the beam dump. These particles then interact in the air above, producing neutral particles that travel downward into SciBar. The number of hits from skyshine interactions can be reduced by eliminating hits that occur in between bunches. However, the discrepancy in number of hits persists even after making this cut. Another possibility for the discrepancy is the crosstalk simulation.

A large discrepancy is also observed between data and MC in the distribution of average distance between off-track hits and the track, shown in Figure 5.3. In the data, hits are farther away from the track on average than

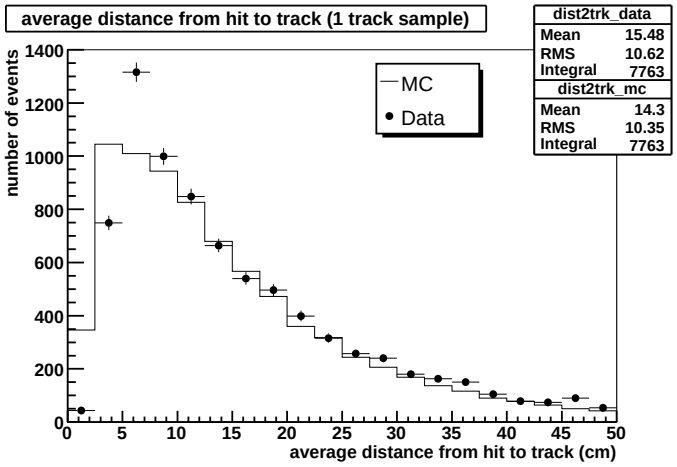

Figure 5.3: Comparison of data and in the distribution of average distance between off-track hits and the track in the 1 track sample

they are in MC. The discrepancy is especially spectacular in the first three bins, i.e. near the track. Each bar in SciBar is connected to an MAPMT channel based on position, as shown in Figure 5.4. Groups of x or y bars in an 8×8 array are mapped to the 8×8 array of pixels on a single MAPMT. Thus the greater distance between off-track hits and the track in the detector shown in Figure 5.3 maps back to a greater distance between off-track hits and track hits in the MAPMT. This is an indication that the crosstalk simulation might be the problem.

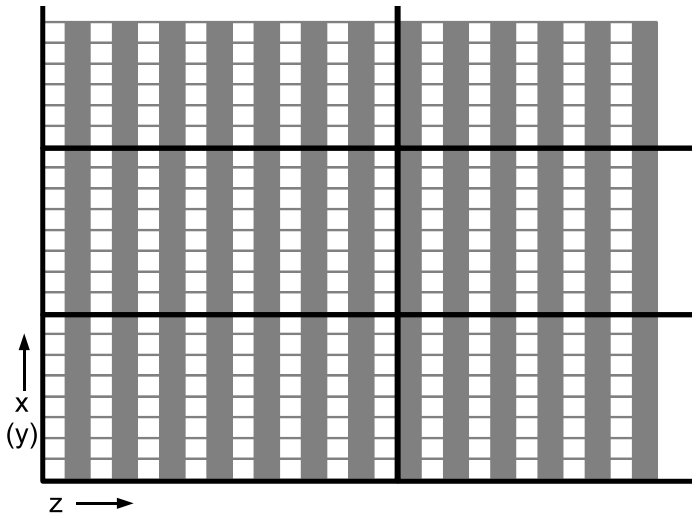

Figure 5.4: Diagram of the SciBar detector, x(or y)-z view. Each black box encloses 64 bars that are mapped to the same MAPMT.

5.1.2 An "Extended" Model

This discrepancy in the distance between hits and the track shown in Figure 5.3 hints that a different model from the simple eight-channel crosstalk should be considered. Suppose charge is spreading not just to the eight immediately surrounding channels in the MAPMT, but to the next layer of channels, 24 in all.

To model this with a minimum number of parameters, we assume that the charge due to crosstalk at a distance r from the hit is proportional to one over the square of the distance, $Q_{xtalk} \propto 1/r^2$. This assumption was based on the fact that the charge is diffusing across a two-dimensional surface. In this model, the ratio of the amount of crosstalk between channels is equivalent to the ratio of $1/r^2$ between channels, where r is the distance to the center of the hit channel. For example, the ratio of the amount of charge due to crosstalk in a diagonal channel to that in a neighboring channel is:

$$\frac{Q_{diagonal}}{Q_{neighbor}} = \frac{1/r^2_{diagonal}}{1/r^2_{neighbor}} \tag{5.2}$$

Assume the distance from the center of the hit channel to the center of a neighboring channel, $r_{neighbor}$, is a; the distance from the center of the hit channel to the center of a diagonal channel, $r_{diagonal}$, is thus $\sqrt{2}a$, and so on as shown in Figure 5.5. Using Equation 5.2 and these distances, we see that

√8a	√5a	2a	√5a	√8a
√5a	√2a	a	√2a	√5a
2a	a		a	2a
√5a	√2a	a	√2a	√5a
√8a	√5a	2a	√5a	√8a

Figure 5.5: The grid represents the surface of an MAPMT. Suppose the central channel in this diagram is the hit channel. The numbers in the diagram show the distance between each channel and the hit channel (measured center to center).

the ratio of crosstalk between a diagonal channel and a neighbor channel is

$$\frac{Q_{diagonal}}{Q_{neighbor}} = \frac{1/r^2_{diagonal}}{1/r^2_{neighbor}} = \frac{(1/(\sqrt{2}a))^2}{1/a^2} = \frac{1}{2} \tag{5.3}$$

If the amount of charge due to crosstalk in a neighboring channel is $Q_{neighbor} = nQ$, then according to this model, the amount of charge due to crosstalk in a diagonal channel is $Q_{diagonal} = \frac{Q_{neighbor}}{2} = \frac{nQ}{2}$.

For this extended crosstalk model, the only parameter is the amount of crosstalk in a neighboring channel (n). Given a MC hit with known charge Q_0, the amount of charge in all 25 channels (one hit channel and 24 surrounding channels) can be determined in terms of Q_0 and n using the relative $1/r^2$ between neighboring channels and other channels, as shown in Figure 5.6.

5.2 Crosstalk Correction

As part of the event reconstruction algorithm, a crosstalk correction is applied to both data and MC to reduce the number of crosstalk hits before tracking. A hit threshold of 2 p.e. is applied after the crosstalk correction but before tracking.

The crosstalk correction is applied in the following way: Number the channels of the MAPMT from 0-63. The matrix M is the 64 $\times$ 64 crosstalk

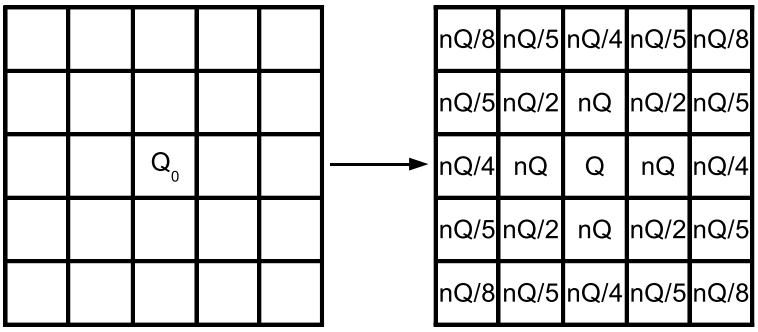

Figure 5.6: In the extended crosstalk model, if the center channel is hit with total charge Q_0, charge will spread to the 24 surrounding channels as shown in this figure. $Q = Q_0/(1 + 9.1n)$.

matrix, where element M_{ij} represents the fraction of channel j's signal that migrates to channel i due to crosstalk. If $\vec{q}$ is a 64-length vector where q_j is the charge in channel j before crosstalk and $\vec{q'}$ is a 64-length vector where q'_i is the charge in channel i after crosstalk, then:

$$q'_i = \sum_j M_{ij} q_j \tag{5.4}$$

For the crosstalk correction, we know $\vec{q'}$ and would like to know $\vec{q}$. So,

$$q_i = \sum_j M^{-1}_{ij} q'_j \tag{5.5}$$

5.3 Comparison of Different Crosstalk Models

To choose the crosstalk model that best matches the data, we tested the two models described in Sections 5.1.1 and 5.1.2 with several different parameters. See Table 5.1 for the full list of MC sets that were generated for this study.

Table 5.1: Crosstalk Models Tested

Simple Model (described in Section 5.1.1)
3.26%,0.81%
4%,1%
4%,2%
5%,1.25%
Extended Model (described in Section 5.1.2)
2.5%
2.75%
3%
3.25%
3.5%
3.75%
4%

To study crosstalk, a very pure sample of single muon events (from beam data) are selected. For each model listed in Table 5.1, a set of MC is produced that consists of ∼10,000 of these muon events; the data set contains ∼8,800 such events. For each MC set, the event reconstruction is done in data and MC using the same crosstalk model and parameters for the crosstalk correction as is used in the simulation; there is never a mismatch between models used for crosstalk simulation and correction.

For each event, only hits that share an MAPMT with a tracked hit are used. In other words, for each hit channel in an event, the channel is matched to its MAPMT, and if there is no muon signal in the same MAPMT, the hit is discarded. Clearly, if there is no muon signal in an MAPMT, there can be no crosstalk from the muon signal in that MAPMT. A timing cut is applied to eliminate off-bunch hits to reduce hits from noise, cosmic rays, or skyshine. Also, hits are required to be in coincidence (within 50 ns) with the muon track.

Using the hits in each event that pass the above cuts, four distributions are considered. The first distribution is the total number of these hits. The second distribution is the average 2D distance between off-track hits and the projection of the track in the x-z plane or y-z plane. The third plot is the average number of off-track hits (averaged over all events) vs distance to the track. For example, the point at 1.25 cm represents the average number of off-track hits found between 0 and 2.5 cm from the track. The final distribution is the charge of the off-track hits. This distribution is not an average or total; the charge of every off-track hit for every event is included. Each MC histogram is normalized to the data by total number of entries in the histogram.

The number of hits and average distance to track distributions are chosen for comparison since the discrepancy was first noticed in these distributions.

The charge distribution is chosen because crosstalk will obviously have a large effect on it. The number of hits versus distance to track plot is chosen because it is a good check on the crosstalk hypothesis. If the discrepancy in the number of hits is happening far away from the track, then crosstalk can't possibly be the problem.

Since the crosstalk correction is exactly the inverse of the crosstalk simulation, one might wonder if the MC distributions change at all from model to model. In fact, they do change, because after crosstalk simulation, but before the correction, other effects are simulated, such as PMT resolution.

5.4 Conclusion

To determine the best model using the four distributions, χ^2 between MC and data is computed for each distribution in the standard way. Figure 5.7 shows a plot of χ^2 per degree of freedom (d.o.f.) vs. the crosstalk parameter value for each distribution. Figure 5.8 shows the total χ^2 per d.o.f. vs. crosstalk parameter. (For the simple model, the crosstalk parameter for neighboring channels is used as the parameter on the horizontal axis; to distinguish between the n,d = 4%,1% and 4%,2% models, the points are plotted at 4% and 4.1%, respectively.)

Based on the plot of total χ^2 per degree of freedom shown in Figure 5.8, we conclude that the 3.25% extended model is the best model for SciBar's crosstalk. The χ^2 plot for number of hits does not show a clear minimum, but this is not surprising, as it is the only distribution of the four that includes on-track hits. Even excluding this distribution from the total χ^2, the minimum is still at 3.25%. Figure 5.9 shows the amount of crosstalk (%) in each channel using the extended model with 3.25% as the parameter. Figures 5.10 and 5.11 show the distribution of number of hits and average distance between hits and the track for the final model (to be compared with Figures 5.2 and 5.3).

The minimum of χ^2 for each distribution individually (excluding the number of hits distribution) is between 3% and 3.5%, and for all combinations of 2 or 3 of the distributions, the minimum χ^2 is always between 3% and 3.5%. Thus we assign a systematic uncertainty of 0.25%, and the result is 0.0325 ± 0.0025.

The measured crosstalk in the MAPMTs is around 3% and 1% for neighboring and diagonal channels, respectively [24]. The result of this crosstalk simulation study might seem not to agree well with the measurement, in particular the fact that crosstalk in diagonal channels in this model is 1.63% instead of 1%. However, there is not necessarily a problem. The model used in the simulation is very simplistic and will not reproduce the effect of crosstalk very precisely. In the model, the amount of crosstalk is the same for every hit for every event. However, in reality, crosstalk will vary for each channel, and even

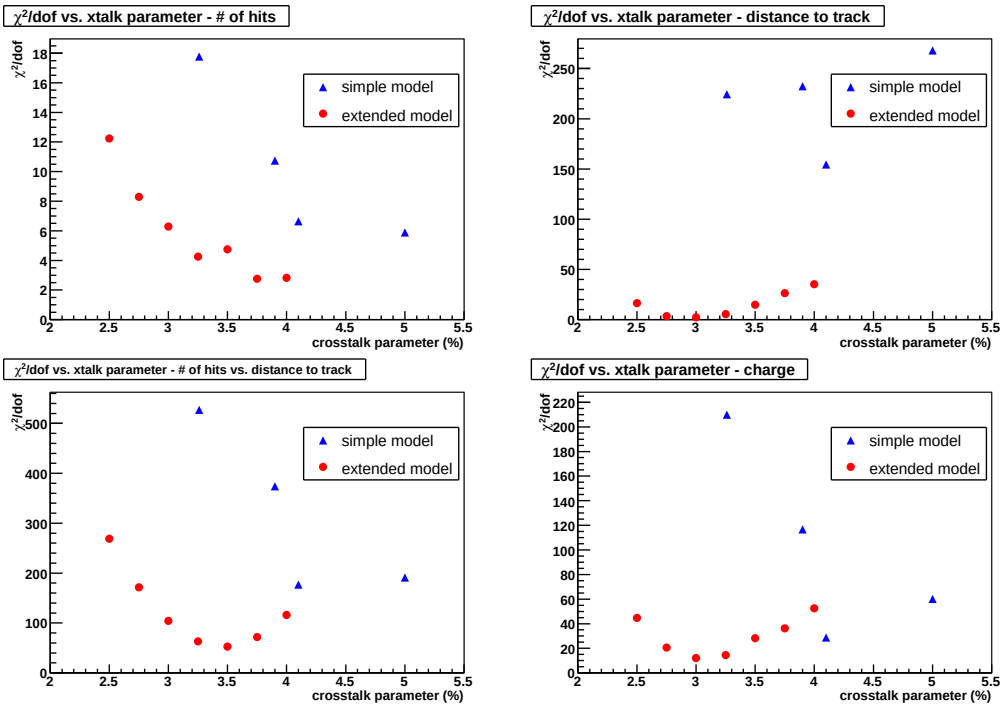

Figure 5.7: χ^2 per d.o.f. vs. crosstalk parameter for each distribution

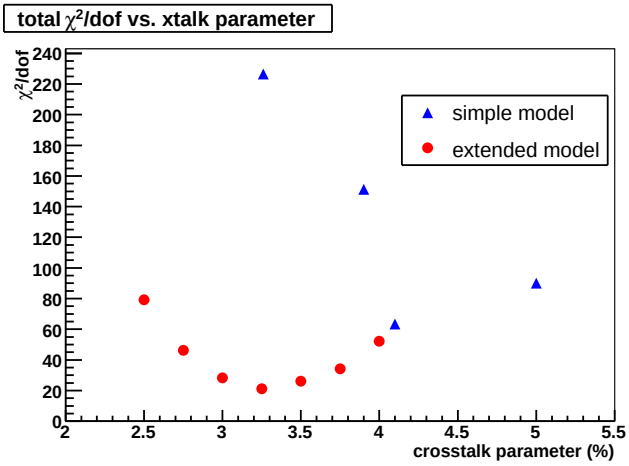

Figure 5.8: total χ^2 per d.o.f. vs. crosstalk parameter

0.41	0.65	0.81	0.65	0.41
0.65	1.63	3.25	1.63	0.65
0.81	3.25		3.25	0.81
0.65	1.63	3.25	1.63	0.65
0.41	0.65	0.81	0.65	0.41

Figure 5.9: Crosstalk in each channel (%) for the extended model with parameter $n = 3.25\%$

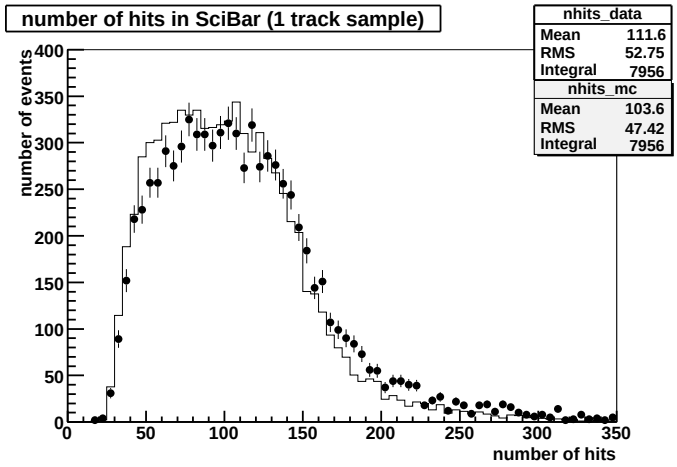

Figure 5.10: The distribution of total number of hits per event in the 1 track sample for MC compared with data using the best fit crosstalk model.

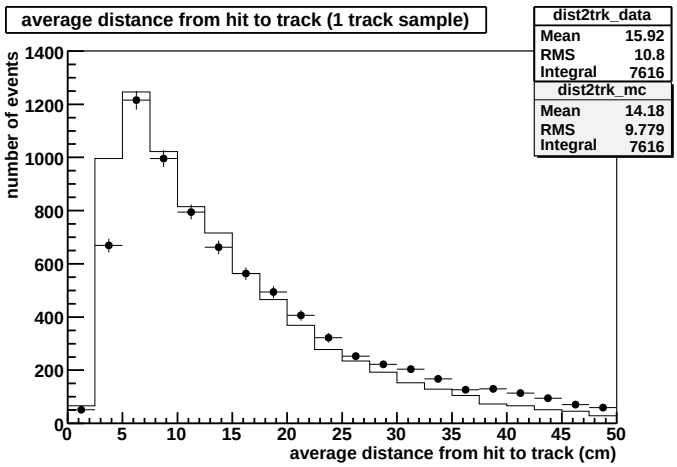

Figure 5.11: Comparison of data and in the distribution of average distance between off-track hits and the track in the 1 track sample using the best fit crosstalk model.

for a particular channel, crosstalk will vary from event to event. Furthermore, the possibly complicated effect of the reflection of signal hits at the corner or edge of an MAPMT is not considered in this model. In addition, we have assumed that the only important contribution to crosstalk in SciBar comes from the MAPMTs. Perhaps scintillator crosstalk, electronics crosstalk, or other effects are contributing more than originally thought. This model is an "effective crosstalk" model and is successful at reproducing what we see in the detector in real neutrino events.

Further details and plots from this study can be found in [72].

Chapter 6

Event Reconstruction in SciBar

To reconstruct events in SciBar, hits are selected and a tracking algorithm is applied. For a charged-current (CC) event candidate, the kinematic information of the reconstructed tracks is used to further classify the event. The SciBar detector also has particle identification capability. Data and MC events are reconstructed using exactly the same algorithm.

6.1 Hit Selection

A crosstalk correction is applied to reduce the number of hits due to crosstalk before tracking. The crosstalk model is discussed in detail in the previous chapter.

Figure 6.1 shows the distribution of number of photoelectrons (p.e.) per hit after the crosstalk correction for data and MC. There is an excess of hits in data with small energy deposit. Based on this distribution, a threshold cut of 2 p.e. is applied to reject these noise hits.

Figure 6.2 shows the timing distribution of beam triggered hits after the threshold cut. The bunch structure can be seen clearly. In between the bunches, a background that increases with time is observed. This is due to the beam-induced background called skyshine. The hits that occur with a time of 1200 ns or later are mostly due to cosmic rays.

6.2 Tracking

Since SciBar is arranged with alternating layers of horizontal (y) and vertical (x) bars along the beam direction (z), there are two two-dimensional

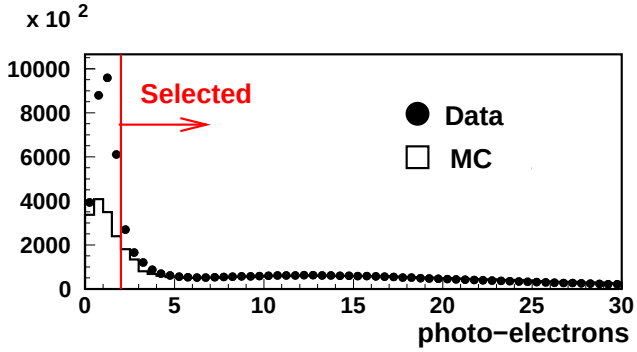

Figure 6.1: Distribution of number of p.e. per hit after crosstalk correction for data and MC. The distribution is normalized by the number of entries with >5 p.e.

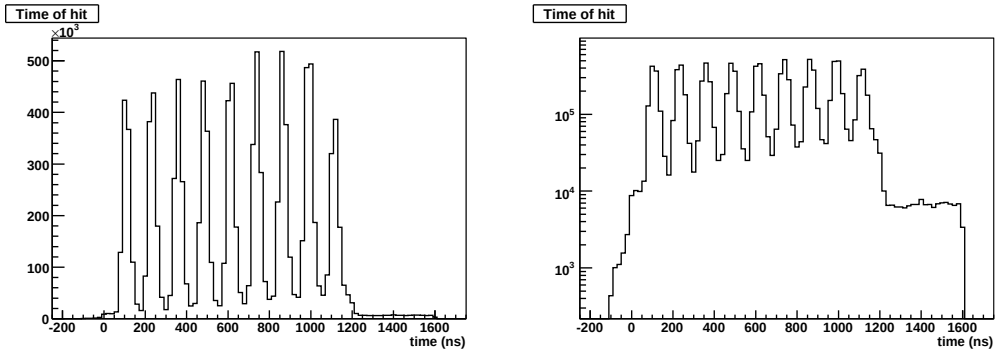

Figure 6.2: Timing distribution of beam triggered hits. The right figure shows the distribution in the log scale so that background in between the bunches can be seen more easily.

(2D) detector projections, x-z and y-z. A cellular automaton tracking algorithm [73, 74] is used to find tracks independently in each view. The tracks are fitted linearly using the least squares method. Then three-dimensional (3D) track reconstruction is performed by matching z-edges and timing of 2D tracks. Tracks are required to have hits in at least three consecutive layers, $\sim$8 cm in the beam direction. This corresponds to a momentum threshold of 450 MeV/c for protons and about 100 MeV/c for muons and pions. The reconstruction efficiency for single tracks with a length of at least 10 cm in the z-direction is 99%. The efficiency is lower when there are multiple tracks in the event due to overlapping of tracks in one or both views. The time of a track (t_{track}) is defined as the average time of all the hits associated with that track.

6.3 Event Selection for Analysis

6.3.1 CC Event Selection

The fiducial volume of SciBar is 2.6 m in both the x and y dimensions and 1.35 m in the z dimension (the 2^{nd} layer through the 53^{rd} layer of 64 total layers). This region was chosen as the fiducial volume to reject tracks from particles produced in the material surrounding the detector.

To select CC events, $\nu_\mu N \rightarrow \mu^- X$, we try to identify the muon produced in the interaction. First, for each event, we search for tracks that start in the fiducial volume of SciBar, where the starting point of the track is defined by the upstream track edge. Then we identify the events in which at least one of these tracks starting in the fiducial volume can be 3D matched to a track in the MRD (MRD3D) or matched to hits in the first layer of the MRD (MRD1L). For 3D matching, the MRD track is required to start in the first layer of the MRD and stop inside the MRD. The distance between the extrapolation of the SciBar track and the actual MRD track starting point must be less than 20 cm, and the angular difference of the tracks must be less than 0.5 radians in both projections. For 1L matching, the distance between the extrapolation of the SciBar track and the hits in the MRD must be less than 20 cm. This SciBar-MRD matched track is identified as the muon for the event. The MRD matching requirement imposes a muon momentum (p_μ) threshold of 450 MeV/c. The SciBar-MRD matched track is required to be within the spill time ($t_{track} < 1500$ ns after beam trigger). We verify that the SciBar-MRD track actually exits SciBar. If there is more than one track that meets the MRD matching criteria in an event, the longest such track is defined as the SciBar-MRD track.

The set of events in which a SciBar-MRD matched track is found is called the MRD sample, and this sample serves as our CC-enriched sample. Events

with any hit in the first layer of SciBar with at least 5 p.e. in coincidence with the SciBar-MRD track within 50 ns are excluded from the MRD sample to eliminate incoming particles produced by neutrino interactions in the other near detectors, the detector support structure, etc. According to MC simulation, 96% of the events in the MRD sample are true CC interactions.

The energy of the muon is reconstructed by the range of the SciBar-MRD track and expected energy deposit per unit length in SciBar, the Electron Catcher (EC), and the MRD. The reconstructed muon energy is calculated as follows:

$$\begin{aligned} E_\mu &= E_\mu^{SciBar} + E_\mu^{EC} + E_\mu^{MRD} \\ &= L_{SciBar}(\frac{dE}{dx})_{SciBar} + L_{EC}(\frac{dE}{dx})_{EC} + E_\mu^{MRD} \end{aligned} \tag{6.1}$$

E_μ^{SciBar}, E_μ^{EC}, and E_μ^{MRD} are the energy deposited in each detector. L_{SciBar} and L_{EC} are the muon's range through SciBar and the EC, respectively; $(\frac{dE}{dx})_{SciBar}$ is set to 2.10 MeV/cm, and $(\frac{dE}{dx})_{EC}$ is set to 11.25 MeV/cm. The resolution of muon momentum (p_μ) and muon angle with respect to the beam direction (θ_μ) are 90 MeV/c and 1.4 degrees, respectively, as estimated by the MC simulation. The systematic uncertainty in the muon momentum scale is estimated to be 2.7%, dominated by uncertainties of muon energy reconstruction in the MRD (see Section 2.2.5).

6.3.2 Matching Tracks to the Vertex

The upstream edge of the SciBar-MRD track is the reconstructed event vertex. Figure 6.3 shows the resolution of the event vertex for MC events in x, y, z, and $r = \sqrt{x^2 + y^2}$. To match tracks to the vertex, we search for tracks in the fiducial volume (other than the SciBar-MRD track) that have an edge that is less than 4.8 cm from the reconstructed event vertex and are in coincidence with the SciBar-MRD track within 100 ns. The 4.8 cm cut corresponds to 3σ in vertex resolution in the z dimension and more than 5σ in the x and y dimensions. Figure 6.4 shows the distribution of the total number of reconstructed tracks for events in the MRD sample without vertex matching. Figure 6.5 shows the distribution of number of tracks after vertex matching for events in the MRD sample. The MC is normalized to the data in both distributions by the number of events in the MRD sample.

As is evident in Figure 6.4, there is a significant discrepancy between data and MC in the number of tracks for events in the MRD sample. This discrepancy disappears when we apply the vertex matching criteria.

Figures 6.6 and 6.7 illustrate the vertex matching. Figure 6.6 shows a MC event in the MRD sample with four reconstructed tracks. Both the x-z

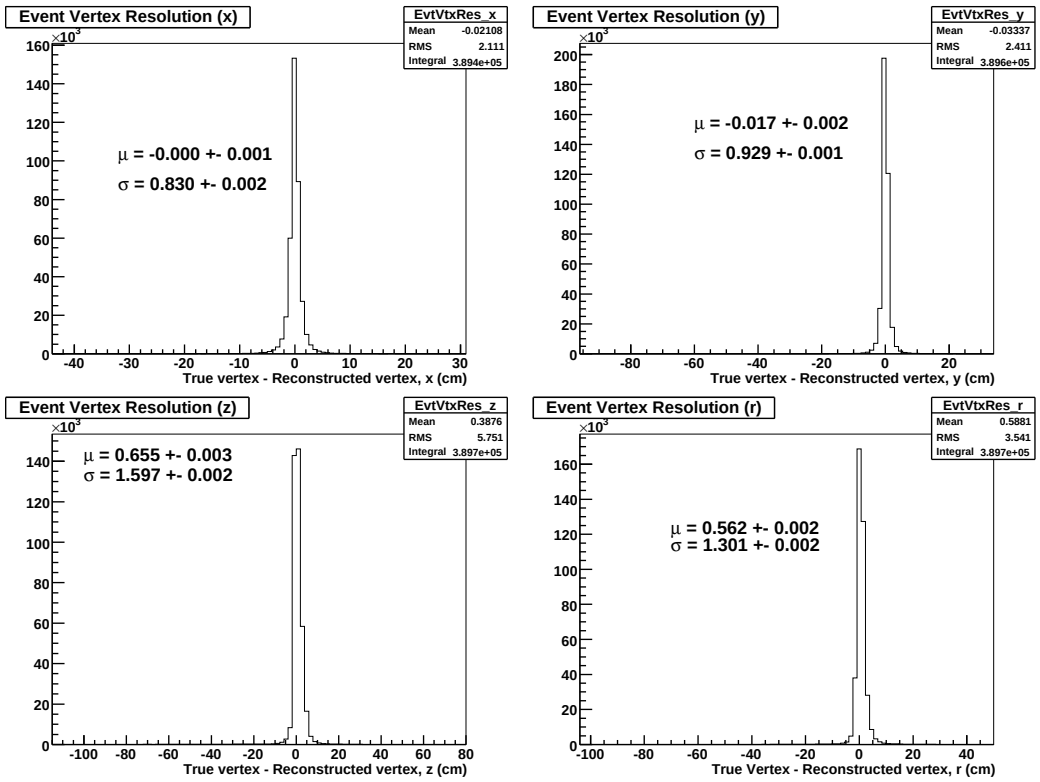

Figure 6.3: Event vertex resolution in x, y, z, and r

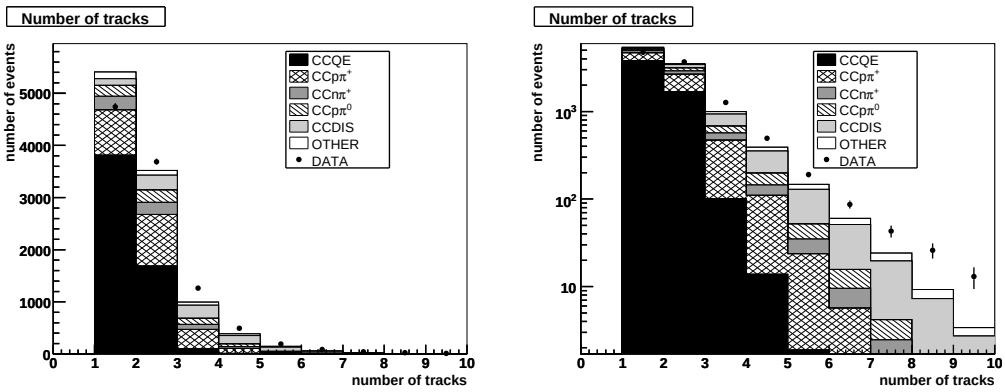

Figure 6.4: Number of tracks for events in the MRD sample. (Right: log scale)

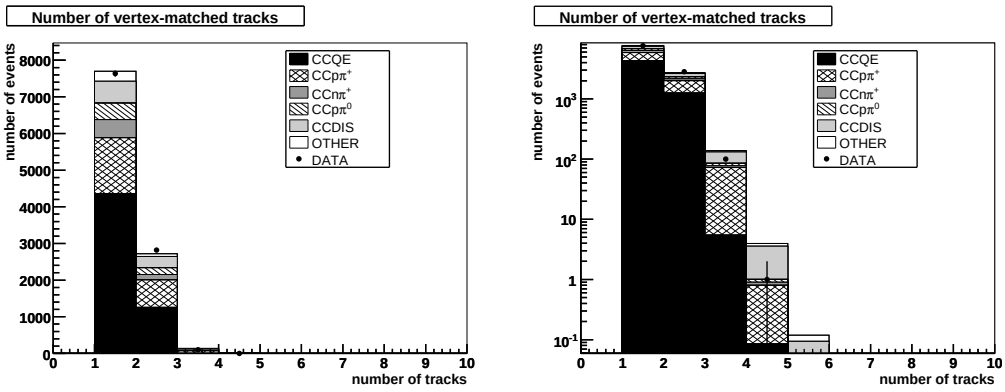

Figure 6.5: Number of vertex-matched tracks for events in the MRD sample. (Right: log scale)

and y-z views are shown. The SciBar-MRD matched track is in red. A 4.8 cm radius circle is drawn around the reconstructed vertex. The other three reconstructed tracks are not matched to the vertex. Therefore, after vertex matching, this event is considered a 1-track event. (This is an CC event in which a π^0 is produced; the tracks away from the vertex are from converted gamma-rays that were produced in the π^0 decay.) Figure 6.7 shows a MC event in the MRD sample with two reconstructed tracks. The second track is matched to the vertex; therefore, this event is considered a 2-track event.

6.3.3 QE-like and nonQE-like Separation

In the CCQE interaction, a neutrino strikes a target neutron, producing a muon and proton. The direction of the proton relative to the incident neutrino

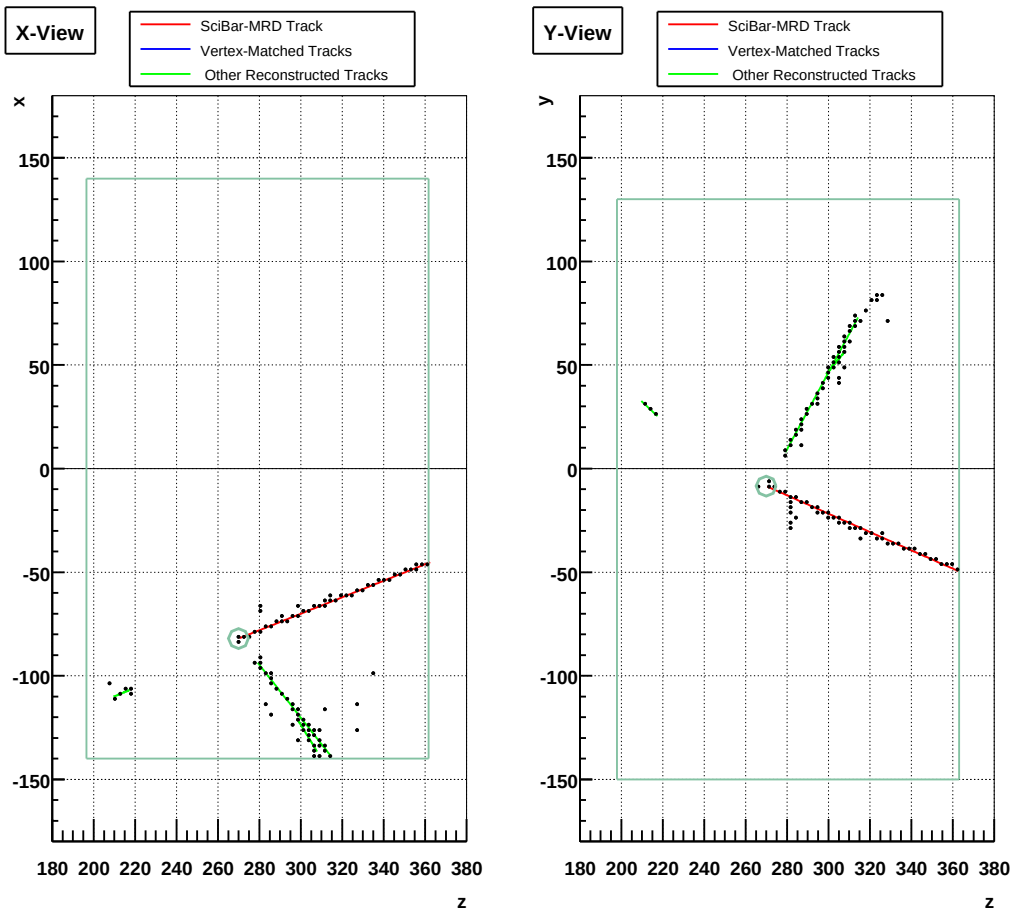

Figure 6.6: A MC event display, x-z (left) and y-z (right). There are four reconstructed tracks: the SciBar-MRD matched track and three others. A 4.8 cm radius circle is drawn around the reconstructed vertex. None of the three other tracks are matched to the vertex.

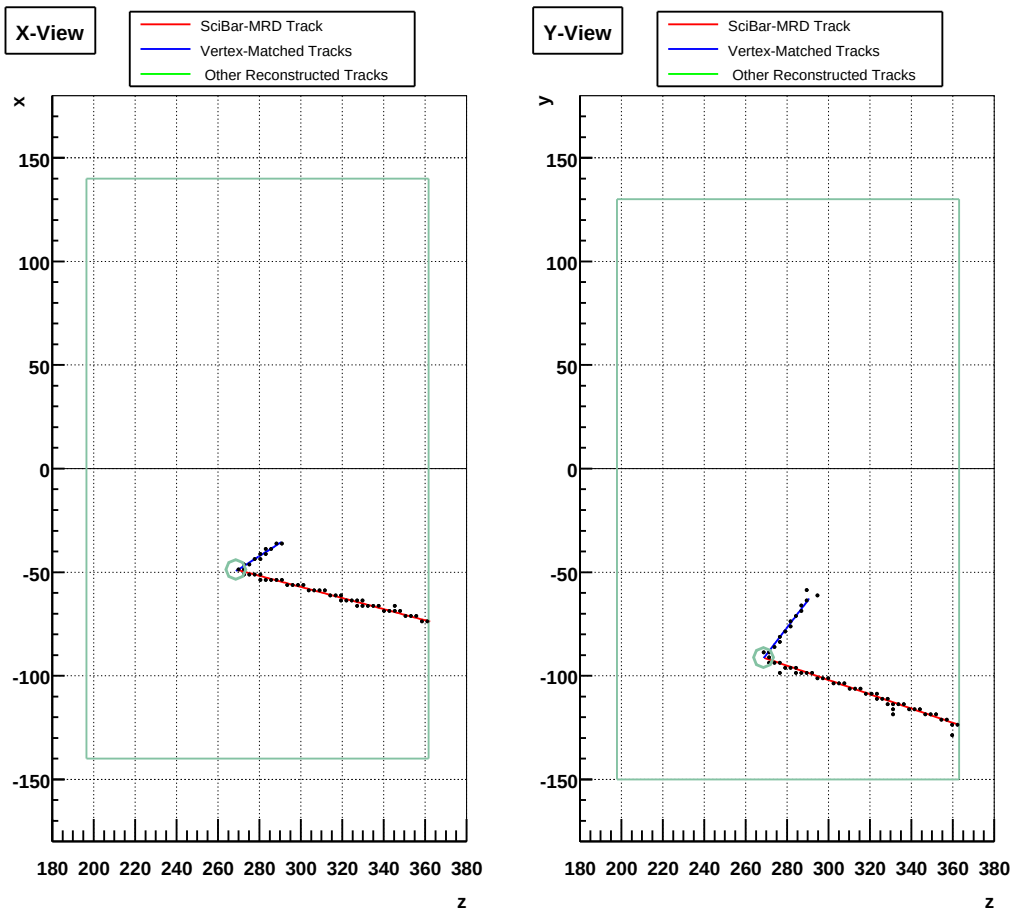

Figure 6.7: A MC event display, x-z (left) and y-z (right). There are two reconstructed tracks: the SciBar-MRD track and another track. A 4.8 cm radius circle is drawn around the reconstructed vertex. The second track is matched to the vertex.

direction can be calculated given the momentum and direction of the muon. For 2-track events, we define an angle called $\Delta\theta_p$ which is the angle between the expected proton track (assuming the event was CCQE) and the observed second track as shown in Figure 6.8. See Appendix A.1 for details of the calculation. Figure 6.9 shows the distribution of $\Delta\theta_p$ for the 2-track sample. The MC is normalized to data by the number of events in the MRD sample. We make a cut such that all the events with $\Delta\theta_p$ less than the cut are considered QE-like and other events are considered nonQE-like. To choose the cut value, we use the MC to examine the purity and efficiency of selecting CC1π^+ events in the nonQE sample as a function of the cut value. We want to simultaneously maximize both purity and efficiency. The purity^2 $\times$ efficiency, shown in Figure 6.10, has a maximum at 20 degrees, so we choose this as the cut value.

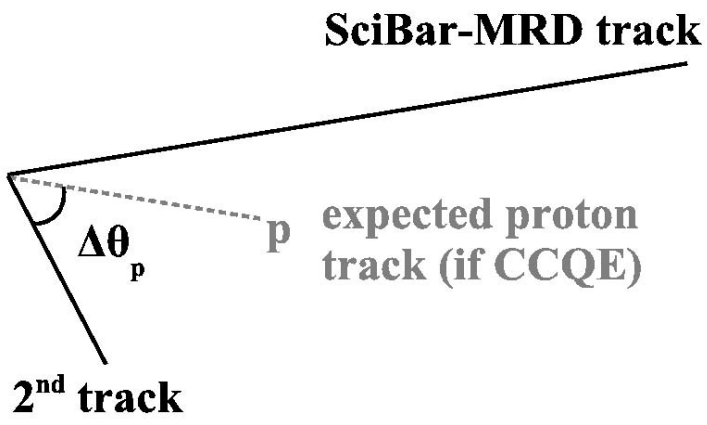

Figure 6.8: Definition of $\Delta\theta_p$

.

6.3.4 Particle ID for nonQE Sample

SciBar has the capability to distinguish protons from muons and pions using dE/dx. Figure 6.11 shows the dE/dx distribution for the SciBar-MRD track in the MRD sample and the second track in the 2-track QE sample; the former is a very pure sample of muons and the latter is a very pure ($\sim$ 90%) proton sample. The distributions are clearly separated.

We define a variable called the muon confidence level (MuCL) that is the probability that a particle is a muon (or other minimum ionizing particle) based on the energy deposition. We define the confidence level per plane, CL$_i$, as the fraction of events in the muon dE/dx distribution (obtained from cosmic muons) with larger dE/dx than what is observed in that plane, dE/dx_i.

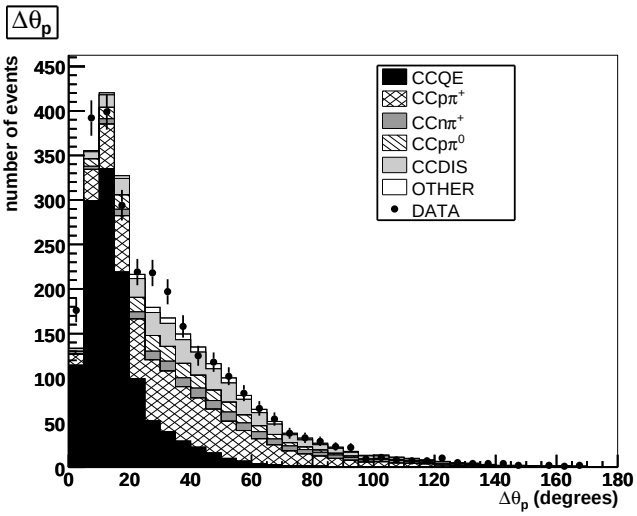

Figure 6.9: $\Delta\theta_p$, angle between expected proton track assuming CCQE and the observed second track for the 2-track sample

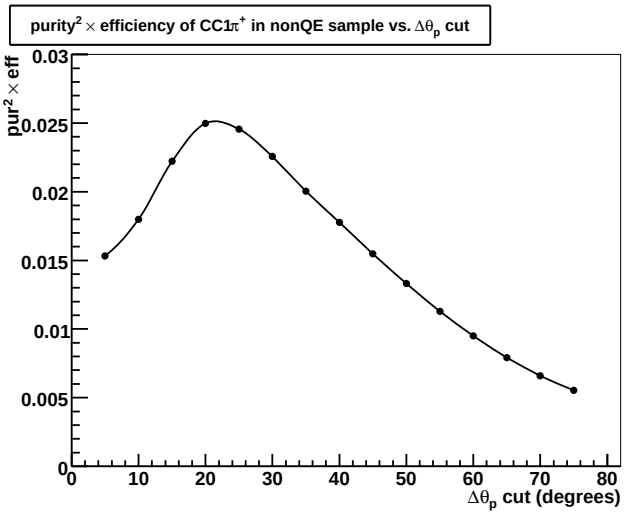

Figure 6.10: The purity^2 $\times$ efficiency of CC1π^+ events in the nonQE sample as a function of the cutoff value of $\Delta\theta_p$

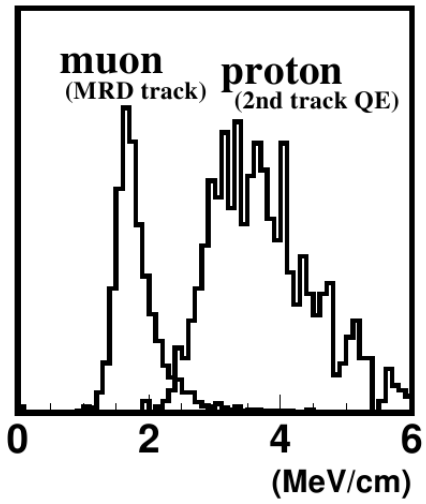

Figure 6.11: dE/dx for a very pure sample of muons and a very pure sample of protons.

Figure 6.12 shows the dE/dx distribution obtained with cosmic muons and the confidence level per plane as a function of the observed dE/dx in that plane.

To obtain the total confidence level, we assume the confidence level at the ith plane, CL_i, is an independent random variable with a uniform probability density function. We let CL be the random variable $\mathrm{CL} = \prod \mathrm{CL}_i$. Then the muon confidence level MuCL is the value of the cumulative distribution function for the random variable CL. More details can be found in [21]. An MuCL value of zero indicates a proton, and a value of one indicates a minimum ionizing particle.

The 2-track nonQE sample is further separated into a pion-like sample and a proton-like sample using the MuCL value of the second track. Figure 6.13 shows the distribution of MuCL for the second track in the 2-track nonQE sample. The MC is normalized to data by the number of events in the MRD sample. To choose the cut value, we use the MC to examine the purity and efficiency of classifying true pions in the nonQE pion sample as a function of the cut value. The purity^2 $\times$ efficiency, shown in Figure 6.14, has a maximum at 0.04, so we choose this as the cut value.

6.3.5 Comparison of data and MC

Table 6.1 shows the number of events in data and MC in the MRD sample. The MRD sample is broken down by number of tracks, and the 2-track sample is broken down further. MC is normalized to data by the number

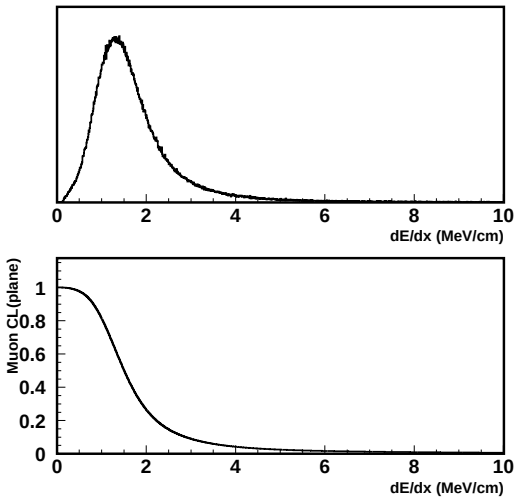

Figure 6.12: The dE/dx distribution for cosmic muons (upper) and the muon confidence level per plane as a function of the observed dE/dx in that plane (lower).

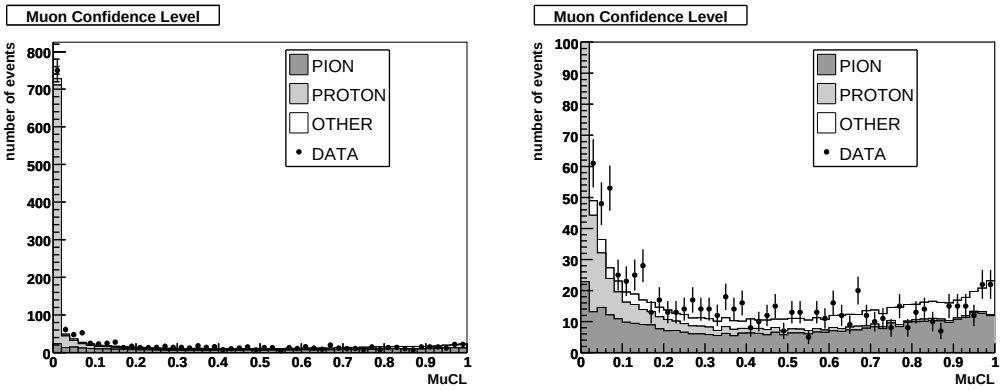

Figure 6.13: Muon confidence level for the second track in the 2-track nonQE sample. The plot on the right is a zoomed-in view.

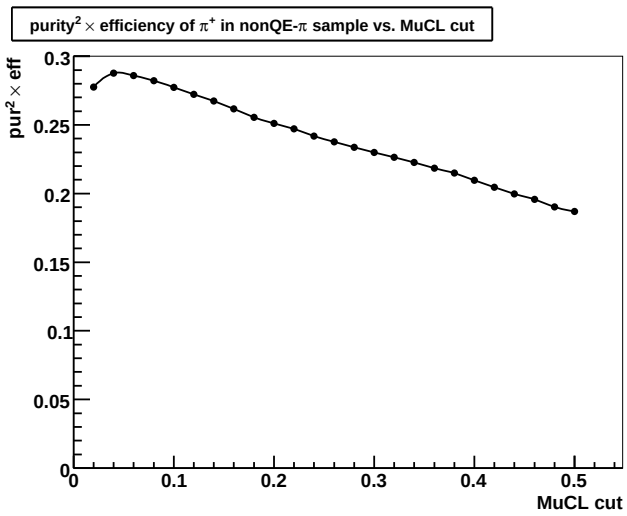

Figure 6.14: The purity^2 $\times$ efficiency of pions in the 2-track nonQE pion sample as a function of the cutoff value of MuCL

of events in the MRD sample. The samples in bold are the four samples used in this analysis.

Table 6.1: Event Samples

Sample	Data (# events)	MC (# events) (normalized)
MRD	10561 ± 103	10561 ± 17
1-track	7638 ± 87	7698 ± 14
2-track	2822 ± 53	2721 ± 8.5
2-track QE	1261 ± 36	1237 ± 5.8
2-track nonQE pion	750 ± 27	707 ± 4.3
2-track nonQE proton	811 ± 28	777 ± 4.5
3-track	100 ± 10	138 ± 1.9
4+-track	1.0 ± 1.0	4.1 ± 0.3

Chapter 7

Charged-Current Single Charged Pion Production

7.1 Introduction

Single pion production occurs by the excitation of a baryon resonance by neutrino interaction with a nucleon, followed by the prompt decay of the resonance into a nucleon-pion final state, $\nu N \to \ell N^*, N^* \to N'\pi$. (A single pion can also be produced by deep inelastic scattering or a coherent interaction. However, in this dissertation, 'single pion production' refers only to the resonance process.)

There are six channels of single pion production in CC interactions and eight in NC interactions of neutrinos and anti-neutrinos. Table 7.1 lists all 14 channels.

Table 7.1: Modes of Single Pion Production

Charged-current	Neutral-current
$\nu_\ell p \to \ell^- p\pi^+$	$\nu_\ell p \to \nu_\ell p\pi^0$
$\nu_\ell n \to \ell^- n\pi^+$	$\nu_\ell p \to \nu_\ell n\pi^+$
$\nu_\ell n \to \ell^- p\pi^0$	$\nu_\ell n \to \nu_\ell n\pi^0$
	$\nu_\ell n \to \nu_\ell p\pi^-$
$\overline{\nu}_\ell p \to \ell^+ p\pi^-$	$\overline{\nu}_\ell p \to \overline{\nu}_\ell p\pi^0$
$\overline{\nu}_\ell p \to \ell^+ n\pi^0$	$\overline{\nu}_\ell p \to \overline{\nu}_\ell n\pi^+$
$\overline{\nu}_\ell n \to \ell^+ n\pi^-$	$\overline{\nu}_\ell n \to \overline{\nu}_\ell n\pi^0$
	$\overline{\nu}_\ell n \to \overline{\nu}_\ell p\pi^-$

The three channels for CC muon neutrino interactions are:

1) $\nu_\mu p \to \mu^- p\pi^+$ (CC$p\pi^+$)

2) $\nu_\mu n \to \mu^- n\pi^+$ (CC$n\pi^+$)

3) $\nu_\mu n \to \mu^- p\pi^0$ (CC$p\pi^0$)

CC single pion production is the largest contribution to the total neutrino cross section after CCQE in K2K's energy region. In this dissertation, I present the measurement of the cross section for channels **1)** and **2)** above, collectively called CC1π^+.

CC single charged pion production was studied in a number of experiments, including bubble chamber experiments at Argonne [49], CERN [75, 50], Brookhaven [48], and Fermilab [76] beginning in the 1960s through the 1980s. However, the CC1π^+ cross section is still not well-known in the neutrino energy region near 1 GeV, which is the energy region of interest for many neutrino oscillation experiments. Neutrino detectors in oscillation experiments often use carbon or oxygen as target material. Therefore, it is important for cross section measurements to be made using a variety of nuclear targets so that the effect of the nuclear medium can be understood. Thus a measurement of the CC1π^+ cross section made at K2K's neutrino beam energy (average E_ν $\sim$1.3 GeV) with a carbon target is a significant contribution to the current knowledge.

7.2 Basic Distributions

Figure 7.1 shows the distribution of π^+ momentum and angle with respect to the beam direction for CC1π^+ interactions according to MC simulation. Figure 7.2 shows the distribution of the incident neutrino energy (E_ν) and the square of the lepton momentum transfer (Q^2) for CC1π^+ events in the MC.

7.3 Event Displays

Figure 7.3 shows the true particle tracks overlaid with the reconstructed hits for a MC CC$p\pi^+$ event in SciBar. Figure 7.4 shows the same for a CC$n\pi^+$ event.

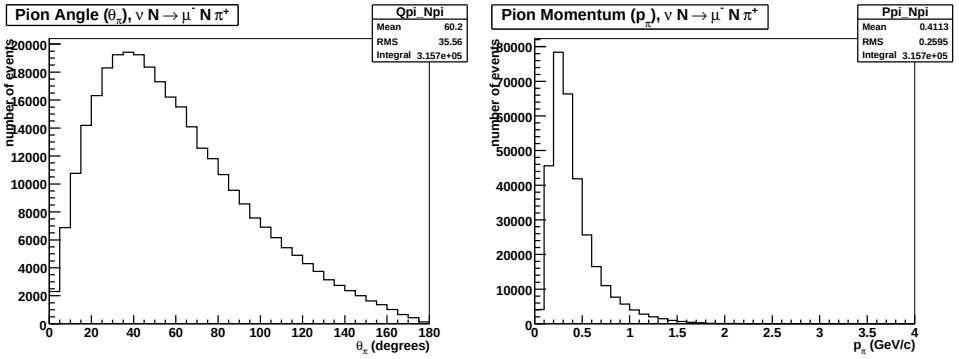

Figure 7.1: Pion momentum and angle distributions for CC1π^+ events.

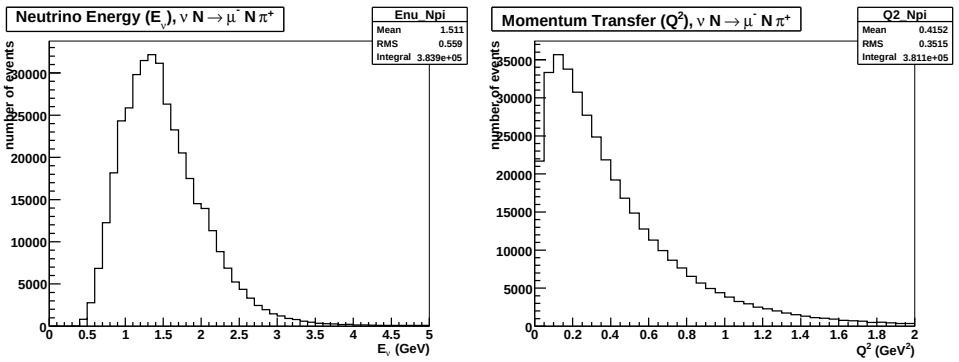

Figure 7.2: E_ν and Q^2 distributions for CC1π^+ events.

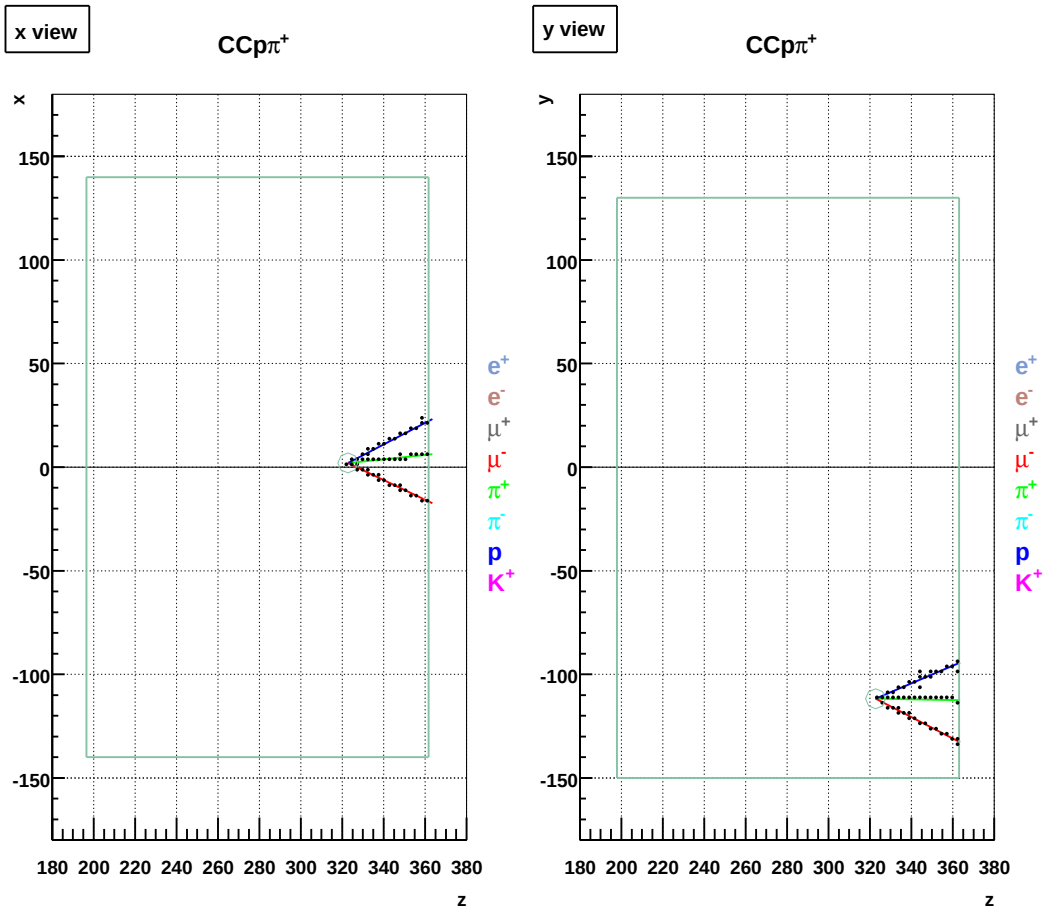

Figure 7.3: The true particle tracks overlaid with the reconstructed hits for a MC CC$p\pi^+$ event in SciBar. x-z (left), y-z (right).

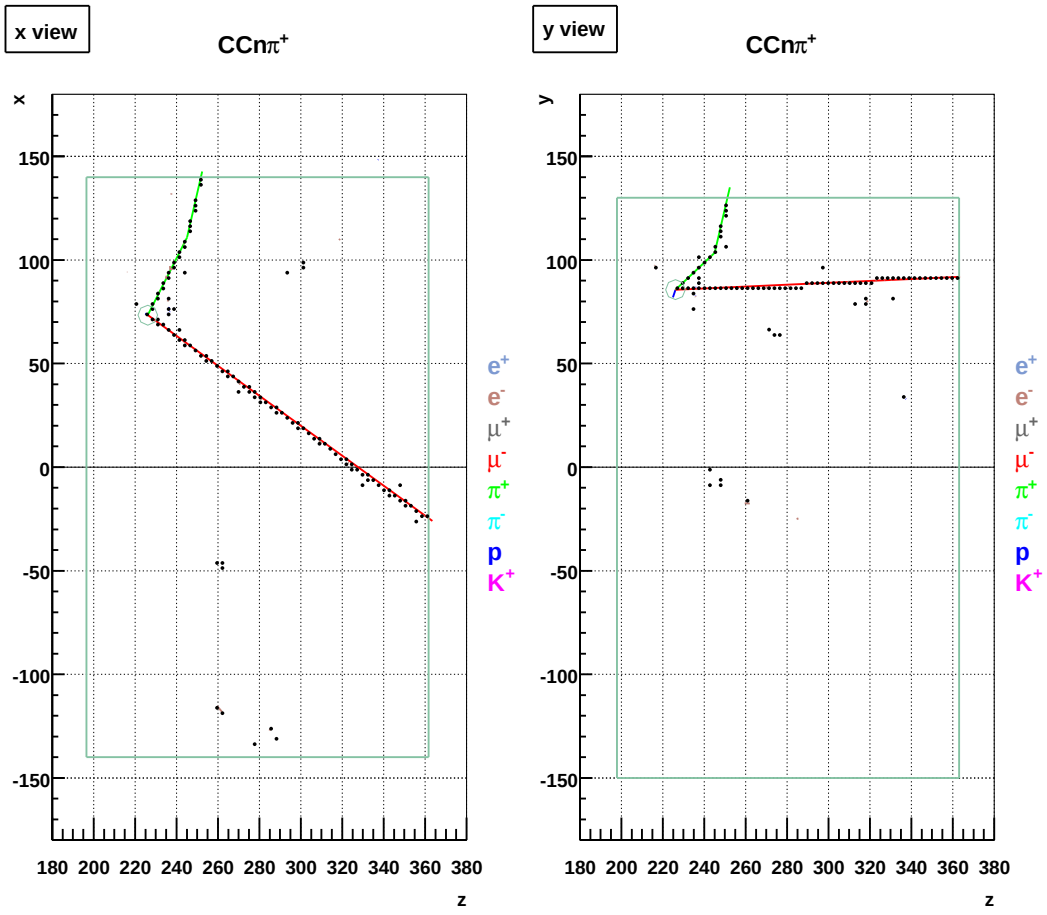

Figure 7.4: The true particle tracks overlaid with the reconstructed hits for a MC CC$n\pi^+$ event in SciBar. x-z (left), y-z (right).

Chapter 8

Cross Section Measurement

8.1 Analysis

8.1.1 Analysis Overview

Ideally, we would like to make a measurement of the absolute CC1π^+ cross section. To do this one needs a measurement of the absolute neutrino flux. Unfortunately, the measurement of K2K's absolute flux has large uncertainties due to difficulties in the estimation of the primary proton beam intensity, the proton targeting efficiency, and hadron production cross sections. Therefore, we measure the CC1π^+ cross section relative to the cross section for the CCQE interaction, $\nu_\mu n \to \mu^- p$, the dominant CC interaction in this neutrino energy range.

In this analysis, we bin the data and perform a maximum likelihood fit based on Poisson statistics to determine the cross sections of CC1π^+ and CCQE relative to the simulated cross sections. From the MC prediction and results of the fit, the observed CC1π^+ to CCQE cross section ratio can be extracted. We measure both the total cross section ratio for K2K's entire neutrino energy range and the energy-dependent cross section ratio.

8.1.2 Review of Events Selected for Analysis

We consider data and MC in the MRD 1- and 2-track sample (MRD1&2). This sample is sub-divided into four sub-samples (1-track, 2-track QE, 2-track nonQE pion, and 2-track nonQE proton) as described in Section 6.3. Table 8.1 shows the breakdown of all the events in the fiducial volume and each sub-sample by event type as predicted by the nominal MC.

Table 8.1: Breakdown of Samples by Event Type (numbers given are % of events in sample)

Sample	CCQE	CC$p\pi^+$	CC$n\pi^+$	CC$1\pi^0$	CC DIS	Other
Fiducial Volume	32	18	6	5	9	30
MRD	52	22	6	6	9	5
1-track	57	20	6	6	8	3
2-track QE	78	13	1	3	4	1
2-track nonQE pion	6	41	15	8	24	6
2-track nonQE proton	32	38	3	12	12	3

Shown in Table 8.2 is the fate of the π^+ for CC$1\pi^+$ events in each sample according to MC simulation. The first column shows the percent of CC$1\pi^+$ events in each sample in which a Δ-resonance is produced and absorbed in the nucleus (meaning there is no π^+ in the final state). The second column shows the percent of CC$1\pi^+$ events in which the π^+ is absorbed in the nucleus. The third column shows the proportion of events in which the π^+ undergoes charge exchange inside the nucleus. If charge exchange ($\pi^+ n \rightarrow \pi^0 p$) occurs, a π^0 exits the nucleus. It's also possible for double charge exchange ($\pi^+ n \rightarrow \pi^0 p$, followed by $\pi^0 n \rightarrow \pi^- p$) to occur; in that case, a π^- can exit the nucleus. If there is no absorption or charge exchange, the π^+ should exit the nucleus and deposit energy in the detector. For example, the first row of Table 8.2 indicates that the Δ is absorbed in 22% of CC$1\pi^+$ events in the 1-track sample, the π^+ is absorbed in 20% of CC$1\pi^+$ events in the 1-track sample, and charge exchange occurs in 4% of CC$1\pi^+$ events in the 1-track sample. In the remaining CC$1\pi^+$ events in the 1-track sample (54%), the π^+ escapes the nucleus. As expected, the CC$1\pi^+$ events in 2-track nonQE pion sample almost always have a π^+ in the final state.

Table 8.2: Final state for CC$1\pi^+$ events in each sample

Sample	Δ absorbed (% CC$1\pi^+$ events)	π^+ absorbed (% CC$1\pi^+$ events)	π^+ charge exchange (% CC$1\pi^+$ events)
1 track	22	20	4
2 track QE	19	16	3
2 track nonQE pion	4	4	2
2 track nonQE proton	24	22	4

In this analysis, the MC events in the four samples are further divided based on the interaction type and true neutrino energy. The interaction types considered are CCQE, CC$1\pi^+$, and background. The background consists mainly of CC deep inelastic scattering (CCDIS) and CC$p\pi^0$ interactions. The bins of true neutrino energy are defined as shown in Table 8.3.

The most basic kinematic information for the CC sample is the

Table 8.3: E_ν bins

E_ν Range (GeV)
0.00-1.35
1.35-1.72
1.72-2.22
> 2.22

reconstructed muon's momentum (p_μ) and angle with respect to the beam direction (θ_μ); any other kinematic quantities such as neutrino energy or momentum transfer (q^2) are reconstructed using p_μ and θ_μ. Data and MC are binned in p_μ bins of size 0.2 GeV/c and θ_μ bins of size 10 degrees. The p_μ vs. θ_μ distributions for each of the four event samples are used to fit MC to data. Figure 8.1 shows the comparison of data and MC of the p_μ and θ_μ distributions for each sample. The two-dimensional p_μ vs. θ_μ distributions for data and the nominal MC are shown in Appendix B. The two-dimensional p_μ vs. θ_μ distributions for all MC CC1π^+, CCQE, and background interactions are also shown in Appendix B.

8.1.3 Poisson Maximum Likelihood

For N bins where n_i is the number of observed events in bin i and $\mu_i(\vec{\theta})$ is the number of expected events in bin i which depends on parameters $\vec{\theta} = \langle \theta_1, \theta_2, ... \rangle$, the likelihood ratio, $\lambda(\vec{\theta})$ is

$$\lambda(\vec{\theta}) = \frac{f(\vec{n}, \vec{\mu}(\vec{\theta}))}{f(\vec{n}, \vec{n})} \tag{8.1}$$

where $f(\vec{n}, \vec{\mu}(\vec{\theta})) = \prod_i^N P(n_i, \mu_i(\vec{\theta}))$ and $f(\vec{n}, \vec{n}) = \prod_i^N P(n_i, n_i)$.
$P(n_i, \mu_i)$ ($P(n_i, n_i)$) is the Poisson probability of observing n_i events when μ_i (n_i) are expected, i.e.

$$P(n_i, \mu_i) = \frac{\mu_i^{n_i} e^{-\mu_i}}{n_i!} \tag{8.2}$$

Maximizing λ is equivalent to minimizing the quantity $-2 \ln \lambda$ [6], so $F_{poisson}$ is defined as

$$\begin{aligned} F_{poisson} &= -2 \ln \lambda \\ &= 2 \sum_i \left[\mu_i(\vec{\theta}) - n_i + n_i \ln \frac{n_i}{\mu_i(\vec{\theta})} \right] \end{aligned} \tag{8.3}$$

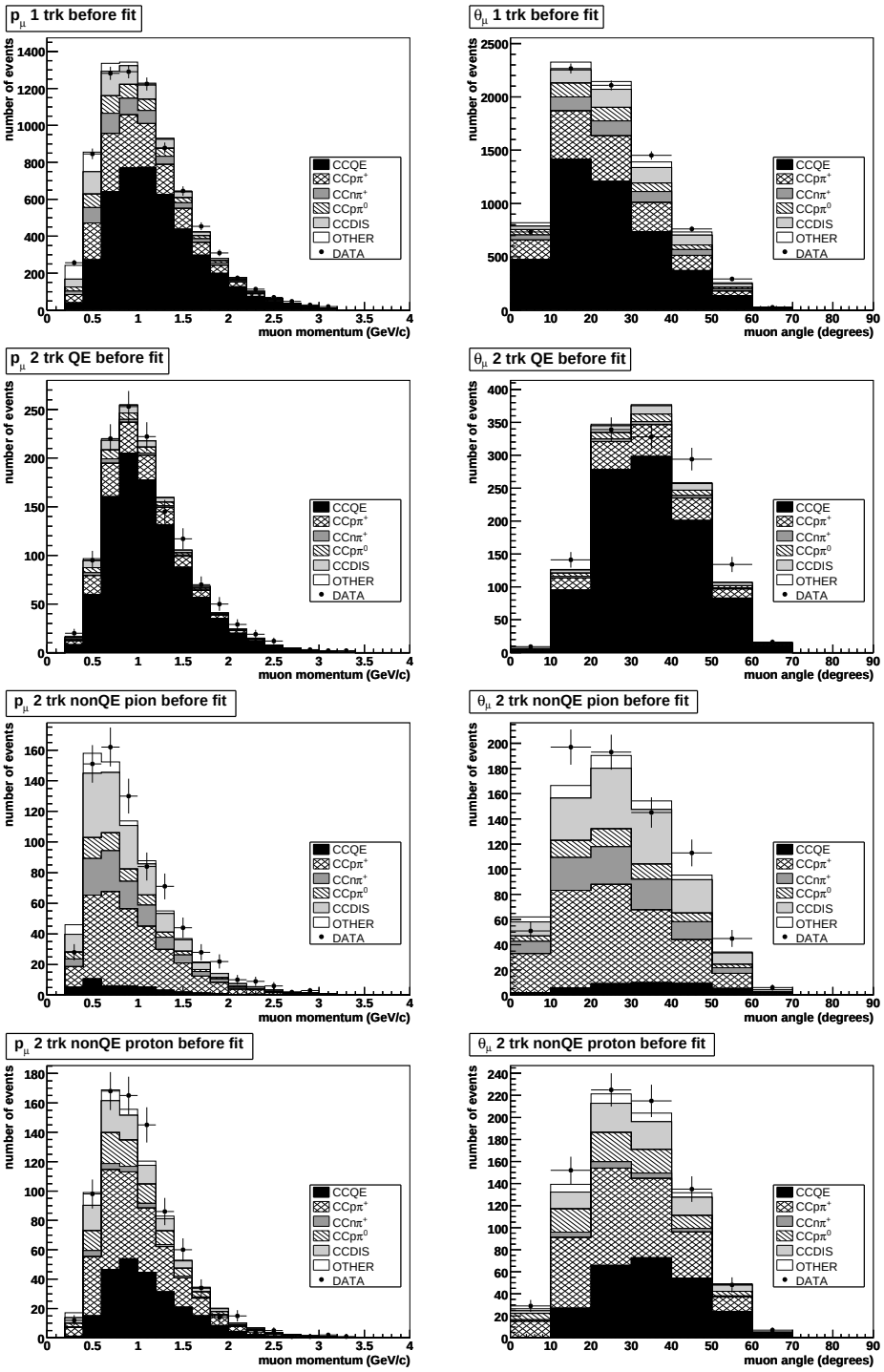

Figure 8.1: p_μ (left) and θ_μ (right) distributions for the data and nominal MC for the 1-track, 2-track QE, 2-track nonQE pion, and 2-track nonQE proton samples.

The expression inside the sum is valid only when n_i and μ_i are greater than zero. Since n_i and μ_i represent numbers of events, they should never be negative. For the special cases in which n_i or μ_i is zero, Equation 8.3 can't be used. If $n_i = 0$ and $\mu_i \geq 0$, the i^{th} term in $F_{poisson}$ is:

$$F^i_{poisson} = 2\mu_i \tag{8.4}$$

If $\mu_i = 0$ and $n_i > 0$, the i^{th} term in $F_{poisson}$ is:

$$F^i_{poisson} = \text{undefined} \tag{8.5}$$

So one must be careful not to allow bins in which μ_i might approach zero in the fitting. See Appendix A.2 for details.

8.1.4 Application of Poisson Maximum Likelihood

The function used in minimization (taken directly from Equation 8.3) is:

$$F_{poisson} = 2\sum_{is}\left[N^{exp}_{is} - N^{obs}_{is} + N^{obs}_{is}\ln\frac{N^{obs}_{is}}{N^{exp}_{is}}\right] \tag{8.6}$$

where N^{exp}_{is} and N^{obs}_{is} are the number of expected events and observed events, respectively, in bin i of the p_μ vs. θ_μ distribution of sample s. N^{exp}_{is} depends on the fitting parameters as shown below in Equation 8.7.

$$N^{exp}_{is} = \alpha\sum_e\left(R^{CCQE}N^{CCQE}_{ise}(P_{sc}) + R^{CC1\pi+}_e N^{CC1\pi+}_{ise}(P_{sc}) + N^{Bkgd}_{ise}(P_{sc})\right) \tag{8.7}$$

P_{sc} is the momentum rescaling parameter, $p'_\mu = p_\mu/P_{sc}$. The first step in each iteration of the minimization is stretching or shrinking the p_μ vs. θ_μ distributions for the nominal MC along the p_μ axis according to P_{sc}. Then, in Equation 8.7, $N^{CC1\pi^+}_{ise}(P_{sc})$ is the number of CC1π^+ events with true neutrino energy in bin e in bin i for sample s after scaling by P_{sc}. $N^{CCQE}_{ise}(P_{sc})$ and $N^{Bkgd}_{ise}(P_{sc})$ are defined similarly.

R^{CCQE} and $R^{CC1\pi^+}_e$ are scaling factors for the CCQE and CC1π^+ interactions, respectively. The scaling for CC1π^+ is energy-dependent; there is a different parameter for each neutrino energy bin e. However, only an overall scaling for the CCQE interaction is used, fixing the energy-dependency of the CCQE cross section to the MC prediction. The reason for fixing the shape of the CCQE cross section is that the shape has already been studied in K2K [19], and we consider uncertainties in the shape as a source of systematic uncertainty.

Since the MRD1&2 sample is a very pure CC sample, it can be used to normalize MC to data. Therefore, we want to force the total number of events in the MC to be the same as the total number of data events in the fit. This is accomplished by the overall normalization factor, α. We want to enforce the condition

$$\sum_{is} N_{is}^{exp} \equiv \sum_{is} N_{is}^{obs} \tag{8.8}$$

This implies that α is a function of the fitting parameters.

$$\sum_{is} N_{is}^{exp} = \sum_{is} N_{is}^{obs}$$

$$\sum_{is} \alpha \sum_{e} (R^{CCQE} N_{ise}^{CCQE}(P_{sc}) + R_e^{CC1\pi+} N_{ise}^{CC1\pi+}(P_{sc}) + N_{ise}^{Bkgd}(P_{sc})) = \sum_{is} N_{is}^{obs}$$

$$\Longrightarrow$$

$$\alpha = \frac{\sum_{is} N_{is}^{obs}}{\sum_{is} \sum_{e} \left(R^{CCQE} N_{ise}^{CCQE}(P_{sc}) + R_e^{CC1\pi+} N_{ise}^{CC1\pi+}(P_{sc}) + N_{ise}^{Bkgd}(P_{sc}) \right)} \tag{8.9}$$

So for every iteration of the fit, α is calculated using the nominal MC and the current fitting parameters.

Note that if we fix the total number of events in this way, then only two of the three cross sections can be free. That is, if we fix the total number of events, but let the number of CCQE and CC1π^+ events vary freely, then the number of background events will not be fixed, but will vary as:

$$N^{Bkgd} = N_{total} - N^{CCQE} - N^{CC1\pi+} \tag{8.10}$$

A p_μ vs. θ_μ bin is excluded from the fit if the number of normalized nominal MC events in the bin is less than 3. This corresponds to approximately 100 events of unnormalized MC, giving a statistical uncertainty of $\sim$10%. As shown in Section 8.1.3, the fitting function becomes undefined if the number of expected events is zero. Discarding bins with low MC statistics helps to prevent the fitting function from wandering into the undefined region. The bins are selected using this criteria before the fit. Figure 8.2 illustrates which bins in the p_μ vs. θ_μ distribution for each sample are used in the fit.

The systematic uncertainty in P_{sc} is estimated to be $\sigma_{P_{sc}} = 2.7\%$ due to uncertainties in the muon energy reconstruction in the MRD (see Section

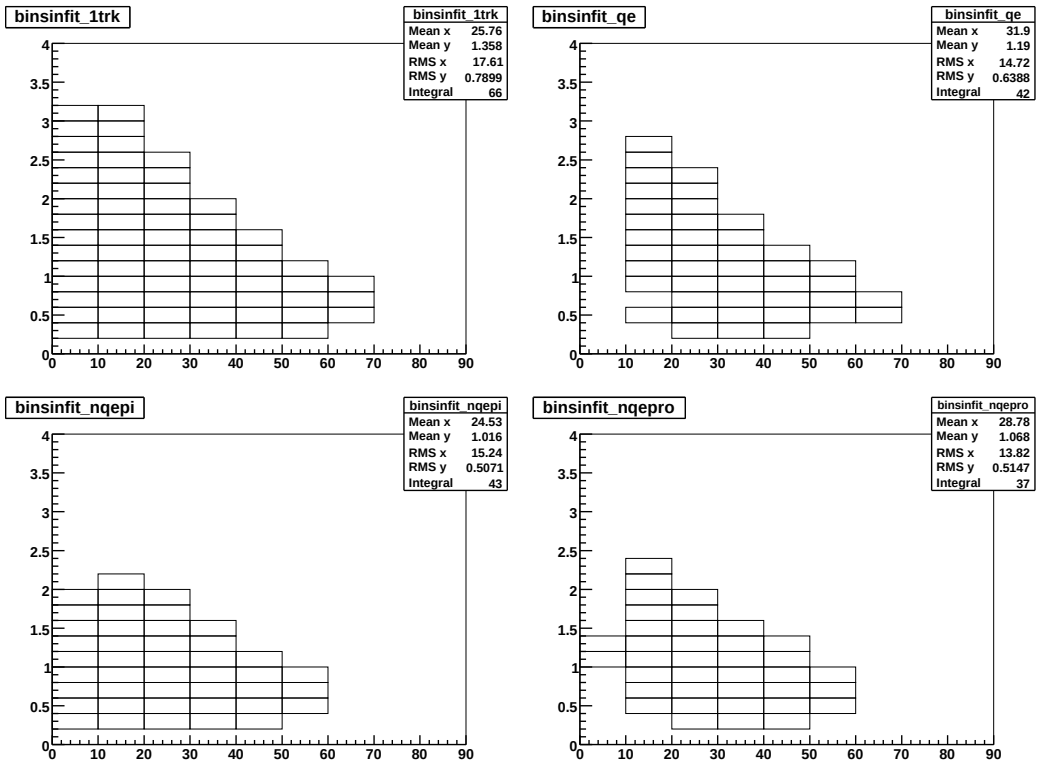

Figure 8.2: Bins used in the fit

2.2.5). P_{sc} is a free parameter in the fit; however, we want to constrain its fit value within the systematic uncertainty. We add a term, F_{Psc}, to the fitting function to constrain P_{sc}.

$$F_{Psc} = \frac{(P_{sc} - 1)^2}{\sigma^2_{P_{sc}}} \tag{8.11}$$

The total minimizing function, F is:

$$F = F_{poisson} + F_{Psc} \tag{8.12}$$

The fit is performed using the ROOT [77] implementation of the Minuit minimization package [78].

8.1.5 Calculation of the Cross Section Ratio

The CC1π^+ to CCQE cross section ratio for neutrino energy bin e, R_e, can be calculated under the assumption that the efficiencies for detecting CCQE and CC1π^+ events in the MRD1&2 sample are the same in data and MC.

$$\begin{aligned} R_e &= \frac{\sigma_e^{CC1\pi^+}}{\sigma_e^{CCQE}} \\ &= \frac{N_{data,e}^{CC1\pi^+}}{N_{data,e}^{CCQE}} \\ &= \frac{N_{data,MRD1\&2,e}^{CC1\pi^+}}{N_{MC,MRD1\&2,e}^{CC1\pi^+}} \times \frac{N_{MC,MRD1\&2,e}^{CCQE}}{N_{data,MRD1\&2,e}^{CCQE}} \times R_{MC,e} \end{aligned} \tag{8.13}$$

where $R_{MC,e}$ is the MC prediction for the cross section ratio. The data values in the above equation are obtained from the fitted MC, as shown below. The overall normalization cancels out.

$$R_e = \frac{\left(R_e^{CC1\pi^+} \sum_{is} N_{ise}^{CC1\pi^+}(P_{sc}) \right) \left(\sum_{is} N_{ise}^{CCQE}(1) \right)}{\left(\sum_{is} N_{ise}^{CC1\pi^+}(1) \right) \left(R^{CCQE} \sum_{is} N_{ise}^{CCQE}(P_{sc}) \right)} R_{MC,e} \tag{8.14}$$

See Appendix A.3 for the details.

8.1.6 Uncertainty in Cross Section Ratio due to Fitting

To determine the uncertainty in R_e due to fitting, the uncertainty in each parameter and the correlation among them is considered using the error matrix, E, from the fit. A diagonal term of the error matrix, E_{ii}, is the square of the total fitting error in parameter i (Par_i). An off-diagonal term, E_{ij}, is the covariance of parameters i and j.

$$\Delta R_e^2(fit) = \sum_{i,j} \frac{\partial R_e}{\partial Par_i} \frac{\partial R_e}{\partial Par_j} E_{ij} \tag{8.15}$$

8.1.7 Uncertainty due to MC Statistics

There is an uncertainty in R_e due to MC statistics. The uncertainty is due to the statistical uncertainty in $R_{MC,e}$ and the statistical uncertainty of the sums of CCQE and CC1π^+ events shown in Equation 8.14. This is quoted as a systematic uncertainty.

8.1.8 Evaluation of Systematic Uncertainties

For each source of systematic uncertainty, a change is made to the nominal MC to evaluate the systematic uncertainty due to that source. A new set of p_μ vs. θ_μ templates is produced with the altered MC. The analysis is performed with the new histogram templates to produce a different result, R_e'. Then the systematic uncertainty is the difference from the nominal result.

$$\Delta R_e(\text{syst}) = R_e' - R_e \tag{8.16}$$

The sources of systematic uncertainty are described below.

Nuclear Effects

- The simulation of pion and nucleon interactions inside the nucleus is described in Section 4.2.5. The uncertainty of the cross sections of pion absorption, pion inelastic scattering, and proton rescattering in the nucleus is considered as a systematic uncertainty. (The cross section of pion charge exchange is much smaller than the others; the effect is negligible). In the momentum range of pions from $\Delta(1232)$ decay, the cross section measurement uncertainty for both pion absorption and pion inelastic scattering is approximately 30% [79]; therefore the cross sections for pion absorption and inelastic scattering are each changed by $\pm 30\%$ to evaluate the systematic uncertainty. The uncertainty in the cross section of proton rescattering inside the nucleus is about 10% [80], and thus the

cross section of proton rescattering is varied by ±10% to evaluate the systematic uncertainty.

- In our simulation, the maximum Fermi momentum of nucleons is set to be 225 MeV/c for oxygen. For carbon, the value should be approximately 221 ± 5 MeV/c [81]. We evaluate the systematic uncertainty due to this effect by eliminating events in which the Fermi momentum of the nucleon is greater than 220 MeV/c.

Detector Effects

- The crosstalk simulation is described in Chapter 5. For the nominal MC, the amount of crosstalk in neighboring channels is set to 3.25%. To evaluate the systematic uncertainty due to the crosstalk model, the crosstalk parameter is changed by its systematic uncertainty of 0.25%, i.e. to 3.0% and 3.5%.

- PMT charge resolution is nominally set at 40%. The estimated uncertainty in this value is 10%, so the resolution is changed by ± 10% to evaluate the systematic effect.

- The model for scintillator quenching relies on Birk's constant, which was measured in SciBar to be 0.0208 ± 0.0023. The constant is changed within its uncertainty (±0.0023) to evaluate the systematic uncertainty due to the model.

Reconstruction Effects

- A (software) hit threshold is nominally set at 2.0 photoelectrons (p.e.) to eliminate hits from noise in data that is not simulated. To evaluate the systematic uncertainty due to the choice of the threshold value, we consider the fact that the spread in the distribution of the energy calibration constant per bar is about 15%. Therefore, we evaluate the uncertainty by increasing the threshold by 15%; we then assume that the uncertainty due to decreasing the threshold is the same magnitude. (We avoid decreasing the threshold, as a lower threshold would be in the region of data-MC discrepancy.)

- The difference in angular resolution between data and MC is considered as a systematic uncertainty. The angular information comes in the form of the variables t_x and t_y, which are the slopes of a track's projection in the x-z and y-z planes, respectively. They can also be thought of as the tangent of the angle the track projection onto the x-z (y-z) plane makes with the z-axis. In Figure 8.3, the solid line is the track projection onto

the x-z plane, and $t_x = \dfrac{\Delta x}{\Delta z} = \tan\theta_x$. From these variables one can calculate the 3D track angles, θ and ϕ.

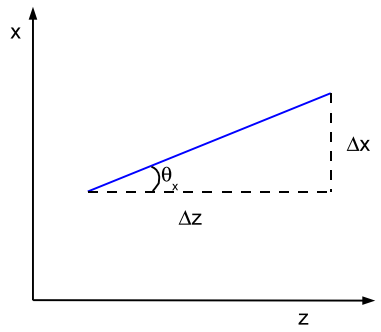

Figure 8.3: $t_x = \Delta x/\Delta z = \tan\theta_x$

To determine the angular resolution in data and MC, we select a sample of muon tracks (the SciBar-MRD matched track in the MRD 1-track sample). Each track is divided into two halves (the upstream half and downstream half), and then each half is fitted to get the t_x value. The difference between the t_x values for the upstream half and downstream halt is called σ_t. (The procedure is the same for t_y). Figure 8.4 shows the distribution of σ_t for data and MC. Both the data and MC distributions are fitted with a Gaussian. The difference between the sigma of the distributions is $\sqrt{0.03091^2 - 0.02965^2} = 0.009$. We evaluate the systematic uncertainty due to this difference in resolution by smearing t_x and t_y in the MC event-by-event by 0.009.

Model Effects

- The axial-vector mass for the CCQE interaction, M_A^{CCQE}, is set to 1.1 GeV/c^2 in our neutrino interaction simulation. The uncertainty in M_A^{CCQE} is estimated to be about ± 0.1 GeV/c^2 in an analysis of data from the SciFi detector[19]. We vary the value within this uncertainty to evaluate the systematic effect. Changing the value of M_A^{CCQE} changes not only the shape of the cross section, but also the overall normalization. In this analysis, we measure the overall normalization of the CCQE cross section, and we only want to quote a systematic uncertainty due to the shape of the cross section. So when varying the M_A^{CCQE} value, the total cross section is reweighted back to the nominal value so the variation only affects the q^2 shape of the CCQE cross section.

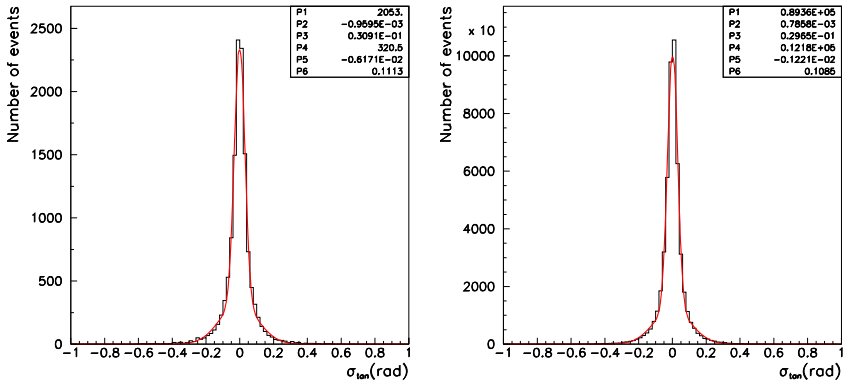

Figure 8.4: σ_t for data (left) and MC (right)

- As described in Section 4.2.3, we apply the Bodek/Yang correction to deep inelastic scattering events. We change the value of the correction factor, 0.188, by ±30%, based on the uncertainty of the model.
- Also as described in Section 4.1.5, we reweight the neutrino flux according to the spectrum fit. To determine the systematic uncertainty due to the flux reweighting, we vary the weighting factors, taking into account their uncertainty and the correlation among them using the error matrix given in Table 4.2

8.2 Results

8.2.1 Fitting Results

We want to measure both the total cross section and the energy-dependency of the CC1π^+ cross section, so the fit is performed twice: once with only one CC1π^+ parameter for the whole energy range and once with a different CC1π^+ parameter for each of the energy bins in Table 8.3.

Result with energy-independent CC1π^+ scaling

The best fit parameters are given in Table 8.4. The errors shown include the effect of correlations between the parameters. The χ^2/d.o.f. at best fit is 228/184 = 1.24. (The nominal χ^2/d.o.f. is 283/184 = 1.54.) Table 8.5 shows the correlation matrix.

For a meaningful interpretation of the fitting parameters, it is necessary to know the normalization at best fit, α, relative to the nominal normalization,

Table 8.4: Best Fit Parameter Values (energy-independent CC1π^+)

Parameter	**Best Fit Value**
P_{sc}	0.974±0.004
R^{CCQE}	0.764±0.070
$R_0^{CC1\pi^+}$	0.758±0.139

Table 8.5: Correlation Matrix (energy-independent CC1π^+)

	P_{sc}	R^{CCQE}	$R_0^{CC1\pi^+}$
P_{sc}	1.000	-0.309	-0.126
R^{CCQE}	-0.309	1.000	0.843
$R_0^{CC1\pi^+}$	-0.126	0.843	1.000

$\alpha_{nominal}$. For example, the number of CCQE interactions in the data relative to the number of CCQE interactions predicted by the nominal MC is

$$\frac{N^{CCQE}(data)}{N^{CCQE}(nominalMC)} = \frac{N^{CCQE}(fittedMC)}{N^{CCQE}(nominalMC)} \approx \frac{\alpha}{\alpha_{nominal}} \times R^{CCQE} \tag{8.17}$$

Similarly,

$$\frac{N_e^{CC1\pi^+}(data)}{N_e^{CC1\pi^+}(nominalMC)} \approx \frac{\alpha}{\alpha_{nominal}} \times R_e^{CC1\pi^+} \tag{8.18}$$

$$\frac{N^{Bkgd}(data)}{N^{Bkgd}(nominalMC)} \approx \frac{\alpha}{\alpha_{nominal}} \tag{8.19}$$

(The above relationship is not exact because the number of events is slightly changed when scaling by P_{sc}.) The value of $\alpha/\alpha_{nominal}$ is 1.24. Table 8.6 gives the number of CCQE, CC1π^+, and background interactions in data relative to the MC prediction.

The fitting results indicate that the CCQE and CC1π^+ cross sections we observe in the data are close to the prediction of the MC model, but we see an excess of background events relative to the MC prediction. The background mostly consists of DIS interactions. The DIS cross section has not been studied extensively in this low energy region, and thus the ∼25% discrepancy we observe is not surprising.

Figure 8.5 shows the comparison of data and best fit MC of the p_μ and θ_μ distributions for each sample. The two-dimensional p_μ vs. θ_μ distributions for the best fit MC are shown in Appendix B.

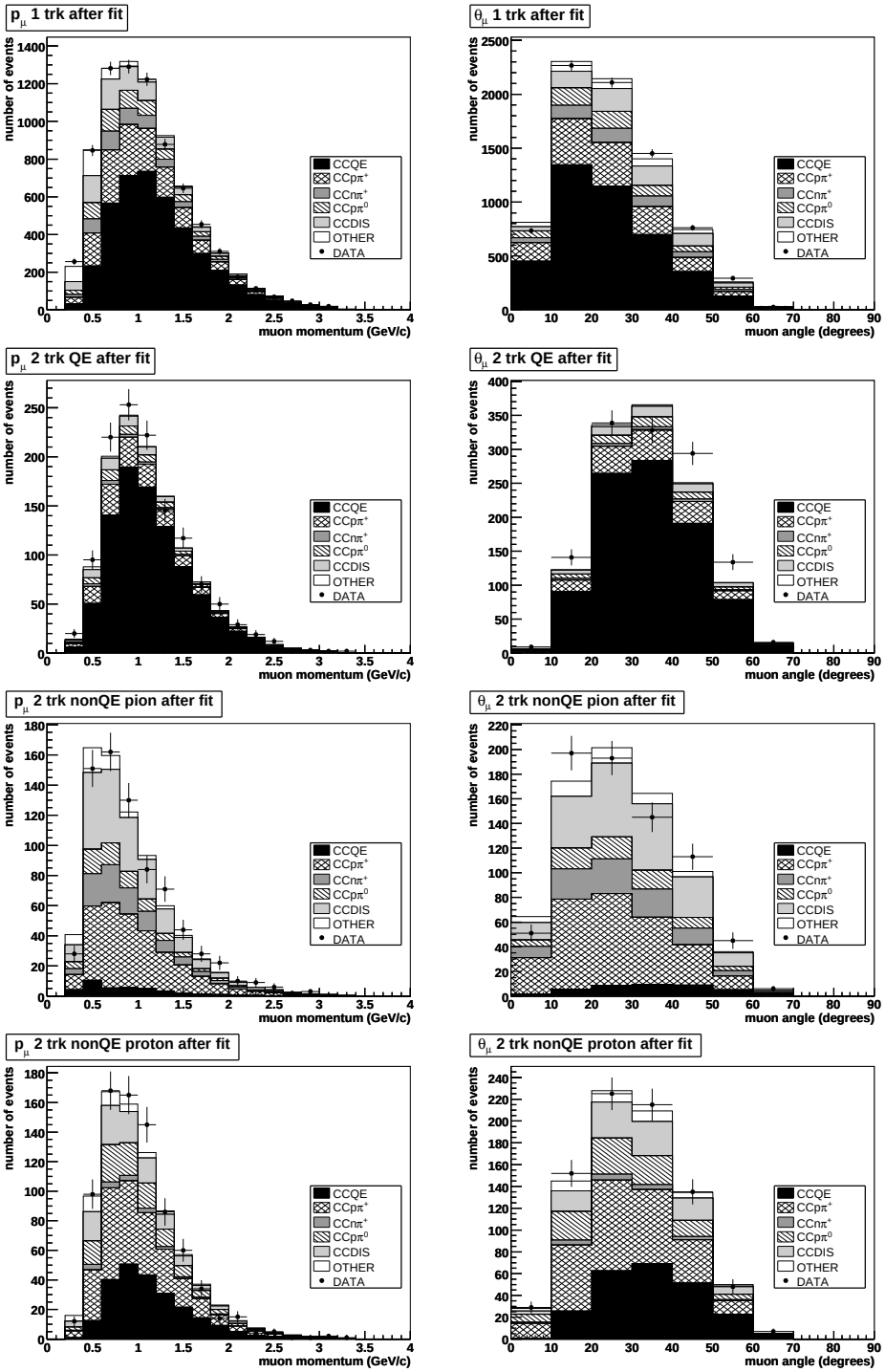

Figure 8.5: p_μ (left) and θ_μ (right) distributions for the data and best fit MC (E_ν-independent CC1π^+) for each sample.

Table 8.6: CCQE, CC1π^+, and background in data relative to MC prediction (energy-independent CC1π^+)

$\frac{N^{CCQE}(data)}{N^{CCQE}(nominalMC)}$	0.95
$\frac{N^{CC1\pi^+}(data)}{N^{CC1\pi^+}(nominalMC)}$	0.94
$\frac{N^{Bkgd}(data)}{N^{Bkgd}(nominalMC)}$	1.24

Result with energy-dependent CC1π^+

The best fit values are given in Table 8.7. The errors shown include the effect of correlations between the parameters. The χ^2/d.o.f. of best fit is 227/181 = 1.25. Table 8.8 shows the correlation matrix. The value of $\alpha/\alpha_{nominal}$ is 1.31. Table 8.9 gives the number of CCQE, CC1π^+ (for each energy bin), and background interactions in data relative to the MC prediction. Figure 8.6 shows the comparison of data and best fit MC of the p_μ and θ_μ distributions for each sample. The two-dimensional p_μ vs. θ_μ distributions for the best fit MC are shown in Appendix B.

Table 8.7: Best Fit Parameter Values (energy-dependent CC1π^+)

Parameter	**Best Fit Value**
P_{sc}	0.977±0.005
R^{CCQE}	0.725±0.071
$R_0^{CC1\pi^+}$	0.545±0.190
$R_1^{CC1\pi^+}$	0.801±0.163
$R_2^{CC1\pi^+}$	0.652±0.170
$R_3^{CC1\pi^+}$	0.798±0.207

8.2.2 Final Results

The final results for the energy-independent and energy-dependent cross section ratios are given in Tables 8.10 and 8.11, respectively.

Table 8.8: Correlation Matrix (energy-dependent CC1π^+)

	P_{sc}	R^{CCQE}	$R_0^{CC1\pi^+}$	$R_1^{CC1\pi^+}$	$R_2^{CC1\pi^+}$	$R_3^{CC1\pi^+}$
P_{sc}	1.000	-0.064	0.248	0.008	0.042	-0.404
R^{CCQE}	-0.064	1.000	0.795	0.610	0.633	0.565
$R_0^{CC1\pi^+}$	0.248	0.795	1.000	0.437	0.679	0.441
$R_1^{CC1\pi^+}$	0.008	0.610	0.437	1.000	0.291	0.570
$R_2^{CC1\pi^+}$	0.042	0.633	0.679	0.291	1.000	0.282
$R_3^{CC1\pi^+}$	-0.404	0.565	0.441	0.570	0.282	1.000

Table 8.9: CCQE, CC1π^+ (for each energy bin), and background in data relative to MC prediction (energy-dependent CC1π^+)

$\frac{N^{CCQE}(data)}{N^{CCQE}(nominalMC)}$	0.95
$\frac{N_0^{CC1\pi^+}(data)}{N_0^{CC1\pi^+}(nominalMC)}$	0.71
$\frac{N_1^{CC1\pi^+}(data)}{N_1^{CC1\pi^+}(nominalMC)}$	1.05
$\frac{N_2^{CC1\pi^+}(data)}{N_2^{CC1\pi^+}(nominalMC)}$	0.85
$\frac{N_3^{CC1\pi^+}(data)}{N_3^{CC1\pi^+}(nominalMC)}$	1.05
$\frac{N^{Bkgd}(data)}{N^{Bkgd}(nominalMC)}$	1.31

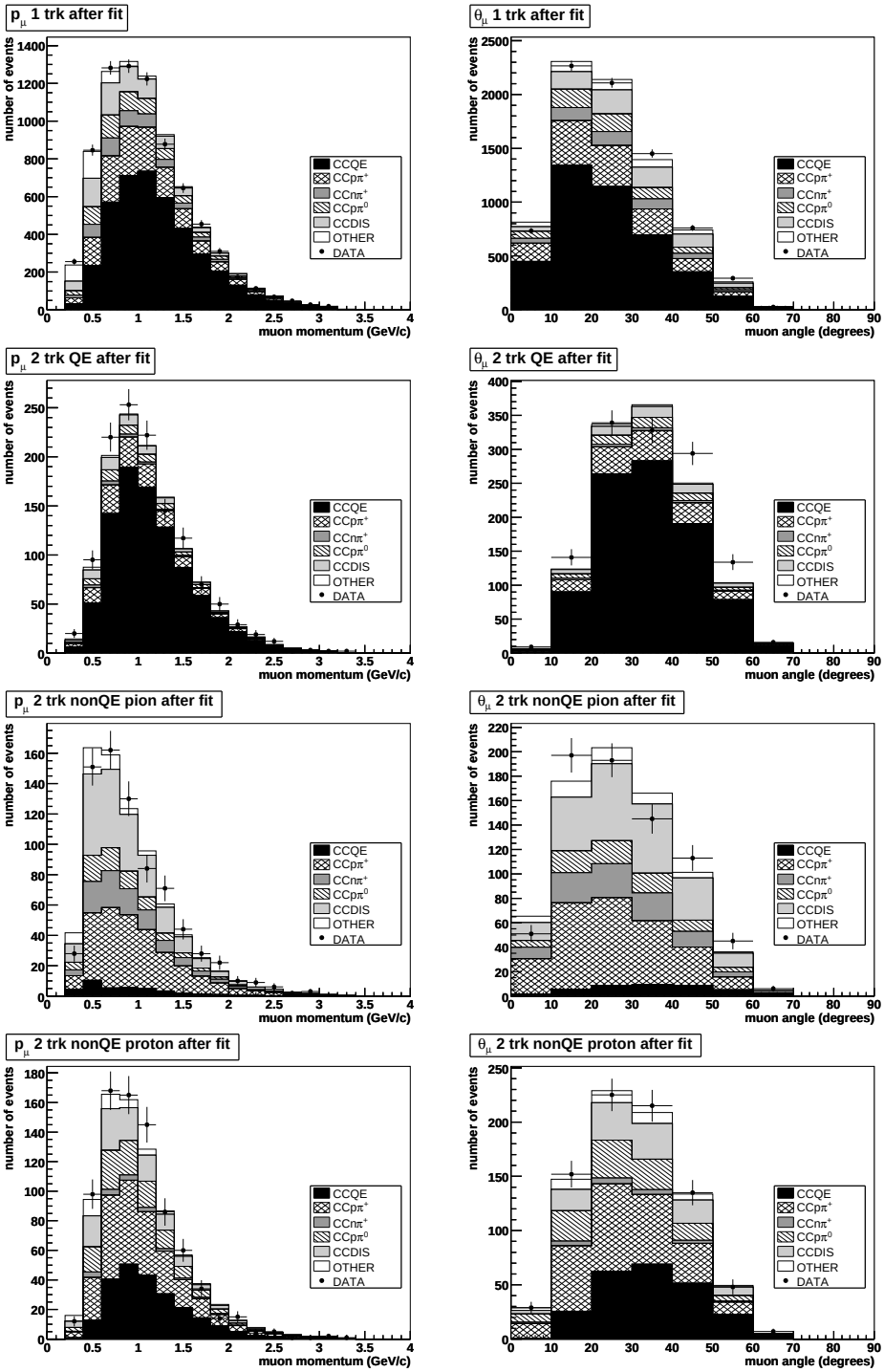

Figure 8.6: p_μ (left) and θ_μ (right) distributions for the data and best fit MC (E_ν-dependent CC1π^+)

Table 8.10: Energy-Independent Cross Section Ratio

Energy Range (GeV)	**Measured Ratio**	**MC Prediction**
>0.00	$0.735 \pm 0.194(\text{fit})^{+0.109}_{-0.126}(\text{syst})$	$0.740 \pm 0.002(\text{stat})$

Table 8.11: Energy-Dependent Cross Section Ratio

Energy Range (GeV)	**Measured Ratio**	**MC Prediction**
0.00-1.35	$0.403 \pm 0.173(\text{fit})^{+0.155}_{-0.118}(\text{syst})$	$0.535 \pm 0.002(\text{stat})$
1.35-1.72	$1.023 \pm 0.281(\text{fit})^{+0.129}_{-0.259}(\text{syst})$	$0.924 \pm 0.005(\text{stat})$
1.72-2.22	$1.006 \pm 0.334(\text{fit})^{+0.323}_{-0.182}(\text{syst})$	$1.117 \pm 0.007(\text{stat})$
>2.22	$1.444 \pm 0.470(\text{fit})^{+0.391}_{-0.543}(\text{syst})$	$1.300 \pm 0.013(\text{stat})$

8.2.3 Summary of Systematic Uncertainties

Tables 8.12 and 8.13 give a summary of the systematic uncertainties of the energy-independent and energy-dependent cross section ratios, respectively.

For the calculation of total systematic uncertainty, if a particular effect has systematic uncertainties in the same direction, only the larger value is used in the calculation of total systematic uncertainty. For example, in Table 8.12, for pion absorption $\pm 30\%$, the uncertainties are +0.046 and +0.014; 0.046 is used and 0.014 is not used in the calculation of the total systematic uncertainty in the positive direction.

Table 8.12: Syst. Uncertainties for Energy-Independent Ratio

Condition	ΔR_0
Detector Simulation	
Crosstalk ±0.25%	+0.042,-0.010
PMT Res. ±10%	+0.006,-0.017
Birks' Const. ±0.0023	-0.010,+0.036
Reconstruction	
Threshold ±15%	±0.022
Angular res.	±0.010
Model	
M_A^{QE} ±0.1 GeV	-0.056,+0.049
Bodek/Yang Corr. ±30%	+0.003,-0.018
Neutrino Flux	+0.006,-0.028
Nuclear Effects	
π abs. ±30%	+0.046,+0.014
π inel. scat. ±30%	+0.059,-0.068
proton rescat. ±10%	-0.076,+0.004
Fermi mom.	±0.012
MC Stats.	±0.006
Total Syst. Error	**-0.126,+0.109**

Table 8.13: Syst. Uncertainties for Energy-Dependent Ratio

Condition	ΔR_0	ΔR_1	ΔR_2	ΔR_3
Detector Simulation				
Crosstalk ±0.25%	+0.023,+0.086	+0.031,-0.079	+0.104,+0.075	+0.058,-0.212
PMT Res. ±10%	-0.007,-0.018	+0.012,-0.026	+0.024,-0.002	-0.010,-0.077
Birks' Const. ±0.0023	+0.009,+0.042	-0.024,+0.046	-0.003,+0.100	-0.047,-0.131
Reconstruction				
Threshold ±15%	±0.013	±0.045	±0.014	±0.162
Angular res.	±0.015	±0.001	±0.021	±0.023
Model				
M_A^{QE} ±0.1 GeV	-0.039,+0.015	-0.054,+0.048	-0.031,+0.021	-0.270,+0.276
Bodek/Yang Corr. ±30%	+0.007,-0.014	+0.006,-0.021	+0.022,-0.030	-0.046,-0.037
Neutrino Flux	+0.082,-0.079	+0.061,-0.082	+0.192,-0.162	+0.047,-0.207
Nuclear Effects				
π abs. ±30%	+0.022,+0.077	+0.006,-0.053	+0.129,+0.106	+0.203,-0.052
π inel. scat. ±30%	+0.031,+0.018	+0.069,-0.173	+0.155,+0.032	+0.019,-0.243
proton rescat. ±10%	-0.072,+0.025	-0.119,-0.019	-0.063,+0.059	-0.135,-0.080
Fermi mom.	±0.004	±0.020	±0.009	±0.035
MC Stats.	±0.006	±0.015	±0.017	±0.037
Total Syst. Error	**-0.118,+0.155**	**-0.259,+0.129**	**-0.182,+0.323**	**-0.543,+0.391**

Chapter 9

Conclusion

The main result presented in the previous chapter is for the inclusive CC1π^+ cross section, i.e. the CCpπ^+ and CCnπ^+ modes taken together. We also measure the exclusive CCpπ^+ cross section. The method is exactly the same as the main analysis, except that CCnπ^+ events are considered part of the background. The detailed results of the exclusive measurement are given in Appendix C. In the following section, I will compare the results of both the inclusive and exclusive cross section ratio measurements with MC predictions and previous experimental results.

9.1 Comparison with the MC Model and Previous Experiments

Shown in Figures 9.1 and 9.2 is the comparison of the results for the inclusive and exclusive cross section ratios, respectively, with the SciBar MC predictions. In these plots, the black points and lines represent the result with fitting error, while the gray boxes represent the total uncertainty (uncertainties due to fitting and systematic sources added in quadrature). The width of the gray box represents the size of the neutrino energy bin.

To compare these results with previous experiments, we must calculate the CC1π^+ (or CCpπ^+) to CCQE cross section ratios from absolute cross section measurements from these previous experiments. There are only a few experiments that have made measurements of the CC1π interaction for muon neutrinos in K2K's neutrino energy region. The Argonne (ANL) bubble chamber experiment provided cross section measurements of all three CC1π interaction modes [49] and the CCQE interaction [39] for muon neutrinos with a

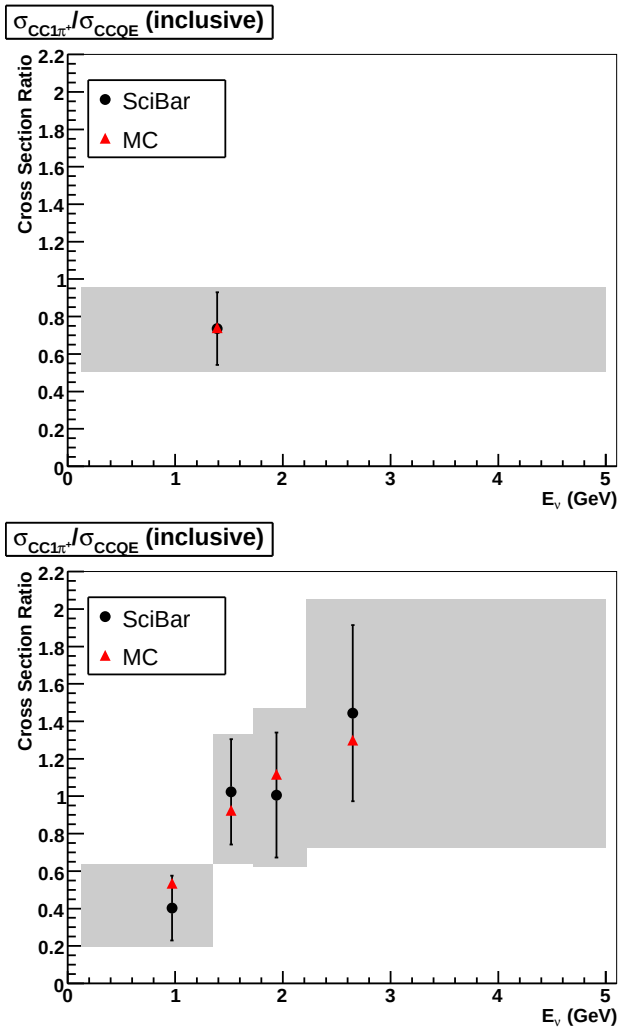

Figure 9.1: Comparison of the results with the MC prediction for the total cross section ratio (upper) and the energy-dependent cross section ratio (lower).

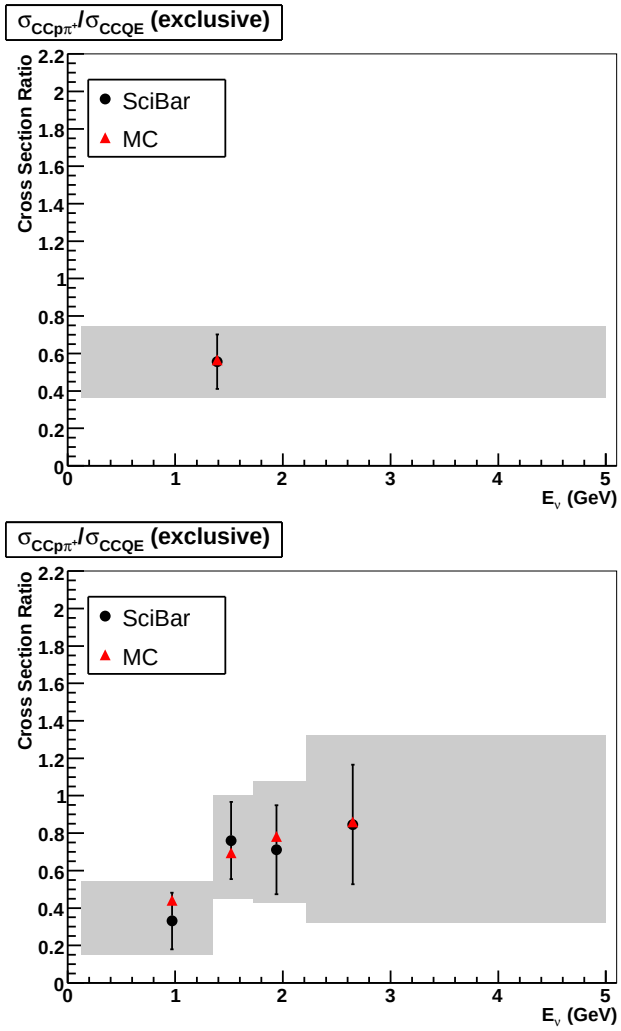

Figure 9.2: Comparison of the results for the exclusive cross section ratio with the MC prediction for the total cross section ratio (upper) and the energy-dependent cross section ratio (lower).

peak energy of 0.5 GeV. The Brookhaven (BNL) bubble chamber experiment also made measurements of all three CC1π modes [48] with muon neutrinos with an average energy of 1.6 GeV. They did not publish a measurement of the CCQE cross section, though they did measure the CCQE axial-vector mass, M_A [82]. They also published a measurement of the exclusive CC$p\pi^+$ to CCQE ratio [83]. The Gargamelle (GGM) bubble chamber experiment at CERN measured cross sections for muon neutrinos with energy less than 10 GeV. They measured the CCQE cross section [84], and for the CC1π interaction, they only measured the cross section of the CC$p\pi^+$ mode [50]. Using the published results from these experiments, the CC1π^+ (and CC$p\pi^+$) to CCQE cross section ratio for each experiment can be calculated. The calculated cross section ratios are given in Appendix D.

To compare the SciBar result with previous experiments, the composition of our detector must be taken into account. SciBar is made of polystyrene, C_8H_8, which has 56 protons and 48 neutrons. The cross section ratio must be scaled to account for the fact that there are more protons than neutrons. The details are discussed in Appendix E. Figures 9.3 and 9.4 show a comparison of the scaled inclusive and exclusive cross section ratios, respectively, with results from other experiments. Again, the black points and gray boxes are the SciBar result with the total uncertainty. The width of the gray box represents the size of the neutrino energy bin.

These results are consistent with the prediction made using the Rein and Sehgal model and the previous experimental data.

9.2 Summary and Outlook

A measurement of the cross section for single charged pion production via resonance in charged-current neutrino interactions with carbon is made with data from the SciBar detector as part of the K2K experiment. The result serves to test the predictions of the Rein and Sehgal model and verify old experimental measurements. While the results do not improve on precision, they serve as a useful cross-check in a region with few measurements. The use of a carbon target, a commonly used material in neutrino detectors, will aid in understanding nuclear effects in neutrino interactions.

Other oscillation experiments are using their detectors to make neutrino cross section measurements. For example, the MiniBooNE neutrino oscillation experiment has published a preliminary result for the CC1π^+ cross section [85]. There are also plans for neutrino experiments with the explicit purpose of measuring cross sections. The SciBar detector has been moved to FNAL to become part of the SciBooNE experiment; it will take data to study both neutrino and anti-neutrino cross sections. MINERvA is a neutrino scattering experiment that will study low-energy neutrino cross sections at FNAL starting

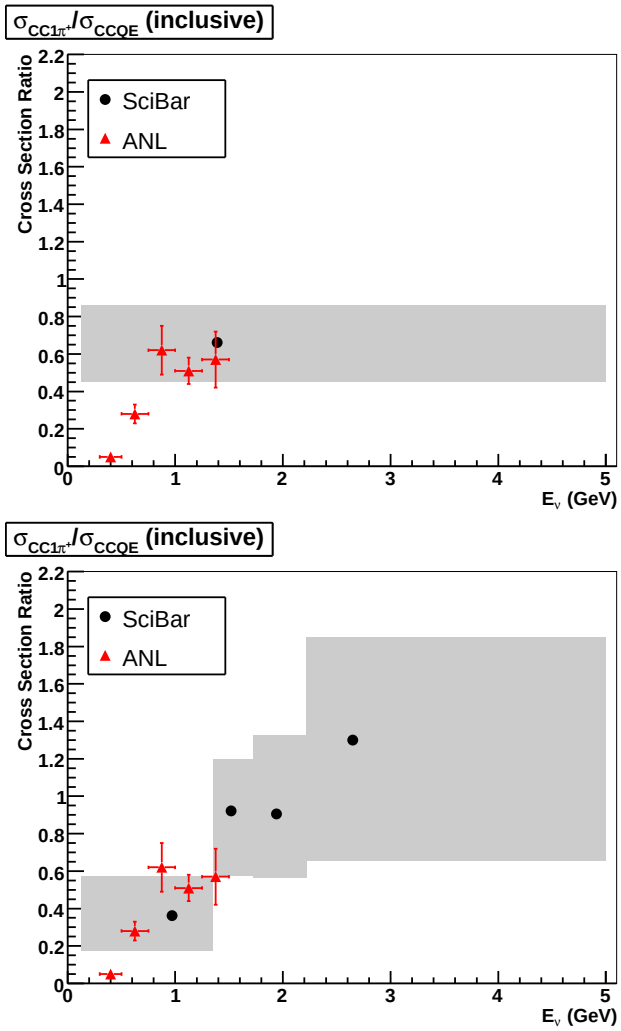

Figure 9.3: Comparison of the results for the inclusive cross section ratio with results from ANL [49],[39]

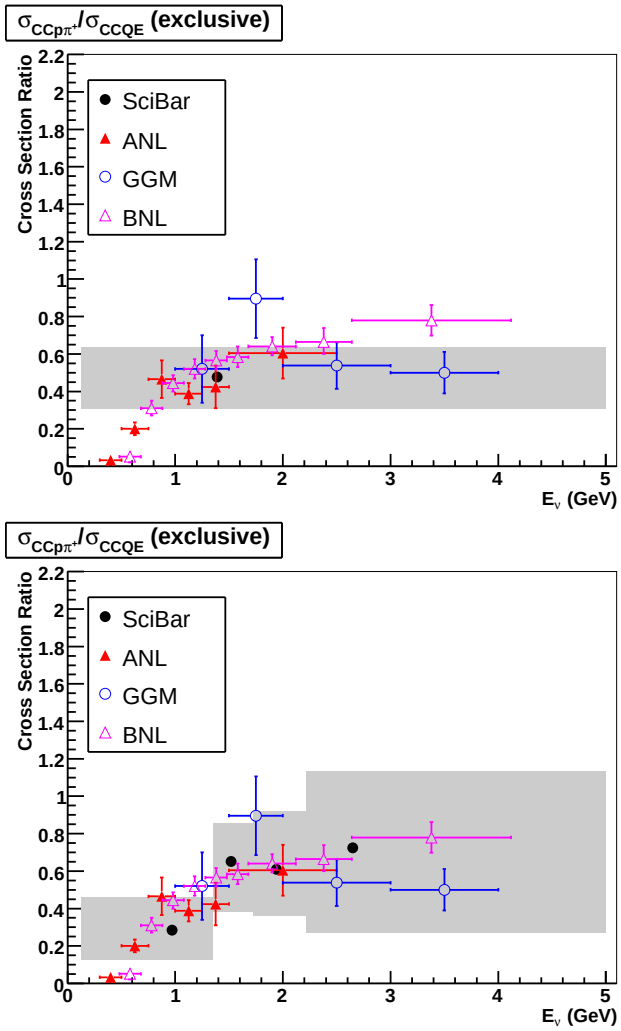

Figure 9.4: Comparison of the results for the exclusive cross section ratio with results from ANL [49],[39], GGM [84],[50], and BNL [83].

in 2009. In the next few years, these neutrino cross section studies will shine light on weak interactions and open the door for precise understanding of the phenomenon of neutrino oscillations.

Appendix A

Calculations

A.1 Kinematic Reconstruction

The z axis of the detector does not exactly correspond to the neutrino beam direction; the neutrino beam is oriented slightly downward from horizontal, $\phi_{beam} = -1.075°$. Thus the neutrino's momentum vector in the coordinate system of the detector is

$$\vec{p_\nu} = \langle 0, E_\nu \sin\phi_{beam}, E_\nu \cos\phi_{beam} \rangle \tag{A.1}$$

A.1.1 Calculation of Neutrino Energy

In a charged-current quasi-elastic (CCQE) event, $\nu n \to \mu^- p$, a neutrino strikes a target neutron. Conservation of momentum implies:

$$\begin{aligned} p_{\mu x} + p_{px} &= 0 \\ p_{\mu y} + p_{py} &= E_\nu \sin\phi_{beam} \\ p_{\mu z} + p_{pz} &= E_\nu \cos\phi_{beam} \end{aligned} \tag{A.2}$$

Using conservation of energy, we can solve for the neutrino's energy, E_ν, as follows:

$$E_\nu + m_n - V = E_\mu + E_p$$

$$(E_\nu - E_\mu) + (m_n - V) = E_p = \sqrt{m_p^2 + p_p^2}$$

$$[(E_\nu - E_\mu) + (m_n - V)]^2 = m_p^2 + p_{px}^2 + p_{py}^2 + p_{pz}^2$$

$$(E_\nu - E_\mu)^2 + (m_n - V)^2 + 2(E_\nu - E_\mu)(m_n - V)$$
$$= m_p^2 + p_{\mu x}^2 + (E_\nu \sin\phi_{beam} - p_{\mu y})^2 + (E_\nu \cos\phi_{beam} - p_{\mu z})^2$$

$$E_\nu^2 - 2E_\nu E_\mu + E_\mu^2 + (m_n - V)^2 + 2E_\nu(m_n - V) - 2E_\mu(m_n - V)$$
$$= m_p^2 + p_{\mu x}^2 + E_\nu^2 \sin^2\phi_{beam} + p_{\mu y}^2 - 2E_\nu \sin\phi_{beam} p_{\mu y} + E_\nu^2 \cos^2\phi_{beam} + p_{\mu z}^2 - 2E_\nu \cos\phi_{beam} p_{\mu z}$$

$$E_\nu^2 - 2E_\nu E_\mu + E_\mu^2 + (m_n - V)^2 + 2E_\nu(m_n - V) - 2E_\mu(m_n - V)$$
$$= m_p^2 + (p_{\mu x}^2 + p_{\mu y}^2 + p_{\mu z}^2) + E_\nu^2(\sin^2\phi_{beam} + \cos^2\phi_{beam}) - 2E_\nu(\sin\phi_{beam} p_{\mu y} + \cos\phi_{beam} p_{\mu z})$$

$$-2E_\nu E_\mu + E_\mu^2 + (m_n - V)^2 + 2E_\nu(m_n - V) - 2E_\mu(m_n - V)$$
$$= m_p^2 + p_\mu^2 - 2E_\nu(\sin\phi_{beam} p_{\mu y} + \cos\phi_{beam} p_{\mu z})$$

$$-2E_\nu E_\mu + 2E_\nu(m_n - V) + 2E_\nu(\sin\phi_{beam} p_{\mu y} + \cos\phi_{beam} p_{\mu z})$$
$$= -E_\mu^2 - (m_n - V)^2 + 2E_\mu(m_n - V) + m_p^2 + p_\mu^2$$

$$2E_\nu[-E_\mu + (m_n - V) + \sin\phi_{beam} p_{\mu y} + \cos\phi_{beam} p_{\mu z}]$$
$$= m_p^2 + (p_\mu^2 - E_\mu^2) - (m_n - V)^2 + 2E_\mu(m_n - V)$$

$$2E_\nu[-E_\mu + (m_n - V) + \sin\phi_{beam} p_{\mu y} + \cos\phi_{beam} p_{\mu z}] =$$
$$m_p^2 - m_\mu^2 - (m_n - V)^2 + 2E_\mu(m_n - V)$$

$$E_\nu = \frac{1}{2}\frac{m_p^2 - m_\mu^2 - (m_n - V)^2 + 2E_\mu(m_n - V)}{[-E_\mu + (m_n - V) + \sin\phi_{beam} p_{\mu y} + \cos\phi_{beam} p_{\mu z}]}$$

$$E_\nu = \frac{E_\mu(m_n - V) + \frac{1}{2}\left(m_p^2 - (m_n - V)^2 - m_\mu^2\right)}{(m_n - V) - E_\mu + \sin\phi_{beam} p_{\mu y} + \cos\phi_{beam} p_{\mu z}} \tag{A.3}$$

where E = energy, m = mass, p = momentum, V = nuclear potential = 27 MeV, and the subscripts p, n, μ, ν represent the proton, neutron, muon, and neutrino, respectively.

The neutrino energy reconstruction described above is not accurate if the interaction is not actually CCQE. For nonQE events, the reconstructed neutrino energy is less than the true energy; the reconstruction assumes a two-body interaction, but there are additional particles that are produced. Figure A.1 shows the neutrino energy resolution for the SciBar-MRD sample when the neutrino energy is reconstructed as CCQE. Figure A.2 shows the neutrino energy resolution in 2-track QE like sample which has a CCQE purity of 78%. There is still a bias in the energy reconstruction because of contamination by nonQE events, but it is less significant. The energy resolution for these events is about 200 MeV.

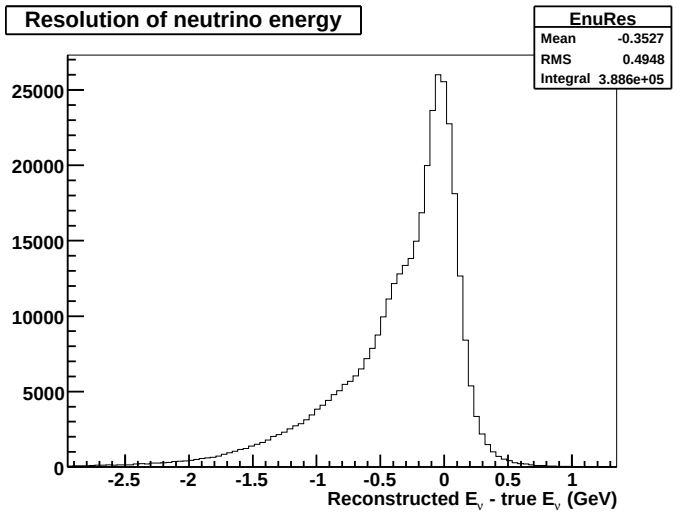

Figure A.1: The E_ν resolution when the energy is reconstructed assuming CCQE interaction for the entire MRD sample. The reconstructed energy tends to be less than the true energy due to the reconstruction assumption that each event is a two-body interaction.

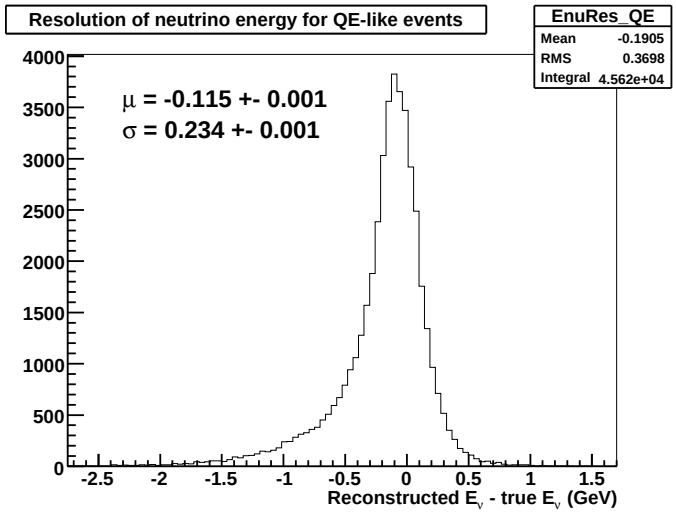

Figure A.2: The E_ν resolution when the energy is reconstructed assuming CCQE interaction for only the 2-track QE sample. There is still a small bias in the energy reconstruction for these events. The resolution is about 200 MeV.

A.1.2 Calculation for QE/nonQE-like Separation

$\Delta\theta_p$ is defined as the angle between expected proton direction (assuming a CCQE interaction) and the observed direction of the second track. Let $\vec{p_p}$ be the expected proton momentum vector and $\vec{p_2}$ be the momentum vector of the observed second track. The angle between the two vectors is calculated as follows:

$$\cos\Delta\theta_p = \frac{\vec{p_p}}{|\vec{p_p}|} \cdot \frac{\vec{p_2}}{|\vec{p_2}|} \tag{A.4}$$

From equation A.2,

$$\vec{p_p} = \langle -p_{\mu x}, E_\nu \sin\phi_{beam} - p_{\mu y}, E_\nu \cos\phi_{beam} - p_{\mu z}\rangle \tag{A.5}$$

Therefore,

$$\frac{\vec{p_p}}{|\vec{p_p}|} = \frac{\langle -p_{\mu x}, E_\nu \sin\phi_{beam} - p_{\mu y}, E_\nu \cos\phi_{beam} - p_{\mu z}\rangle}{\sqrt{p_{\mu x}^2 + (E_\nu \sin\phi_{beam} - p_{\mu y})^2 + (E_\nu \cos\phi_{beam} - p_{\mu z})^2}} \tag{A.6}$$

The angular information for each track is given by the variables t_x and t_y, which are the slopes of a track's projection in the x-z and y-z planes, respectively. $\frac{\vec{p_2}}{|\vec{p_2}|}$ is just a unit vector in the direction of the observed second track, which can be represented as

$$\frac{\vec{p_2}}{|\vec{p_2}|} = \frac{\langle t_{x2}, t_{y2}, 1\rangle}{\sqrt{t_{x2}^2 + t_{y2}^2 + 1}} \tag{A.7}$$

Therefore,

$$\cos\Delta\theta_p = \frac{-p_{\mu x}t_{x2} + (E_\nu \sin\phi_{beam} - p_{\mu y})t_{y2} + (E_\nu \cos\phi_{beam} - p_{\mu z})}{\sqrt{p_{\mu x}^2 + (E_\nu \sin\phi_{beam} - p_{\mu y})^2 + (E_\nu \cos\phi_{beam} - p_{\mu z})^2}\sqrt{t_{x2}^2 + t_{y2}^2 + 1}} \tag{A.8}$$

and

$$\Delta\theta_p = \arccos(\cos\Delta\theta_p) \tag{A.9}$$

We need to make an adjustment in this calculation if the second track is backward, that is, the downstream end of the track is closer than the upstream end to the muon vertex. In Figure A.3, the muon track is labeled $\boldsymbol{\mu}$, the expected proton track is labeled **p**, and tracks **1** and **2** are examples of candidate proton tracks. Track **1** is forward and track **2** is backward. We want to calculate $\Delta\theta_p(1)$, the angle between the expected proton track and track **1**, and $\Delta\theta_p(2)$, the angle between the expected proton track and track **2**.

The variable t_x is just the slope of the line created when the track is

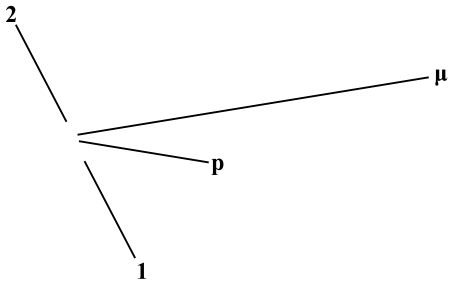

Figure A.3: The muon track is labeled $\boldsymbol{\mu}$, the expected proton track is labeled **p**, and tracks **1** and **2** are examples of candidate proton tracks. Track **1** is forward and track **2** is backward.

projected on the x-z plane (etc. for t_y). So in Figure A.3, $t_x(1) = t_x(2)$ because the lines have the same slope. Defining $\vec{p} = \langle t_x, t_y, 1\rangle$, means that $\vec{p}(1) = \vec{p}(2)$, shown in Figure A.4. And so we get $\Delta\theta_p(1) = \Delta\theta_p(2) = \alpha$.

Clearly, this is not correct; the vectors for track **1** and track **2** should be in opposite directions, and $\Delta\theta_p(2) = 180^\circ - \alpha$, as can be seen in Figure A.5. However, our definition, $\vec{p} = \langle t_x, t_y, 1\rangle$, forces the z component of $\vec{p}$ to be positive.

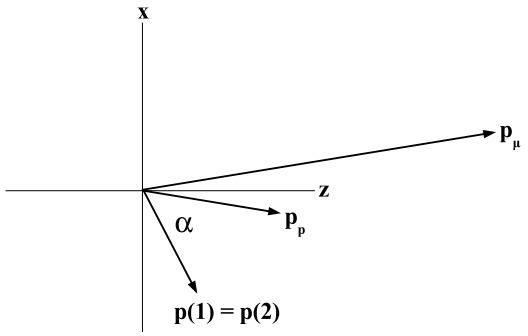

Figure A.4: Momentum vectors of the tracks shown in Figure A.3. Defining $\vec{p} = \langle t_x, t_y, 1\rangle$ gives tracks **1** and **2** the same momentum vector, which is incorrect.

To correct this, we take $\vec{p} \to -\vec{p}$ for backward tracks. In this example, this means $\vec{p}(2) = -\vec{p}(1)$. So then $\cos\Delta\theta_p(2) = -\cos\Delta\theta_p(1) = -\cos\alpha$. This

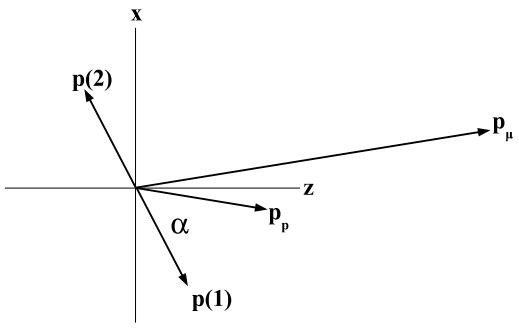

Figure A.5: Correct momentum vectors of the tracks shown in Figure A.3. (Track **2** correctly points backwards.)

gives us the correct result for $\Delta\theta_p(2)$ because:
$\arccos(\cos\Delta\theta_p(2)) = \arccos(-\cos\Delta\theta_p(1)) = \arccos(-\cos\alpha) = 180^\circ - \alpha$.

A.2 Poisson Maximum Likelihood

Equation 8.3:

$$
\begin{aligned}
F_{poisson} &= -2\ln\lambda \\
&= -2\ln\frac{f(\vec{n},\vec{\mu}(\vec{\theta}))}{f(\vec{n},\vec{n})} \\
&= -2\ln\frac{\prod P(n_i,\mu_i(\vec{\theta}))}{\prod P(n_i,n_i)} \\
&= -2\left[\ln\prod P(n_i,\mu_i(\vec{\theta})) - \ln\prod P(n_i,n_i)\right] \\
&= -2\left[\sum \ln P(n_i,\mu_i(\vec{\theta})) - \sum \ln P(n_i,n_i)\right] \\
&= -2\sum\left[\ln P(n_i,\mu_i(\vec{\theta})) - \ln P(n_i,n_i)\right] \\
&= -2\sum\left[\ln\frac{\mu_i^{n_i}e^{-\mu_i}}{n_i!} - \ln\frac{n_i^{n_i}e^{-n_i}}{n_i!}\right] \\
&= -2\sum\left[n_i\ln\mu_i - \mu_i - \ln n_i! - n_i\ln n_i + n_i + \ln n_i!\right] \\
&= -2\sum\left[n_i(\ln\mu_i - \ln n_i) - \mu_i + n_i\right] \\
&= 2\sum\left[n_i(\ln n_i - \ln\mu_i) + \mu_i - n_i\right] \\
F_{poisson} &= 2\sum\left[\mu_i(\vec{\theta}) - n_i + n_i\ln\frac{n_i}{\mu_i(\vec{\theta})}\right] \qquad \text{(A.10)}
\end{aligned}
$$

Equation 8.4:

$$
\begin{aligned}
F^i_{poisson} &= -2\left[\ln\frac{\mu_i^0 e^{-\mu_i}}{0!} - \ln\frac{0^0 e^{-0}}{0!}\right] \\
&= -2\left[\ln e^{-\mu_i} - \ln 1\right] \\
&= 2\mu_i \qquad \text{(A.11)}
\end{aligned}
$$

Equation 8.5

$$
\begin{aligned}
F^i_{poisson} &= -2\left[\ln\frac{0^{n_i}e^{-0}}{n_i!} - \ln\frac{n_i^{n_i}e^{-n_i}}{n_i!}\right] \\
&= \text{undefined} \qquad \text{(A.12)}
\end{aligned}
$$

A.3 Calculation of Cross Section Ratio

To calculate the cross section ratio R_e, we assume that the efficiencies for detecting CC1π^+ or CCQE events in the MRD1&2 sample, $e^{CC1\pi^+}_{MRD12,e}$ and $e^{CCQE}_{MRD12,e}$, are the same in data and MC.

Equation 8.13:

$$\begin{aligned}
R_e &= \frac{\sigma_e^{CC1\pi+}}{\sigma_e^{CCQE}} \\
&= \frac{N_{data,e}^{CC1\pi+}}{N_{data,e}^{CCQE}} \\
&= \frac{N_{data,MRD12,e}^{CC1\pi+}/e_{data,MRD12,e}^{CC1\pi+}}{N_{data,MRD12,e}^{CCQE}/e_{data,MRD12,e}^{CCQE}} \\
&= \frac{N_{data,MRD12,e}^{CC1\pi+}/e_{MC,MRD12,e}^{CC1\pi+}}{N_{data,MRD12,e}^{CCQE}/e_{MC,MRD12,e}^{CCQE}} \\
&= \frac{N_{data,MRD12,e}^{CC1\pi+}}{N_{data,MRD12,e}^{CCQE}} \times e_{MC,MRD12,e}^{CCQE} \times \frac{1}{e_{MC,MRD12,e}^{CC1\pi+}} \\
&= \frac{N_{data,MRD12,e}^{CC1\pi+}}{N_{data,MRD12,e}^{CCQE}} \times \frac{N_{MC,MRD12,e}^{CCQE}}{N_{MC,e}^{CCQE}} \times \frac{N_{MC,e}^{CC1\pi+}}{N_{MC,MRD12,e}^{CC1\pi+}} \\
&= \frac{N_{data,MRD12,e}^{CC1\pi+}}{N_{MC,MRD12,e}^{CC1\pi+}} \times \frac{N_{MC,MRD12,e}^{CCQE}}{N_{data,MRD12,e}^{CCQE}} \times \frac{N_{MC,e}^{CC1\pi+}}{N_{MC,e}^{CCQE}} \\
R_e &= \frac{N_{data,MRD12,e}^{CC1\pi+}}{N_{MC,MRD12,e}^{CC1\pi+}} \times \frac{N_{MC,MRD12,e}^{CCQE}}{N_{data,MRD12,e}^{CCQE}} \times R_{MC,e} \qquad \text{(A.13)}
\end{aligned}$$

where e is the neutrino energy bin, $R_{MC,e}$ is the MC prediction for the cross section ratio, $\sigma_e^{CC1\pi+}$ and σ_e^{CCQE} are the observed CC1π^+ and CCQE cross sections, respectively, $N_e^{CC1\pi^+}$ means the total number of CC1π^+ events, and $N^{CC1\pi^+}_{MRD12,e}$ means number the CC1π^+ events in the MRD 1&2 track sample (similarly for CCQE).

Equation 8.14:

$$R_e = \frac{N^{CC1\pi+}_{data,MRD12,e}}{N^{CC1\pi+}_{MC,MRD12,e}} \times \frac{N^{CCQE}_{MC,MRD12,e}}{N^{CCQE}_{data,MRD12,e}} \times R_{MC,e}$$

$$= \frac{\alpha R^{CC1\pi+}_e \sum_{is} N^{CC1\pi+}_{ise}(P_{sc})}{\alpha_{nominal} \sum_{is} N^{CC1\pi+}_{ise}(1)} \times \frac{\alpha_{nominal} \sum_{is} N^{CCQE}_{ise}(1)}{\alpha R^{CCQE} \sum_{is} N^{CCQE}_{ise}(P_{sc})} \times R_{MC,e}$$

$$R_e = \frac{R^{CC1\pi+}_e \sum_{is} N^{CC1\pi+}_{ise}(P_{sc})}{\sum_{is} N^{CC1\pi+}_{ise}(1)} \times \frac{\sum_{is} N^{CCQE}_{ise}(1)}{R^{CCQE} \sum_{is} N^{CCQE}_{ise}(P_{sc})} \times R_{MC,e} \quad \text{(A.14)}$$

Appendix B

Muon Momentum vs. Angle Plots

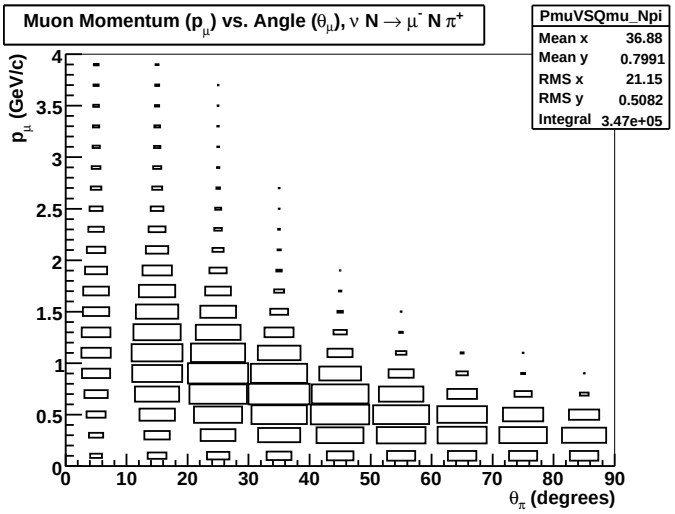

Figure B.1: p_μ vs. θ_μ distributions for MC CC1π^+ events

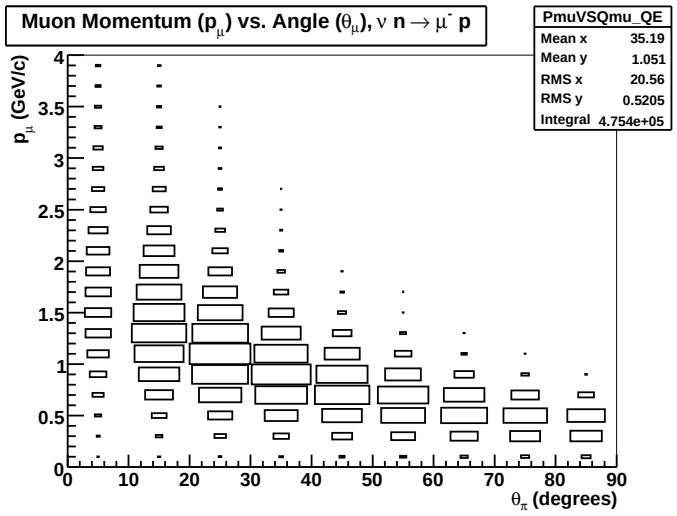

Figure B.2: p_μ vs. θ_μ distributions for MC CCQE events

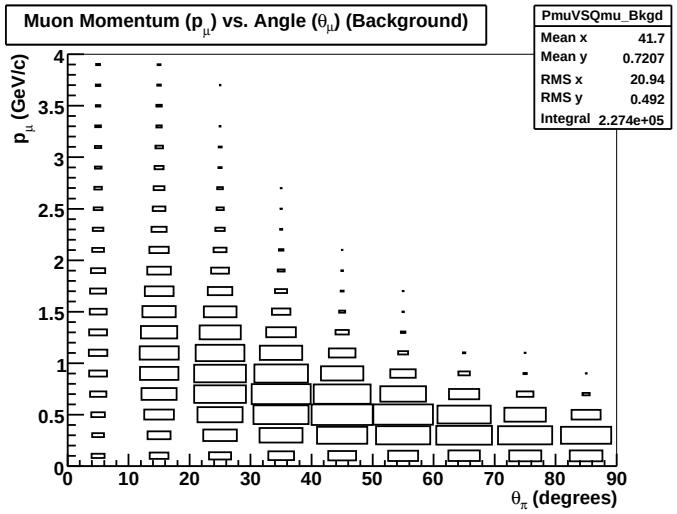

Figure B.3: p_μ vs. θ_μ distributions for MC background events

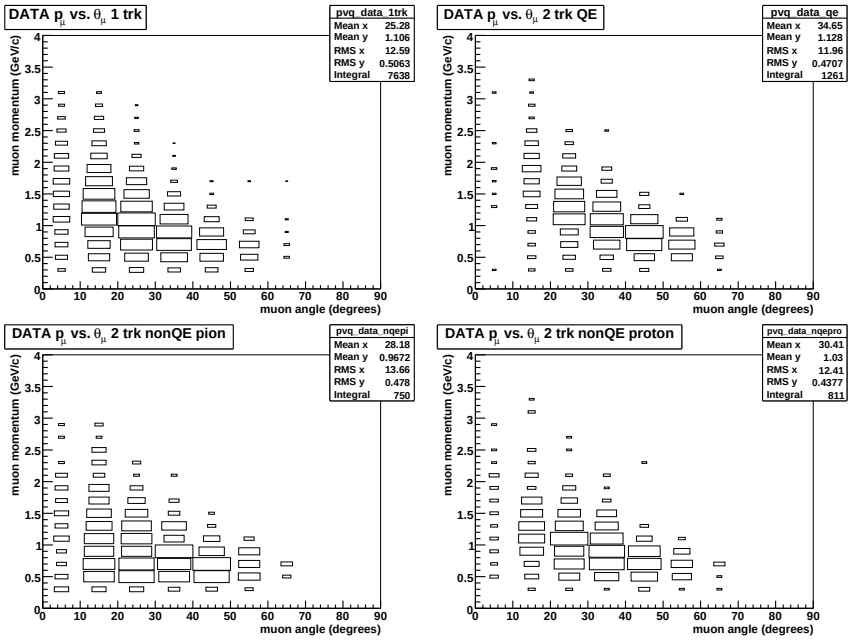

Figure B.4: p_μ vs. θ_μ distributions for the data

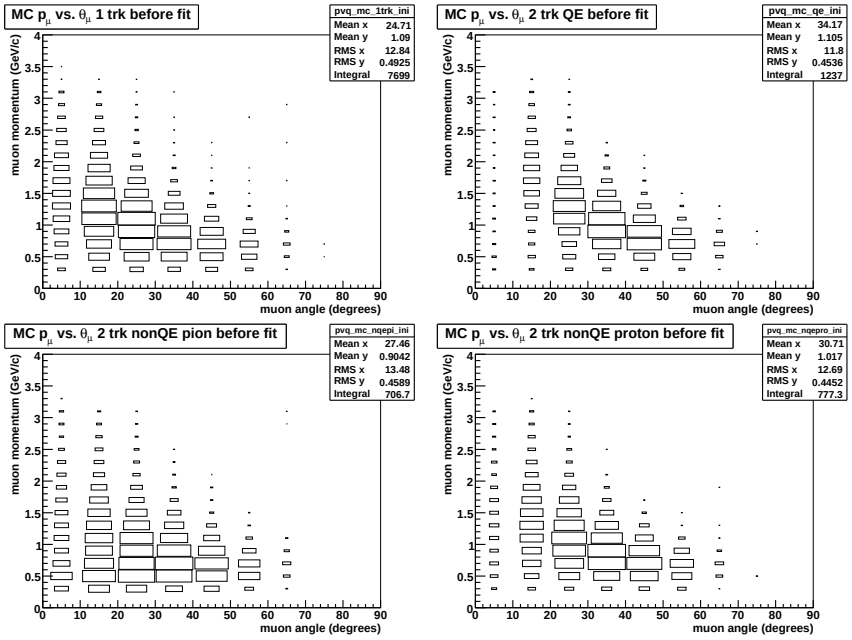

Figure B.5: p_μ vs. θ_μ distributions for the nominal MC

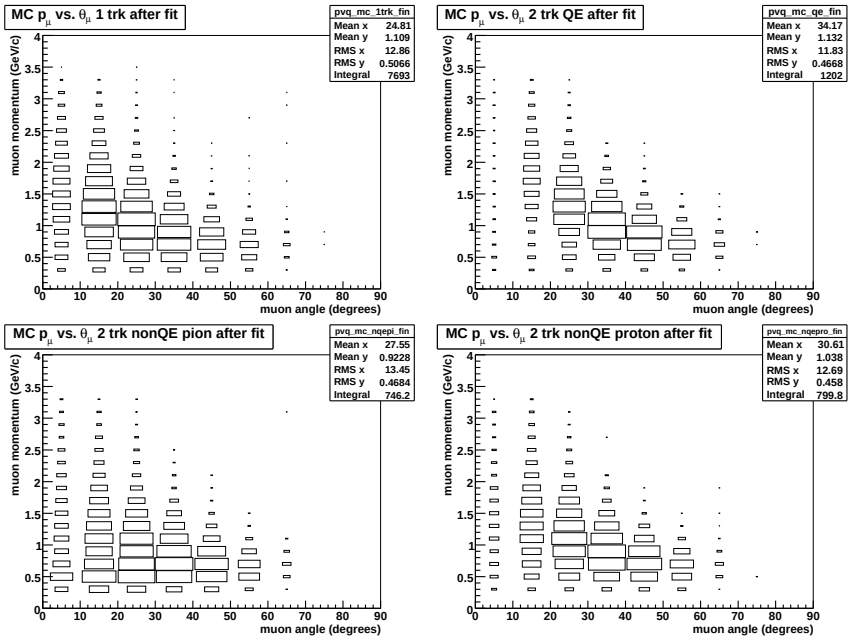

Figure B.6: p_μ vs. θ_μ for the best fit MC (E_ν-independent CC1π^+)

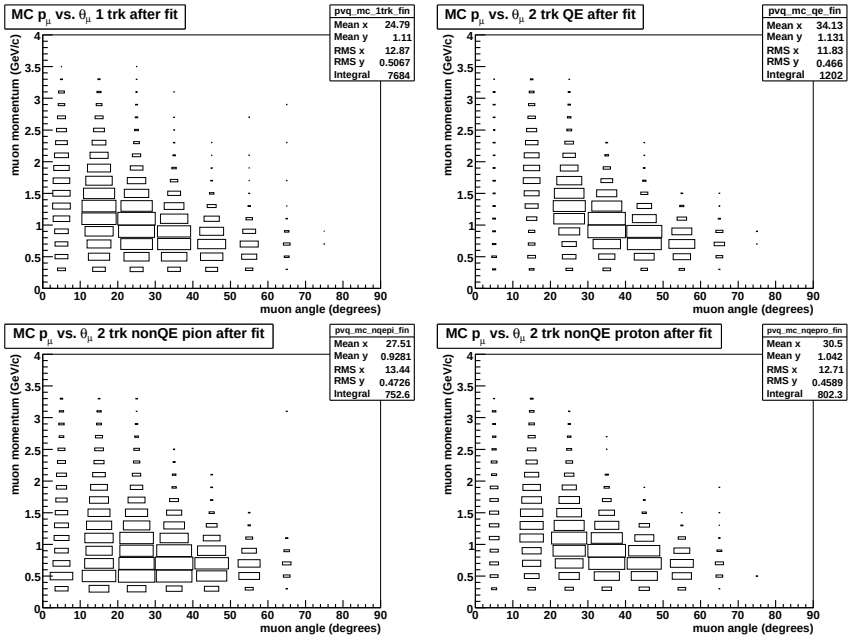

Figure B.7: p_μ vs. θ_μ for the best fit MC (E_ν-dependent CC1π^+)

Appendix C

Result for Exclusive Cross Section Measurement

C.1 Results (Exclusive Cross Section)

C.1.1 Fitting Results (Exclusive Cross Section)

Result with energy-independent CCpπ^+ scaling (Exclusive π^+)

The best fit parameters are given in Table C.1. The errors shown include the effect of correlations between the parameters. The χ^2/d.o.f. of best fit is 229/184 = 1.25. Table C.2 shows the correlation matrix. The value of $\alpha/\alpha_{nominal}$ is 1.18. Table C.3 gives the number of CCQE, CCpπ^+, and background interactions in data relative to the MC prediction.

Table C.1: Best Fit Parameter Values (Exclusive π^+)

Parameter	Best Fit Value
P_{sc}	0.974±0.003
R^{CCQE}	0.802±0.062
$R_0^{CCp\pi^+}$	0.789±0.155

Result with energy-dependent CCpπ^+ scaling (Exclusive π^+)

The best fit values are given in Table C.4. The errors shown include the effect of correlations between the parameters. The χ^2/d.o.f. of best fit is 228/181 = 1.26. Table C.5 shows the correlation matrix. The value of

Table C.2: Correlation Matrix (Exclusive π^+)

	P_{sc}	R^{CCQE}	$R_0^{CC p\pi^+}$
P_{sc}	1.000	-0.310	-0.091
R^{CCQE}	-0.310	1.000	0.773
$R_0^{CC p\pi^+}$	-0.091	0.773	1.000

Table C.3: CCQE, CC$p\pi^+$, and background in data relative to MC prediction (Exclusive π^+)

$\frac{N^{CCQE}(data)}{N^{CCQE}(nominalMC)}$	0.95
$\frac{N^{CC p\pi^+}(data)}{N^{CC p\pi^+}(nominalMC)}$	0.93
$\frac{N^{Bkgd}(data)}{N^{Bkgd}(nominalMC)}$	1.18

$\alpha/\alpha_{nominal}$ is 1.24. Table C.6 gives the number of CCQE, CCpπ^+ (for each energy bin), and background interactions in data relative to the MC prediction.

Table C.4: Best Fit Parameter Values (Exclusive π^+)

Parameter	**Best Fit Value**
P_{sc}	0.975±0.005
R^{CCQE}	0.765±0.065
$R_0^{CC p\pi^+}$	0.574±0.223
$R_1^{CC p\pi^+}$	0.836±0.179
$R_2^{CC p\pi^+}$	0.695±0.193
$R_3^{CC p\pi^+}$	0.747±0.247

Table C.5: Correlation Matrix (Exclusive π^+)

	P_{sc}	R^{CCQE}	$R_0^{CC p\pi^+}$	$R_1^{CC p\pi^+}$	$R_2^{CC p\pi^+}$	$R_3^{CC p\pi^+}$
P_{sc}	1.000	-0.054	0.279	0.013	0.039	-0.406
R^{CCQE}	-0.054	1.000	0.763	0.557	0.584	0.450
$R_0^{CC p\pi^+}$	0.279	0.763	1.000	0.438	0.670	0.358
$R_1^{CC p\pi^+}$	0.013	0.557	0.438	1.000	0.302	0.514
$R_2^{CC p\pi^+}$	0.039	0.584	0.670	0.302	1.000	0.235
$R_3^{CC p\pi^+}$	-0.406	0.450	0.358	0.514	0.235	1.000

C.1.2 Final Results (Exclusive Cross Section)

The final results for the energy-independent and energy-dependent cross section ratios are given in Tables C.7 and C.8, respectively.

C.1.3 Systematic Uncertainties (Exclusive Cross Section)

Tables C.9 and C.10 give a summary of the systematic errors of the energy-independent and energy-dependent cross section ratio, respectively.

Table C.6: CCQE, CC$p\pi^+$ (for each energy bin), and background in data relative to MC prediction (Exclusive π^+)

$\frac{N^{CCQE}(data)}{N^{CCQE}(nominalMC)}$	0.95
$\frac{N_0^{CCp\pi^+}(data)}{N_0^{CCp\pi^+}(nominalMC)}$	0.71
$\frac{N_1^{CCp\pi^+}(data)}{N_1^{CCp\pi^+}(nominalMC)}$	1.04
$\frac{N_2^{CCp\pi^+}(data)}{N_2^{CCp\pi^+}(nominalMC)}$	0.86
$\frac{N_3^{CCp\pi^+}(data)}{N_3^{CCp\pi^+}(nominalMC)}$	0.93
$\frac{N^{Bkgd}(data)}{N^{Bkgd}(nominalMC)}$	1.24

Table C.7: Energy-Independent Cross Section Ratio (Exclusive π^+)

Energy Range (GeV)	**Measured Ratio**	**MC Prediction**
>0.00	$0.556\pm0.145(\text{fitting})^{+0.117}_{-0.128}(\text{syst})$	0.565 ± 0.002(stat)

Table C.8: Energy-Dependent Cross Section Ratio (Exclusive π^+)

Energy Range (GeV)	**Measured Ratio**	**MC Prediction**
0.00-1.35	$0.331 \pm 0.151(\text{fitting})^{+0.146}_{-0.103}(\text{syst})$	$0.441 \pm 0.002(\text{stat})$
1.35-1.72	$0.760 \pm 0.206(\text{fitting})^{+0.123}_{-0.233}(\text{syst})$	$0.695 \pm 0.004(\text{stat})$
1.72-2.22	$0.711 \pm 0.238(\text{fitting})^{+0.275}_{-0.159}(\text{syst})$	$0.782 \pm 0.006(\text{stat})$
>2.22	$0.846 \pm 0.319(\text{fitting})^{+0.355}_{-0.421}(\text{syst})$	$0.860 \pm 0.010(\text{stat})$

Table C.9: Syst. Uncertainties for Energy-Independent Ratio (Exclusive π^+)

Condition	ΔR_0
Detector Simulation	
Crosstalk ±0.25%	+0.045,-0.071
PMT Res. ±10%	+0.020,-0.032
Birks' Const. ±0.0023	+0.010,+0.030
Reconstruction	
Threshold ±15%	±0.052
Angular res.	±0.010
Model	
M_A^{QE} ±0.1 GeV	-0.039,+0.036
Bodek/Yang Corr. ±30%	-0.003,-0.009
Neutrino Flux	+0.007,-0.028
Nuclear Effects	
π abs. ±30%	+0.035,+0.055
π inel. scat. ±30%	+0.054,-0.057
proton rescat. ±10%	-0.041,-0.009
Fermi mom.	±0.017
MC Stats.	±0.005
Total Syst. Error	**-0.128,+0.117**

Table C.10: Syst. Uncertainties for Energy-Dependent Ratio (Exclusive π^+)

Condition	ΔR_0	ΔR_1	ΔR_2	ΔR_3
Detector Simulation				
Crosstalk ±0.25%	+0.044,-0.001	+0.026,-0.124	+0.110,-0.051	+0.045,-0.213
PMT Res. ±10%	+0.007,-0.040	+0.020,-0.040	+0.037,-0.034	+0.025,-0.086
Birks' Const. ±0.0023	+0.031,+0.033	-0.005,+0.026	+0.031,+0.072	+0.006,-0.088
Reconstruction				
Threshold ±15%	±0.029	±0.075	±0.037	±0.199
Angular res.	±0.020	±0.002	±0.025	±0.004
Model				
M_A^{QE} ±0.1 GeV	-0.035,+0.000	-0.041,+0.036	-0.022,+0.013	-0.176,+0.214
Bodek/Yang Corr. ±30%	-0.000,-0.006	-0.003,-0.011	+0.003,-0.016	-0.052,-0.017
Neutrino Flux	+0.063,-0.072	+0.040,-0.063	+0.147,-0.135	+0.053,-0.163
Nuclear Effects				
π abs. ±30%	-0.004,+0.110	-0.011,+0.005	+0.111,+0.149	+0.171,+0.053
π inel. scat. ±30%	+0.025,-0.015	+0.065,-0.136	+0.100,+0.013	+0.064,-0.097
proton rescat. ±10%	-0.030,+0.005	-0.081,-0.025	+0.009,+0.019	-0.057,-0.078
Fermi mom.	±0.011	±0.020	±0.021	±0.030
MC Stats.	±0.005	±0.012	±0.013	±0.024
Total Syst. Error	**-0.103,+0.146**	**-0.233,+0.123**	**-0.159,+0.275**	**-0.421,+0.355**

Appendix D

Summary of Previous Experimental Results

The ANL single pion result is summarized in Table D.1, and the ANL CCQE measurement is summarized in Table D.2. The GGM single pion result is summarized in Table D.3, and the GGM CCQE result is summarized in Table D.4.

Table D.1: Radecky *et al.* 1982 single pion measurement [49]

E_μ (GeV)	$\sigma(\nu p \to \mu^- p \pi^+)$ (10^{-38}cm^2)	$\sigma(\nu n \to \mu^- n \pi^+)$ (10^{-38}cm^2)	sum (10^{-38}cm^2)
0.30-0.50	0.019±0.006	0.009±0.005	0.028±0.008
0.50-0.75	0.155±0.017	0.061±0.012	0.216±0.021
0.75-1.00	0.335±0.030	0.109±0.020	0.444±0.036
1.00-1.25	0.435±0.042	0.132±0.026	0.567±0.049
1.25-1.50	0.488±0.055	0.166±0.037	0.654±0.066
1.50-2.50	0.707±0.087	–	–
2.50-3.50	0.722±0.174	–	–
3.50-6.00	0.552±0.150	–	–

Using the published results from these experiments, the CC1π^+ (and CCpπ^+) to CCQE cross section ratio for each experiment can be calculated. (Some interpolation is necessary because of different energy binning in the CC1π and CCQE measurements.) The ANL inclusive and exclusive cross section ratios are given in Table D.5 and Table D.6, respectively. The GGM exclusive cross section ratio is given in Table D.7. Table D.8 shows the exclusive cross section ratio from BNL [83].

Table D.2: Barish *et al.* 1977 CCQE measurement [39]

E_μ (GeV)	$\sigma(\nu n \to \mu^- p)$ (10^{-38}cm^2)
0.15-0.30	0.29±0.08
0.30-0.50	0.57±0.10
0.50-0.70	0.77±0.10
0.70-0.90	0.72±0.14
0.90-1.25	1.12±0.12
1.25-1.50	1.15±0.28
1.50-2.00	1.02±0.21
2.00-6.00	1.18±0.33

Table D.3: Lerche *et al.* 1978 single pπ^+ measurement [50]

E_ν (GeV)	$\sigma(\nu_\mu p \to \mu^- p \pi^+)$ (10^{-38} cm^2)
1.00 - 1.5	0.47 ± 0.12
1.50 - 2.00	0.60 ± 0.09
2.00 - 3.00	0.50 ± 0.07
3.00 - 4.00	0.45 ± 0.08
4.00 - 10.0	0.47 ± 0.09

Table D.4: Pohl *et al.* 1979 CCQE measurement [84]

E_ν (GeV)	$\sigma(\nu_\mu n \to \mu^- p)$ (10^{-38} cm^2)
1.00 - 1.25	0.96 ± 0.16
1.25 - 1.50	0.85 ± 0.14
1.50 - 2.00	0.67 ± 0.12
2.00 - 2.50	0.92 ± 0.11
2.50 - 3.00	0.94 ± 0.13
3.00 - 4.00	0.90 ± 0.12
4.00 - 8.50	0.70 ± 0.12

Table D.5: ANL, R = $\frac{\sigma(CC1\pi^+)}{\sigma(CCQE)}$

E_μ (GeV)	R (Radecky)
0.30-0.50	0.05±0.02
0.50-0.75	0.28±0.05
0.75-1.00	0.62±0.13
1.00-1.25	0.51±0.07
1.25-1.50	0.57±0.15

Table D.6: ANL, R = $\frac{\sigma(CCp\pi^+)}{\sigma(CCQE)}$

E_ν(GeV)	R (ANL)
0.30 - 0.50	0.033 ± 0.012
0.50 - 0.75	0.201 ± 0.034
0.75 - 1.00	0.465 ± 0.100
1.00 - 1.25	0.388 ± 0.056
1.25 - 1.50	0.424 ± 0.114
1.50 - 2.50	0.604 ± 0.136

Table D.7: GGM, R = $\frac{\sigma(CCp\pi^+)}{\sigma(CCQE)}$

E_ν(GeV)	R (GGM)
1.00 - 1.50	0.520 ± 0.180
1.50 - 2.00	0.896 ± 0.210
2.00 - 3.00	0.538 ± 0.124
3.00 - 4.00	0.500 ± 0.111

Table D.8: BNL [83], R = $\frac{\sigma(CCp\pi^+)}{\sigma(CCQE)}$

E_ν(GeV)	R (BNL)
0.48-0.68	$0.051^{+0.022}_{-0.030}$
0.68-0.88	$0.310^{+0.040}_{-0.038}$
0.88-1.08	$0.445^{+0.041}_{-0.046}$
1.08-1.28	$0.520^{+0.053}_{-0.051}$
1.28-1.48	$0.565^{+0.051}_{-0.047}$
1.48-1.68	$0.583^{+0.057}_{-0.053}$
1.68-2.12	$0.640^{+0.051}_{-0.047}$
2.12-2.64	$0.664^{+0.075}_{-0.065}$
2.64-4.12	$0.780^{+0.081}_{-0.081}$
4.12-6.28	$0.878^{+0.167}_{-0.167}$

Appendix E

Scaling the Result

SciBar is made of polystyrene (C_8H_8) which has 56 protons and 48 neutrons. Therefore,

$$\begin{aligned}\sigma(\nu(C_8H_8) \to \mu^- p\pi^+) &= 56\sigma(\nu p \to \mu^- p\pi^+) \\ \sigma(\nu(C_8H_8) \to \mu^- n\pi^+) &= 48\sigma(\nu n \to \mu^- n\pi^+) \\ \sigma(\nu(C_8H_8) \to \mu^- p) &= 48\sigma(\nu n \to \mu^- p)\end{aligned} \tag{E.1}$$

The measured cross section ratio is:

$$\begin{aligned}R_{measured} &= \frac{\sigma(\nu(C_8H_8) \to \mu^- p\pi^+) + \sigma(\nu(C_8H_8) \to \mu^- n\pi^+)}{\sigma(\nu(C_8H_8) \to \mu^- p)} \\ &= \frac{56\sigma(\nu p \to \mu^- p\pi^+) + 48\sigma(\nu n \to \mu^- n\pi^+)}{48\sigma(\nu n \to \mu^- p)}\end{aligned} \tag{E.2}$$

The cross section ratio needed in order to compare with other experiments is:

$$R = \frac{\sigma(\nu p \to \mu^- p\pi^+) + \sigma(\nu n \to \mu^- n\pi^+)}{\sigma(\nu n \to \mu^- p)} \tag{E.3}$$

Therefore, the measured valued needs to be scaled. What is the factor, f, by which the measured ratio, $R_{measured}$, can be multiplied to get the corrected ratio, R?

$$R = f \times R_{measured} \tag{E.4}$$

Define the ratios S_p and S_n:

$$S_p \equiv \frac{\sigma(\nu(C_8H_8) \to \mu^- p\pi^+)}{\sigma(\nu(C_8H_8) \to \mu^- p\pi^+) + \sigma(\nu(C_8H_8) \to \mu^- n\pi^+)}$$
$$S_n \equiv \frac{\sigma(\nu(C_8H_8) \to \mu^- n\pi^+)}{\sigma(\nu(C_8H_8) \to \mu^- p\pi^+) + \sigma(\nu(C_8H_8) \to \mu^- n\pi^+)} \tag{E.5}$$

Assume that S_p and S_n are approximately the same in the data as in the MC. Then,

$$\begin{aligned} R &= \frac{\sigma(\nu p \to \mu^- p\pi^+) + \sigma(\nu n \to \mu^- n\pi^+)}{\sigma(\nu n \to \mu^- p)} \\ &= \frac{(1/56)\sigma(\nu(C_8H_8) \to \mu^- p\pi^+) + (1/48)\sigma(\nu(C_8H_8) \to \mu^- n\pi^+)}{(1/48)\sigma(\nu(C_8H_8) \to \mu^- p)} \\ &= \frac{[(1/56)S_p + (1/48)S_n]\,[\sigma(\nu(C_8H_8) \to \mu^- p\pi^+) + \sigma(\nu(C_8H_8) \to \mu^- n\pi^+)]}{(1/48)\sigma(\nu(C_8H_8) \to \mu^- p)} \\ &= \frac{(1/56)S_p + (1/48)S_n}{(1/48)} R_{measured} \\ &= [(48/56)S_p + S_n]\, R_{measured} \end{aligned} \tag{E.6}$$

Thus the scaling factor is $f = (48/56)S_p + S_n$ where S_p and S_n are calculated from the MC. The result is $f = 0.9$.

For the exclusive cross section ratio, the situation is much more simple.

$$\begin{aligned} R_{measured}(exc) &= \frac{\sigma(\nu(C_8H_8) \to \mu^- p\pi^+)}{\sigma(\nu(C_8H_8) \to \mu^- p)} \\ &= \frac{56\sigma(\nu p \to \mu^- p\pi^+)}{48\sigma(\nu n \to \mu^- p)} \\ &= \frac{7}{6} \times \frac{\sigma(\nu p \to \mu^- p\pi^+)}{\sigma(\nu n \to \mu^- p)} \\ &= \frac{7}{6} \times R(exc) \end{aligned} \tag{E.7}$$

So, scaling by a factor of $f = 6/7$ is all that is needed to correct the exclusive cross section ratio.

Bibliography

[1] L. M. Brown, Phys. Today **31** (9), 23 (1978).

[2] E. Fermi, Z. Phys. **88**, 161 (1934).

[3] F. Reines, C. L. Cowan *et al.*, Science **124** (3212), 103 (1956).

[4] G. Danby, J. M. Gaillard, K. Goulianos, L. M. Lederman, N. B. Mistry, M. Schwartz and J. Steinberger, Phys. Rev. Lett. **9**, 36 (1962).

[5] K. Kodama *et al.* [DONUT Collaboration], Phys. Lett. B **504**, 218 (2001) [arXiv:hep-ex/0012035].

[6] W. M. Yao *et al.* [Particle Data Group], J. Phys. G **33**, 1 (2006).

[7] Y. Fukuda *et al.* [Super-Kamiokande Collaboration], Phys. Rev. Lett. **81**, 1562 (1998) [arXiv:hep-ex/9807003].

[8] Y. Ashie *et al.* [Super-Kamiokande Collaboration], Phys. Rev. D **71**, 112005 (2005) [arXiv:hep-ex/0501064].

[9] Y. Fukuda *et al.*, Nucl. Instrum. Meth. A **501**, 418 (2003).

[10] S. Nakayama *et al.* [K2K Collaboration], Phys. Lett. B **619**, 255 (2005) [arXiv:hep-ex/0408134].

[11] A. Suzuki *et al.* [K2K Collaboration], Nucl. Instrum. Meth. A **453**, 165 (2000) [arXiv:hep-ex/0004024].

[12] B. J. Kim *et al.*, Nucl. Instrum. Meth. A **497**, 450 (2003) [arXiv:hep-ex/0206041].

[13] R. Brun, F. Bruyant, M. Maire, A. C. McPherson and P. Zanarini, Report No. CERN-DD/EE/84-1, 1987 (unpublished).

[14] GEANT Detector Description and Simulation Tool, [http://wwwasd.web.cern.ch/wwwasd/geant/].

[15] T. Ishii *et al.* [K2K MRD GROUP Collaboration], Nucl. Instrum. Meth. A **482**, 244 (2002) [Erratum-ibid. A **488**, 673 (2002)] [arXiv:hep-ex/0107041].

[16] M. H. Ahn *et al.* [K2K Collaboration], Phys. Rev. D **74**, 072003 (2006) [arXiv:hep-ex/0606032].

[17] S. Yamamoto *et al.* [K2K Collaboration], Phys. Rev. Lett. **96**, 181801 (2006) [arXiv:hep-ex/0603004].

[18] M. Hasegawa *et al.* [K2K Collaboration], Phys. Rev. Lett. **95**, 252301 (2005) [arXiv:hep-ex/0506008].

[19] R. Gran *et al.* [K2K Collaboration], Phys. Rev. D **74**, 052002 (2006) [arXiv:hep-ex/0603034].

[20] I. Kato, Ph.D. thesis, Kyoto University, 2004.

[21] M. Hasegawa, Ph.D. thesis, Kyoto University, 2006.

[22] K. Nitta *et al.*, Nucl. Instrum. Meth. A **535**, 147 (2004) [arXiv:hep-ex/0406023].

[23] S. Yamamoto *et al.*, IEEE Trans. Nucl. Sci. **52**, 2992 (2005).

[24] T. Sasaki, Master's thesis, Kyoto University, 2004.

[25] M. Yoshida *et al.*, IEEE Trans. Nucl. Sci. **51**, 3043 (2004).

[26] J. Birks, *Theory and Practice of Scintillation Counting*, (Pergamon Press, 1964).

[27] S. Buontempo *et al.*, Nucl. Instrum. Meth. A **349**, 70 (1994).

[28] J. R. Sanford and C. L. Wang, Brookhaven National Laboratory Reports No. BNL 11299 and No. BNL 11479, 1967 (unpublished).

[29] C. L. Wang, Phys. Rev. Lett. **25**, 1068 (1970).

[30] Y. Cho *et al.*, Phys. Rev. D **4**, 1967 (1971).

[31] A. Yamamoto, KEK Report No. 81-13, 1981.

[32] S. Eidelman *et al.* [Particle Data Group], Phys. Lett. B **592**, 1 (2004).

[33] E. D. Commins and P. H. Bucksbaum, *Weak Interactions of Leptons and Quarks*, (Cambridge University Press, 1983).

[34] M. G. Catanesi *et al.* [HARP Collaboration], Nucl. Phys. B **732**, 1 (2006) [arXiv:hep-ex/0510039].

[35] Y. Hayato, Nucl. Phys. Proc. Suppl. **112**, 171 (2002).

[36] C. H. Llewellyn Smith, Phys. Rept. **3**, 261 (1972).

[37] R. P. Feynman and M. Gell-Mann, Phys. Rev. **109**, 193 (1958).

[38] M. H. Ahn *et al.* [K2K Collaboration], Phys. Rev. Lett. **90**, 041801 (2003) [arXiv:hep-ex/0212007].

[39] S. J. Barish *et al.*, Phys. Rev. D **16**, 3103 (1977).

[40] S. Bonetti *et al.*, Nuovo Cim. A **38**, 260 (1977).

[41] S. V. Belikov *et al.*, Z. Phys. A **320**, 625 (1985).

[42] N. Armenise *et al.*, Nucl. Phys. B **152**, 365 (1979).

[43] L. A. Ahrens *et al.*, Phys. Rev. Lett. **56**, 1107 (1986) [Erratum-ibid. **56**, 1883 (1986)].

[44] C. H. Albright, C. Quigg, R. E. Shrock and J. Smith, Phys. Rev. D **14**, 1780 (1976).

[45] D. Rein and L. M. Sehgal, Annals Phys. **133**, 79 (1981).

[46] D. Rein, Z. Phys. C **35**, 43 (1987).

[47] R. P. Feynman, M. Kislinger and F. Ravndal, Phys. Rev. D **3**, 2706 (1971).

[48] T. Kitagaki *et al.*, Phys. Rev. D **34**, 2554 (1986).

[49] G. M. Radecky *et al.*, Phys. Rev. D **25**, 1161 (1982) [Erratum-ibid. D **26**, 3297 (1982)].

[50] W. Lerche *et al.*, Phys. Lett. B **78**, 510 (1978).

[51] M. Gluck, E. Reya and A. Vogt, Z. Phys. C **67**, 433 (1995).

[52] A. Bodek and U.K. Yang, Nucl. Phys. Proc. Suppl. **112** 70 (2002).

[53] T. Sjostrand, Comput. Phys. Commun. **82**, 74 (1994).

[54] M. Nakahata *et al.* [KAMIOKANDE Collaboration], J. Phys. Soc. Jap. **55**, 3786 (1986).

[55] P. Musset and J. P. Vialle, Phys. Rept. **39**, 1 (1978).

[56] J. E. Kim, P. Langacker, M. Levine and H. H. Williams, Rev. Mod. Phys. **53**, 211 (1981).

[57] D. Rein and L. M. Sehgal, Nucl. Phys. B **223**, 29 (1983).

[58] J. Marteau, J. Delorme and M. Ericson, Nucl. Instrum. Meth. A **451**, 76 (2000).

[59] R. A. Smith and E. J. Moniz, Nucl. Phys. B **43**, 605 (1972) [Erratum-ibid. B **101**, 547 (1975)].

[60] R. Woods and D. Saxon, Phys. Rev. **95**, 577 (1954).

[61] L. L. Salcedo, E. Oset, M. J. Vicente-Vacas and C. Garcia-Recio, Nucl. Phys. A **484**, 557 (1988).

[62] G. Rowe, M. Salomon and R. H. Landau, Phys. Rev. C **18**, 584 (1978).

[63] B. R. Martin and M. K. Pidcock, Nucl. Phys. B **126**, 266 (1977).

[64] B. R. Martin and M. K. Pidcock, Nucl. Phys. B **126**, 285 (1977).

[65] J. S. Hyslop, R. A. Arndt, L. D. Roper and R. L. Workman, Phys. Rev. D **46**, 961 (1992).

[66] D. A. Sparrow, AIP Conf. Proc. **123**, 1019 (1984).

[67] D. Ashery, I. Navon, G. Azuelos, H. K. Walter, H. J. Pfeiffer and F. W. Schleputz, Phys. Rev. C **23**, 2173 (1981).

[68] H. W. Bertini, Phys. Rev. C **6**, 631 (1972).

[69] S. J. Lindenbaum and R. M. Sternheimer, Phys. Rev. **105**, 1874 (1957).

[70] C. Zeitnitz and T. A. Gabriel, Nucl. Instrum. Meth. A **349**, 106 (1994).

[71] N. Tagg *et al.*, Nucl. Instrum. Meth. A **539**, 668 (2005) [arXiv:physics/0408055].

[72] L. Whitehead, (internal note) 2006.

[73] H. Maesaka, Ph.D. thesis, Kyoto University, 2005.

[74] I. Abt, I. Kisel, S. Masciocchi and D. Emelyanov, Nucl. Instrum. Meth. A **489**, 389 (2002).

[75] D. Allasia *et al.*, Nucl. Phys. B **343**, 285 (1990).

[76] J. Bell *et al.*, Phys. Rev. Lett. **41**, 1008 (1978).

[77] R. Brun and F. Rademakers, Nucl. Instrum. Meth. A **389**, 81 (1997).

[78] F. James and M. Roos, Comput. Phys. Commun. **10**, 343 (1975).

[79] C. H. Q. Ingram *et al.*, Phys. Rev. C **27**, 1578 (1983).

[80] E. J. Jeon, Ph.D. thesis, The Graduate University for Advanced Studies (Sokendai), 2003.

[81] E. J. Moniz, I. Sick, R. R. Whitney, J. R. Ficenec, R. D. Kephart and W. P. Trower, Phys. Rev. Lett. **26**, 445 (1971).

[82] N. J. Baker *et al.*, Phys. Rev. D **23**, 2499 (1981).

[83] T. Kitagaki *et al.*, Phys. Rev. D **42**, 1331 (1990).

[84] M. Pohl *et al.*, Lett. Nuovo Cimento **26**, 332 (1979).

[85] M. O. Wascko [MiniBooNE Collaboration], Nucl. Phys. Proc. Suppl. **159**, 50 (2006) [arXiv:hep-ex/0602050].